Aus dem Max-Planck-Institut für Kolloid- und Grenzflächenforschung

Forces and elasticity in cell adhesion

Habilitationsschrift

zur Erlangung des akademischen Grades
Doktor rerum naturalium habilitatus
(Dr. rer. nat. habil.)
in der Wissenschaftsdisziplin Theoretische Physik

eingereicht an der
Mathematisch-Naturwissenschaftlichen Fakultät
der Universität Potsdam

von
Dr. Ulrich Schwarz
geboren am 3.3.1966 in Stuttgart

Potsdam, im Januar 2004

Contents

1 Introduction **1**
- 1.1 General aspects of cell adhesion 1
- 1.2 Cell-matrix adhesion 7
- 1.3 Rolling adhesion 11
- 1.4 Overview 13

2 Elastic substrates **15**
- 2.1 Introduction 15
- 2.2 Experimental method 17
- 2.3 Computational method 18
- 2.4 Assumption of localized force and finite size effects 22
- 2.5 Data simulation, regularization and resolution 26
- 2.6 Analysis of experimental data 31
- 2.7 Conclusions 36

3 Bond dynamics **41**
- 3.1 Introduction 41
- 3.2 Single bond 47
- 3.3 Stochastic model for multiple bonds 50
- 3.4 Two bonds under constant shared loading 55
- 3.5 Cluster under constant shared loading 58
- 3.6 Cluster under linear shared loading 65
- 3.7 Biological relevance 70

4 Elastic interactions **75**
- 4.1 Introduction 75
- 4.2 Modeling 79
  - 4.2.1 Force multipoles 79

4.2.2 Elastic interactions for physical dipoles 80
4.2.3 Elastic interactions for active cells 82
4.2.4 Isotropic elastic medium 85
4.2.5 External strain 86
4.2.6 Boundary-induced image strain 87
4.2.7 Elastic interactions between cells 88
4.2.8 Summary modeling section 88
4.3 Examples of cell organization 90
4.3.1 Interaction with external strain 90
4.3.2 Dipoles on elastic halfspace 91
4.3.3 Dipoles in elastic full space 94
4.3.4 Dipoles in elastic halfspace 96
4.3.5 Dipoles in elastic sphere 101
4.3.6 Summary example section 106
4.4 Conclusions 108

Bibliography **111**

Acknowledgements **128**

Publications used in this work **129**

Chapter 1

Introduction

1.1 General aspects of cell adhesion

The human body consists of around 10^{13} cells, which can be classified into more than 200 different cell types [2]. In order to function in the way we are used to, the human body has to fulfill two seemingly contradicting principles. On the one hand, the cells in our body have to adhere to each other, otherwise it would simply fall apart. On the other hand, they must be able to reorganize quickly, for example when the body has to react to infection or injury. Nature has evolved different strategies to cope with these conflicting requirements. On the molecular level, biological adhesion is based on relatively weak (non-covalent) interactions with short lifetimes of the order of seconds. In order to achieve long-lived assemblies, the cells in our body adhere through clusters of adhesions bonds, which prolongue lifetime both by large bond numbers and by facilitating rebinding of single bonds. Because they are highly dynamic, biological adhesion clusters can react quickly to new stimuli by association and dissociation. On the level of tissues, cells build up an additional structure, the extracellular matrix (ECM), a network of protein filaments (e.g. collagen in the connective tissue) which provides structural integrity to the tissue as a whole. The ECM is secreted by cells during developement or after injury and is continuously remodeled by the cells. It provides structural coupling between the cells without preventing them from dynamic rearrangements.

Cells in a multicellular organism communicated with each other through many different channels. The main mean of communication is release and capture of biochemical molecules [101]. In this way, cells can exchange very specific information. In solution, the biochemical information is supplemented by one additional degree of information, namely ligand concentration (including diffusion gradients). In cell adhesion, biochemical ligands are attached to surfaces, like the plasma membrane of other cells or the proteins of the ECM. Therefore now the biochemical information can be supplemented by several additional degrees of information, including spatial distributions of ligand which are not determined by diffusion, and the mechanical properties of the structure the cell attaches to. However, experimentally it is very difficult to quantify these additional factors. During recent years, rapid advances in materials science have led to strongly improved control of extracellular ligand distribution and of the properties of the micromechanical environment. As a result, the investigation of cellular response to the biochemical and physical properties of adhesive surfaces has become a very active area of research. Apart from understanding the basic principles of cellular decision making in a physiological environment, this field is also driven by the prospect of designing artificial environments for cells, which on the one hand can function as biomimetic environment, but on the other hand can also be more versatile than biological environments, which result from specific developmental processes. In general, the combination of materials science and active biological processes promises exciting new developments in the future [113]. In particular, judging from the developments of the last years, one might expect that cell adhesion and materials science (including soft lithography, microfluidics, and nanotechnology) are going to merge into a new field in the future, which also might lead to completely new biomedical applications, including new kinds of biochips [129] and artificial tissues [37].

Traditionally, cells have been studied on flat substrates, like culture dishes made from glass or plastic, which can be easily used in standard setups for optical microscopy. In the early 1980s, Harris and coworkers introduced the use of elastic substrates into cell biology [76, 75]. By crosslinking the surface of silicon oil by exposure to heat, they created thin polymer films which due to their small thickness tend to buckle under cell traction. The resulting wrinkles can be easily observed in optical microscopy and have been used as qualitative assay for mechanical activity of cells since then. However, a quantitative analysis of cell traction by elastic substrates has been achieved only much later, mainly through the use of non-wrinkling elastic substrates made from polyacrylamide (PAA). By inverting the elastic equations, it then became feasible to calculate the details of cellular traction patterns from the

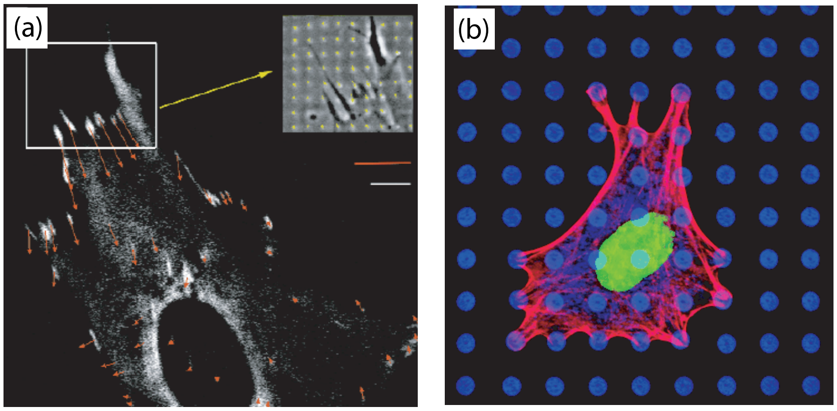

Figure 1.1: The mechanical activity of cells can be monitored on elastic substrates. Recent advances include the fabrication of micropatterned elastic substrates made from the elastomer polydimethylsiloxane (PDMS). (a) A shallow pattern of dots effectively preserves the flatness of the substrate, but can be used for easy visualization of the deformations due to cell traction (small green arrows in inset). Combined with fluorescence markers for the sites of focal adhesion (white) and linear elasticity theory, this allows to calculate the internal forces exerted at focal adhesions (large red arrows) [6]. (b) When plated on a bed of flexible microneedles fabricated with PDMS, cellular traction generated in the actin cytoskeleton (red) leads to displacement of the needle tips (blue). For small bending, the needles act as linear springs, thus here force is simply proportional to displacement (cell nucleus in green) [169].

displacement data (*traction force spectroscopy*) [40, 42]. Recent advances in this field include the use of micropatterned elastic substrates made from polydimethylsiloxane (PDMS) [6, 169] and the combination of traction force microscopy with fluorescent constructs for cell-matrix contacts [6, 12]. A growing body of evidence now suggests that the mechanical properties of the extracellular environment (in particular its elasticity) play a much more important role for cellular decision making than formerly appreciated. In particular, it has been shown that cells more strongly upregulate cytoskeleton and cell-matrix adhesion on stiffer substrates [135, 46], that cells locomote in favor of stiffer or strained substrates [116, 179], and that extracellular mechanical properties and cellular decision making are connected by the internal forces developing at cell-matrix contacts due to cellular actomyosin contractility [6].

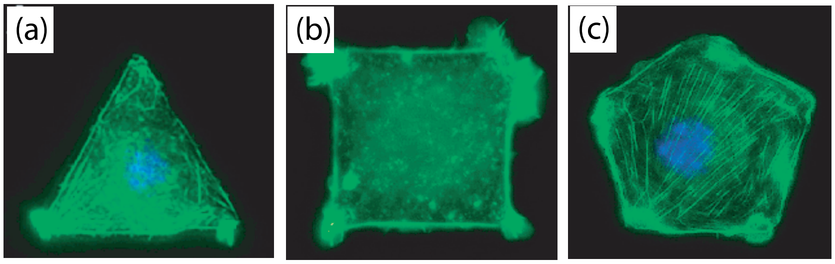

Figure 1.2: Adhesive patterns with different geometries can be created by microcontact printing of suitable proteins on flat substrates. When plated on these adhesive islands, cells adopt the given shapes, e.g. (a) triangle, (b) square, or (c) pentagon [19].

A development closely related with these improvements in the elastic substrate techniques is the control of cell adhesion by microcontact printing. Recent advances in microfabrication technology, originally developed for the semiconductor industry, make it possible to create adhesive islands of different shapes on a passivated surface. It has found by the groups of Ingber and Whitesides that cells plated on these islands adopt the given shape (resulting in e.g. square-shaped cells) and that this shape determines if cells grow and divide or if they switch on the death program [164, 29]. The same collaboration also has reported that cells on adhesive island extend lamellipodia and filopodia preferentially from the corner regions [134, 19]. Recent results from the Bastmeyer group suggest that below a ligand coverage of around 15 percent, the geometrical stimulus might become less important than the chemical one [104].

Very recently, the two fields of cells on gels and cells on islands have been combined for the first time [176]. Usually, the adhesive islands are created with the ECM-protein fibronectin (FN) on glass and passivation is achieved by polyethylene glycol (PEG). In the new technique, elastic substrates were made from PAA and covered with a thin membrane of PDMS, which featured holes of different shapes created by microfabrication. Collagen was adsorbed to the elastic substrate through the holes, the PDMS membrane was removed and the exposed area passivated with bovine serum albumin (BSA). Traction force microscopy then revealed that forces are highest at the corners, thus again mechanical factors seem to determine cellular behaviour.

It has long been known, especially in the medical and bioengineering communities, that certain cell functions are strongly determined by mechanical stimuli. For example, endothelial cells in blood capillaries [39], osteocytes in bone [43] and aveolar cells of type II in lung [178] only function properly when subject to a certain level of strain indicating proper body functioning (namely the one resulting from blood pulsation, body movements and breathing, respectively). However, only recently has it become possible to study the mechanisms of the underlying mechanotransduction processes in quantitative detail and on the level of single cells. During the last decade, there has been an increased effort to study the effect of externally applied force on cells. Several different experimental techniques have been applied for this purpose, including magnetic twisting cytometry [175], laser optical tweezers [35] and micropipettes [144]. These studies showed that there is a strong correlation between aggregation of cell-matrix contacts, build-up of force and triggering of certain signaling cascades determining such physiologically important processes as cell division, apoptosis (programmed cell death), and cell migration [56, 34, 60]. In particular, there is a close relation between the proper functioning of cell-matrix contacts and certain diseases like cancer.

In order to elucidate the molecular basis of these phenomena, another recent development in biophysics might be highly relevant, namely single molecule dynamic force spectroscopy (DFS). Pioneered by early AFM-experiments by the Gaub group [54] and later put onto a firm theoretical basis by Evans and Ritchie [51], which then was confirmed impressively by experiments both in the Gaub [143] and Evans groups [124], it was shown that adhesion bonds feature a much more complicated behaviour under force than suggested by the traditional affinity experiments in solution [101]. In detail, it has been shown that binding strength (the force needed to rupture a bond) is a dynamical quantity which depends crucially on the loading rate with which the bond is probed [51, 88, 160]. A large number of DFS-experiments with different experimental techniques and a growing body of theoretical studies have now demonstrated that most biomolecular adhesion bonds feature a complicated binding energy landscape [49], whose biological significance has to be identified in the future. In this context, it is very likely that some of these bonds serve as mediators between the mechanical properties of the extracellular environment and intracellular decision making. For example, it has been argued that force generation by tissue cells might mechanically destroy the RGD-motive common to many ECM-proteins like fibronectin, thus triggering other biochemical and structural changes important for mechanosensation of cells [96]. Recently it has been reported that the fibronectin domain FN-III$_1$ exhibits stable intermediate states during forced unfolding, which might expose cryptic binding sites inducing fibrillogenesis [57]. Since the FN-III$_1$ repeat is present in many proteins involved in signalling (e.g. tyrosine kinases and phosphatases), it seems to be a good candidate for mechanosensory function through single molecule unfolding. Although this appears to be a rather realistic scenario, it will be left to future studies to prove the physiological relevance of force-induced unbinding events.

During the last decades, much has been learned about cell function from detailed studies of vesicles [109, 115, 154]. Vesicles are closed shells made of lipid bilayers, which are one of the fundamental building blocks of cells. In particular, the plasma membrane defines cell shape and modulates the communication between cell and environment. On the micrometer scale, the behaviour of vesicles can be theoretically explained rather well using the concept of membrane curvature. Subjects especially interesting in regard to cellular systems include the shape of free vesicles [15, 125], domain formation and budding [110, 92], interaction with colloidal particles [114, 94], non-specific adhesion to flat substrates [158], free vesicles in shear flow [97], adhering vesicles in shear flow [155, 26, 167, 117], and forced unbinding of adhering vesicles [166]. In recent years, there has been an large effort to reconstitute increasingly more cellular features in vesicular systems, including incorporation of receptors, specific binding to flat substrates, anchorage of polymers, and coupling of actin gels to the lipid bilayer. Actin can be positioned either outside [78] or inside the vesicle [108] and opens the intriguing prospect of adding molecular motors from the myosin family. Molecular motors are responsible for active transport in cells and their stochastic dynamics has been extensively modeled during recent years [91, 112, 83]. Actomyosin contractility is the basis of mechanical activity of cells and the interaction of myosin and actin is a very active area of research [85]. However, until now it has not been possible to reconstitute actomyosin contractility in vesicular systems. This is different for the formation of adhesion plaques, which have been reconstituted with lipid vesicles carrying sticker and repeller molecules and adhering to a ligand-coated substrate [21]. During the last decade, several theoretical studies have been devoted to the possible mechanisms driving plaque formation, including elastic and entropically induced interactions between stickers [22, 111, 123, 177, 21].

In this work, we present recent theoretical work on the role of forces and elasticity in cell adhesion, using methods from statistical physics and physics of soft condensed matter. The main tools used are elasticity theory to characterize the mechanical properties of the extracellular environment and stochastic equations to model the bond dynamics at cell adhesion contacts. In contrast to existing work on vesicle adhesion, we assume that adhesion plaques have already been assembled and connected to the cytoskeleton. Since such a system has not yet been reconstituted for vesicles, our experimental reference systems are cellular ones. In particular, we will focus on two paradigmatic situations in cell adhesion, cell-matrix adhesion of tissue cells like fibroblasts to a flat substrate, and rolling adhesions of leukocytes. We start with the case of cell-matrix adhesion and present in chapter 2 a new technique which we have developed in a collaboration with cell biologists in order to measure for the first time internal force at single cell-matrix contacts [6, 151, 150]. Together with another study by the same collaboration on the effect of external force on cell-matrix contacts [144], this work proved that focal adhesions act as mechanosensors, converting force into biochemistry and vice versa. In order to address potential mechanism for the mechanosensor, in chaper 3 we will study the stochastic dynamics of clusters of molecular bonds under force [48, 47]. Our results have also been applied in a collaboration with immunologists to interpret recent advances in experiments with leukocytes under shear flow tethering to adhesive surfaces [44, 149]. In chapter 4, we will address the question how one can predict celluluar behaviour in a soft environment from our knowlegde on the kind of information gathered by the mechanosensor at cell-matrix contacts [153, 18, 17]. In the remainder of this chapter, we give additional background information and a more detailed overview for the main body of this work.

1.2 Cell-matrix adhesion

When cell-matrix adhesion is investigated experimentally, traditionally cells are dissolved in solution (often with the help of trypsin, which removes all former surface attachements) and studied on a culture dish inserted into some microscopic setup. The solution usually contains nutrients and buffers. Depending on the objective of the experiment, it might also contain additional factors, e.g. growth factors triggering cell growth and division. A culture dish is typically made from glass or plastic and provides a flat, rigid substrate for cell adhesion. Cell adhesion onto the substrate usually takes place

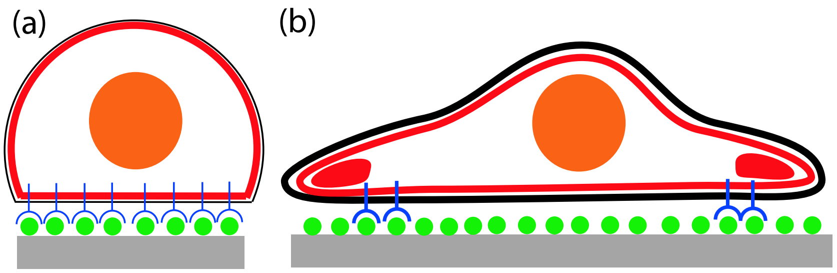

Figure 1.3: Schematic representation of cell adhesion. (a) Specific recognition provides a gain in adhesion energy driving cell adhesion. As for the adhesion of other soft objects, the size of the contact region is determined by object's resistance to elastic deformation, which for cells is provided mainly by the actin cortex underlying the cell membrane (red line). (b) Mature cell adhesion is determined by active processes, namely polymerizing actin gels pushing out the cell envelope (red regions) and formation of focal adhesions close to the cell rim, thus pinning it to its new location. These processes typically lead to a pancake-like cell shape.

only if the appropriate kind of proteins have been adsorbed onto it. These proteins have to be ligands to cell adhesion receptors of the cell, and usually are proteins of the extracellular matrix (ECM), which is secreted by cells in tissues. In an *in vitro* experiment, the ECM proteins can either be absorbed from the medium during incubation or can be coated in a separate step of the protocol. Very often one also uses synthetic adhesion ligands, like the RGD-peptide motive common to many ECM proteins. Depending on cell type, adhering cells might secrete new ligands on the timescale of hours. However, usually this effect is not desired and the adhesion experiment is stopped at an earlier time point.

In principle, cell adhesion might also be mediated by non-specific interactions like the van der Waals attraction ubiquitous in soft matter systems. However, this is prevented by the glycocalix, a polymer brush surrounding every animal cells [11] (this mechanism is reminiscent of steric stabilization in solution of colloidal particles). By switching off non-specific adhesion, cells control which surfaces they adhere to. Therefore the gain in adhesion energy required to drive cell adhesion is mainly provided by specific adhesion. It is counteracted by cell elasticity, which is mainly provided by the actin cortex, a thin layer of actin gel underlying the plasma membrane of all animal cells. From a physical point of view, the balance of adhesion energy and elastic deformation determines the degree to which the cell can adhere over a finite contact area. This situation is depicted schematically in Fig. 1.3a. It resembles adhesion of other soft objects to flat substrates, e.g. of fluid droplets governed by the laws of Laplace and Young [86], of elastic spheres as described by contact mechanics [90], of vesicles [158], and of hollow capsules made from thin shells [152]. To model the elastic aspects of cell adhesion, in principle one should include both the effect of the thin shell elasticity of the actin cortex [70] and the effect of the lipid bilayer [158], as has recently been done for red blood cells in solution [107].

In contrast to the adhesion of inert soft objects, however, cell adhesion is an active process. The cell adhesion receptors driving cell adhesion not only provide a gain in adhesion energy, they also trigger cellular signaling cascades which lead to an active increase in contact area. This active element of cell adhesion is tightly regulated by signaling networks and consumes ATP. Eventually the cell tends to spread flat on the substrate like a pancake (or rather like a fried egg, because the nucleus is a rigid object which sticks out). From a physics point of view, one might think that some kind of viscoelastic flow leads to the flat morphology characteristic for mature adhesion on flat substrates. In practice, the cell's elasticity does increase rather than decrease during cell adhesion, thus the cell has to spread against its own elasticity. This is accomplished by rapidly polymerizing actin gels (*lamellipodia*), which push the cell envelope forward, and the build-up of strong adhesion contacts along the cell rim, which keep the cell in its tensed state. For animal cell types like fibroblasts and in contrast to the situation in physical adhesion, adhesion now is not homogeneous over some contact region, but localized to cell-matrix contacts called *focal adhesions*. They can be detected as dark areas in interference reflection microscopy [1] and as regions of close approach and high electron density in transmission electron microscopy [32]. Today it is common practice to monitor focal adhesions in real time and in live cells by using fluorescence constructs for one of the more than 50 different proteins localizing to focal adhesions. Fig. 1.3b shows a schematic presentation of the active part of cell adhesion, including the regions of polymerizing actin gel and the focal adhesions.

Although the resulting structure is already under large tension, in many situations mature adhesion is characterized by an additional active process, which further increases the mechanical load of the focal adhesions, namely the build-up of so-called *stress fibers*. Stress fibers are bundles of actin filaments set under tension by myosin II molecular motors. They end at focal

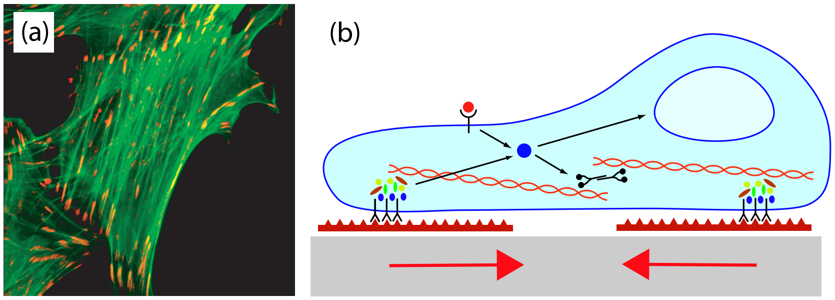

Figure 1.4: Mature adhesion to flat substrates is characterized by stress fibers and focal adhesions. (a) Fluorescence staining of an adhering fibroblast for actin (green) and the focal adhesion protein vinculin (red). (b) Schematic representation with one stress fiber and two focal adhesions. Force is generated by myosin II molecular motors interacting with actin filaments and transmitted to the extracellular environment through the focal adhesions. The traction pattern exerted onto the substrate is pinch-like. Signaling from focal adhesions activates motor activity and combines with other signals to determine gene expression and cell fate.

adhesions, which transmit the internally generated force onto the environment. Stress fibers can be considered to be little muscles, and indeed have been shown by α-actinin staining to contain a striated substructure. The force-generating activity of the molecular motors requires ATP and is known to be activiated by signals from the focal adhesions, in particular by the small GTPases from the Rho family. Fig. 1.4a shows a fluorescence picture of an adhering fibroblast with staining for actin (green) and the focal adhesion protein vinculin (red). One clearly sees that stress fibers end in focal adhesions, which in turn are elongated towards the direction of the stress fibers. In Fig. 1.4b, we show a schematic representation of the system of focal adhesions and stress fibers, which is characteristic for mature cell-matrix adhesion onto flat substrates.

During recent years, the molecular composition of focal adhesions has been studied in great detail [180, 181]. This has led to the following scenario. First small, dot-like adhesions form close to the lamellipodium, the so-called *focal complexes*. Depending on certain stabilization processes, they might mature into *focal adhesions*, which can achieve micrometer dimensions. Focal adhesions are usually connected to stress fibers and elongated in this direction. Often one observes that the whole focal adhesions translocates

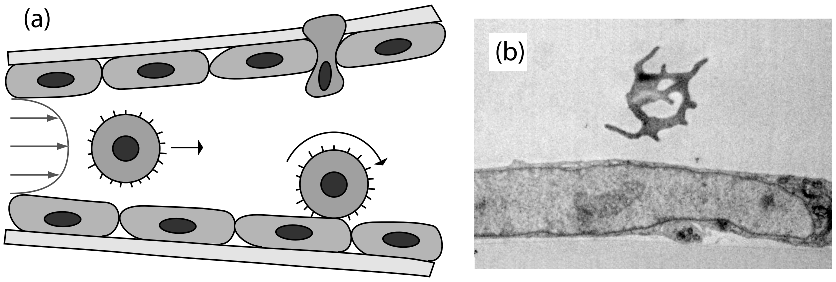

Figure 1.5: (a) White blood cells (leukocytes) circulate through the body in blood vessels. Near sites of inflammation they begin to roll on the vessel wall (*rolling adhesion*). The main agent of initial capture are L-selectin receptors which are localized to the tips of microvilli and bind to certain carbohydrate ligands on the endothelium. Depending on certain signals, the leukocytes might stop and leave the blood stream into the surrounding tissue and lymph (*extravasation*). (b) Transmission electron micrograph of a leukocyte with clearly exposed microvilli close to an endothelial sheet.

in time in the direction of the dominant stress fiber. Although this process is sometimes called *sliding*, it should not be confused with sliding of solid objects pulled by force over a substrate. Rather it reflects a growth process, where new material is added at the leading edge and old material is removed from the trailing edge. Often one also observes that focal adhesions separate into two parts, which the more rapidly translocating part moving quickly towards the cell center. This streak-like contacts are called *fibrillar adhesions* and tend to have a somehow different molecular composition than classical focal adhesions. In physiological settings like three-dimensional collagen gels, the molecular composition is somehow different [36], but in principle one expects that the same mechanisms are at work here as in the experiments on flat substrates.

1.3 Rolling adhesion

Traffiking of white blood cells (leukocytes) plays a central role in the body's immune response [145]. Inflammation of a tissue due to e.g. the presence of a pathogen causes nearby blood vessels to dilate. This changes the local hydrodynamic flow conditions and leukocytes, which constantly circulate with the blood stream, are driven to the wall, where they start interacting adhesively. Initial contact is mediated by adhesion molecules from the selectin family, which bind to certain carbohydrates. Adhering leukocytes begin to roll on the vessel wall in the direction of the blood flow, thereby constantly breaking old and forming new bonds. The rolling process enables them to survey the vicinity of the vessel wall for signs of inflammation. Subsequently they either return to the blood stream, or, on encountering certain signals, activate adhesion molecules from the integrin family, which bind more strongly than the selectins and eventually lead to firm arrest of the leukocytes. Finally the cell flattens and leaves the bloodstream towards the surrounding tissue, where it starts to sense certain chemotaxic gradients which allow it to home in on the pathogen. The multi-step process involving rolling on the endothelium, activation by chemokines, arrest, and transendothelial migration is called the *extravasation cascade* and is far from understood. Overexpression of selectin is known to lead to inflammatory responses (like in arthritis); therefore blocking selectins can help to treat chronic inflammatory disorders. Rolling adhesion is also one of the mechanisms which is used both by cancer and stem cells to travel the body; a better understanding of this process may help to prevent metastasis and to improve use of stem cells.

The interplay between hydrodynamics, elasticity and adhesion at play for rolling adhesion has been addressed both theoretically and in simulations [72, 20, 98, 30, 28]. An adhering cell in shear flow is lifted up by hydrodynamic flow, as investigated recently for vesicles both theoretically [155] and experimentally [117]. However, in physiological flow, the leukocytes are driven to the vessel walls by collisions with red blood cells. In flow chamber experiments monitored by video microscopy, leukocytes move very close to the chamber bottom where they make random contacts and then interact adhesively [5, 4]. A key molecule in this process is L-selectin, a leukocyte-expressed adhesion receptor which is localized to tips of microvilli and seems to be the main agent for initial cell capture. In contrast to tethering through other receptor systems like P-selectin, E-selectin or integrins, appreciable tethering through L-selectin and subsequent rolling only occurs above a threshold in shear [53], even in cell-free systems [3, 67]. Downregulation by low shear is unique for L-selectin tethers and might be necessary because L-selectin ligands are constitutively expressed on circulating leukocytes, platelets and on subsets of blood vessels. Quantitative analysis with normal video camera (time resolution 30 ms) of L-selectin tether kinetics in flow chambers above the shear threshold resulted in first-order dissociation kinetics, with an exponential dependance on force and a force-free dissociation constant of 6.6 Hz [5, 4, 30, 31]. This has been interpreted as signature of single L-selectin carbohydrate bonds. However, recent experiments using high speed camera (time resolution 2 ms) and theoretical analysis of the new data suggest that L-selectin tether stabilization involves multiple bonds and rebinding [44, 149].

1.4 Overview

The remainder of this work is divided into three chapters. In chapter 2, we will present a collaboration with cell biologists in which we developed a new method which allowed to measure single forces at focal adhesions for the first time [6, 151, 150]. The theoretical part of this project consists of numerically solving the ill-posed inverse problem of linear elasticity theory. The main result of this work is that there exists a linear correlation between internal force and size of focal adhesions. Because size in turn correlates with signaling, this indicates that focal adhesions act as mechanosensors which convert force into signaling and vice versa. In another study, the same collaboration was able to show that focal adhesions also act as mechanosensors in regard to external force [144]. In chapter 2, we will give an introduction into quantitative analysis of elastic substrates and present the details of our new method.

In chapter 3, we present models for the stochastic dynamics of adhesions clusters [48, 47]. This work is based on a Master equation for the temporal development of a cluster of parallel adhesion bonds, with the force-dependent transition rates following from Kramers theory. Our results can be used for quantitative evaluation of adhesion experiments and might be used in the future to understand more about the detailed mechanism of the mechanosensor at focal adhesions. Moreover, our results have been used in a collaboration with immunologists which for the first time showed that the shear threshold results from tether stabilization due to multiple bonds and fast rebinding [44, 149].

In chapter 4, we investigate how the information gathered at focal adhesions translates into cellular behaviour in soft media [153, 18, 17]. The main idea here is to model cellular force patterns as anisotropic force contraction dipoles and to describe effective cell behaviour as extremum principle in linear elasticity theory. Our predictions are derived from exact solutions of the elastic equations for different geometries and boundary conditions considered for the extracellular environment, and are in excellent agreement with experiments for fibroblasts both on elastic substrates and in collagen gels. In the future, our theory might be used for biomedical applications, e.g. for optimizing protocols for the design of tissue equivalents and implants, or for the design of elastic features on biochips.

Chapter 2

Forces at focal adhesions measured with elastic substrates

2.1 Introduction

The main technique to measure cellular forces is the elastic substrate method [13, 146], which has been introduced by Harris and coworkers in the early 1980s [76, 75]. In this work, the highly viscous, polymeric fluid polydimethylsiloxane (PDMS) was crosslinked at the surface by exposing it to heat. A thin elastic film over a fluid is obtained which under cell traction yields a wrinkled pattern which is characteristic of the pattern of forces exerted. Major improvements of the wrinkling substrates method include the tuning of the elastic compliance [24, 23]. However, deformation data can be analyzed only semi-quantitatively with this technique, since the buckling of thin polymer films is a non-linear phenomenon which is very difficult to treat in elasticity theory. Wrinkling can be suppressed by prestressing the film, thus allowing only for tangential deformation, which can be tracked by fluorescent latex beads dispersed within the film before crosslinking [103]. Quantitative analysis of elastic substrate data was pioneered by Dembo and coworkers. Using linear elasticity theory for thin elastic films and numerical algorithms for solving inverse problems, the forces exerted by keratocytes on the substrate could be reconstructed [40, 130].

For strong mammalian cells like fibroblasts, the non-wrinkling PDMS-films are too weak. By replacing PDMS with polyacrylamide (PAA) gels, a thick elastic substrate was achieved which is soft enough to deform under cell traction [135]. Like any isotropic elastic medium, it is characterized by two elastic constants. In several recent studies, a thick PAA-film with Young modulus $E \approx 6 - 24$ kPa and Poisson ratio $\nu \approx 0.5$ was used in order to quantitatively investigate traction of fibroblasts [42, 116, 12]. Since the marker bead displacements near the substrate surface are much smaller than the film thickness, they can be evaluated under the assumption that the thick film behaves like an elastic halfspace, whose elastic Green function is well known [99]. This allowed to reconstruct a continuous force field emanating from underneath the cell by using standard techniques for the solution of ill-posed inverse problems.

Recently, we developed a novel elastic substrate technique to measure cellular forces at the level of single focal adhesions (FAs) [6, 151, 150]. A thick polymer film made from PDMS with a Young modulus $E \approx 10 - 20$ kPa and Poisson ratio $\nu \approx 0.5$ was micro-patterned by standard lithographic techniques. Due to the regularity of the surface pattern, its deformation can be easily extracted from microscope pictures by an automatic procedure. Cell traction was generated by stationary, yet mechanically active cells (human foreskin fibroblasts, cardiac fibroblasts or cardiac myocytes) expressing GFP-vinculin. Vinculin is one of the major proteins of the submembrane plaque of FAs and can be tagged with green fluorescent protein (GFP) at its amino terminal. GFP-vinculin localizes at FAs and has good overlap with the dark areas in interference reflection microscopy [144]. In our setup, GFP-vinculin marks FAs with very high optical quality. The cells studied in our experiments show mature adhesion with well-developed FAs and stress fibers, and with little ruffling activity. We never observed traction near an area deprived of FAs, which allows us to assume that FAs are the main sites of application of force by the cells and to develop a numerical procedure which reconstructs discrete forces at sites of FA. The assumption of localized force necessitates several changes to the standard procedure. In this chapter, we address the details of our new computational method and show how the elastic substrate method is affected by the assumption of localized force. The concept of a force multipolar expansion is used in order to show under which experimental conditions one can neglect the details of the force distribution close to FAs and the finite thickness of the elastic substrate. We use systematic simulation of data in order to confirm that the inverse problem of linear elasticity theory is ill-posed for reasonable levels of noise and to show that

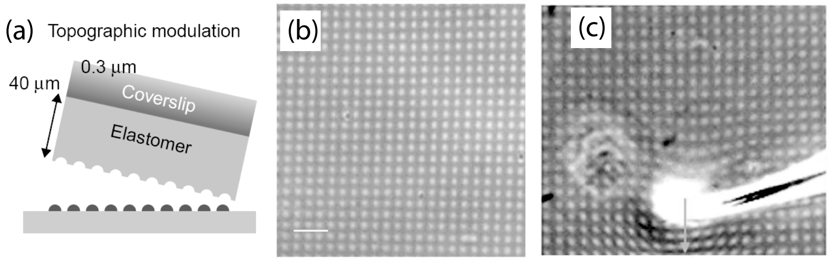

Figure 2.1: Fabrication of micro-patterned elastic substrates. (a) Peeling off the elastomer from the photoresist mould on a Si-wafer results in a topographic modulation of the film surface. (b) The topographic pattern can be easily detected in a phase-contrast image, but is sufficiently shallow (dot depth 0.3 μm) that cells do not react to it (space bar 6 μm) (c) When pulled with a micropipette with force 450 nN, the substrate shows elastic deformation in accordance with its macroscopically measured Young modulus of 19 kPa.

regularization in general cannot be neglected. Data simulation is also used in order to estimate both the spatial and force resolution of our method. Finally we report the main experimental results found with the help of the new method. Our results show that there is a close relationship between force and aggregation at focal adhesions, suggesting that they act as mechanosensors through which the cell can collect information on the mechanical properties of its environment.

2.2 Experimental method

The fabrication of micro-patterned elastic substrates is shown schematically in Fig. 2.1. A pattern of photoresist (Microposit S1805, Shipley) was produced on Si wafers using standard optical lithography. PDMS elastomer (Sylgard 184, Dow Corning) was poured onto glass coverslips, partially cured, put in contact with the photoresist pattern, and cured again. After peeling off, the PDMS film features a topographic modulation, which can be detected easily in phase-contrast microscopy. Typically, a 2 μm square lattice of 0.5 μm diameter dots with depth 0.3 μm was created on a 40 μm thick film. Varying the ratio of silicone elastomer to curing agent from 10:1 to 50:1 resulted in a Young modulus varying from 1000 to 12 kPa (the Poisson ratio was always close to 0.5). The elastic substrates was coated with fibronectin and cells (human foreskin fibroblasts, cardiac fibroblasts or cardiac myocytes) transfected with GFP-vinculin were plated onto them. Observations were made for mature adhesion, 10-60 h after plating. Identifying the dot centers in the phase-contrast pictures of substrates deformed by cell traction relatively to the undeformed substrates resulted in deformation data. Fluorescence pictures were processed by identifying clusters of GFP-vinculin, to each of which one ellipse was fitted. This resulted in data on position, size and elongation of focal adhesions (identified with midpoints, area and long axis of the ellipses).

2.3 Computational method

For adhesion onto a planar substrate, cultured cells usually adopt a flat morphology and cell traction is exerted onto the surface in a way which is essentially tangential. Therefore the force vectors can be assumed to be two-dimensional in the plane of the substrate surface. With a Young modulus E of the PDMS film around 10 kPa, cell traction leads to surface displacements of the order of 1 μm. Since this is much smaller than film thickness (40 μm), the substrate can be considered to be an elastic isotropic halfspace.

In the framework of linear elasticity theory, stress field $\mathbf{F}(\mathbf{r})$ and displacement field $\mathbf{u}(\mathbf{r})$ are related by a Fredholm integral equation of the first kind:

$$u_i(\mathbf{r}) = \int d\mathbf{r}' \; G_{ij}(\mathbf{r} - \mathbf{r}') F_j(\mathbf{r}') \tag{2.1}$$

where we apply the summation convention. In general, one has $1 \leq i, j \leq 3$. In our case, G_{ij} is the Green function of the elastic isotropic halfspace, which was calculated in the 19th century by Boussinesq [99]. The Boussinesq solution implies that for tangential traction and Poisson ratio $\nu = 0.5$, there is no out of plane displacement. Since our substrates have Poisson ratio ν close to 0.5, we can assume that the displacement vectors are two-dimensional in the x-y-plane. Therefore the whole elastic problem is two-dimensional, $1 \leq i, j \leq 2$. The Green function for the surface displacements for Poisson ratio $\nu = 0.5$ is

$$G_{ij}(\mathbf{r}) = \frac{3}{4\pi E r}\left(\delta_{ij} + \frac{x_i x_j}{r^2}\right) \tag{2.2}$$

with $r = |\mathbf{r}|$ and δ_{ij} the Kronecker Delta. For a given traction pattern $\mathbf{F}(\mathbf{r})$, the surface displacement $\mathbf{u}(\mathbf{r})$ follows from using Eq. (2.2) in Eq. (2.1). Note that the Green function is long ranged (it scales inversely with distance) and scales inversely with Young modulus E. The displacement following from a point force F scales as $u = l(l/r)$ with distance r, where $l = \sqrt{F/E}$ is the length set by force and rigidity. Therefore l is a measure both for typical displacements and for the decay length of elastic effects. As can be seen from the data presented below, we always have $|d\mathbf{u}/d\mathbf{r}| \ll 1$, thus linear elasticity theory is valid.

Experimentally, the displacement field $\mathbf{u}(\mathbf{r})$ is measured at different sites $\mathbf{r}_i$ $(1 \leq i \leq N)$ by image analysis. For this purpose we use the *water algorithm*, which has been described elsewhere [180]. In order to quantify the error related to the automatic determination of the centers of the spots, we used the water algorithm several times on the same picture in order to determine the positions of the grid. The standard deviation was found to be of the order of 1 pixel (0.133 μm). The same result was found when subtracting the displacement following from reconstructed force patterns from the experimentally measured displacement. The inverse problem of calculating forces from displacements amounts to inverting the Fredholm equation of the first kind from Eq. (2.1) with a discrete left hand side. However, this is not an easy task, since this kind of Fredholm integral equations and their discretizations are ill-posed. A problem is called *ill-posed* if its solution is not unique or if it is not a continuous function of the data. Fredholm integral equations of the first kind and their discretizations are ill-posed since they constitute smoothing operations which remove high-frequency components. Inverting the smoothing operation from Eq. (2.1) is an underdetermined problem (too much information has been lost during smoothing) which causes the solution $\mathbf{F}$ to be very sensitive to any change in $\mathbf{u}$. Ill-posed inverse problem can be solved by *regularization*, that is by including additional information which stabilizes the solution. They are a subject well investigated in numerical mathematics, and a number of regularization schemes are available for their solution [139, 74].

We approximate the cellular force pattern by an ensemble of point-like forces localized to the sites of focal adhesion. The different positions $\mathbf{r}_i$ $(1 \leq i \leq M)$ of the different focal contacts can be reconstructed from the fluorescence image with the water algorithm [180]. As will be argued below, we can assume that each focal contact corresponds to a point force $\mathbf{F}_i$ as long as we take care not to include displacements which are closer to a FA than its lateral extension. Since both forces and displacements are at discrete positions, the integral equation from Eq. (2.1) now becomes a set of linear equations, $\mathbf{u} = G\mathbf{F}$, where $\mathbf{u} = (u_1(\mathbf{r}_1), u_2(\mathbf{r}_1), u_1(\mathbf{r}_2), u_2(\mathbf{r}_2), \dots)$ is a $2N$-vector, $\mathbf{F} = (F_1(\mathbf{r}'_1), F_2(\mathbf{r}'_1), F_1(\mathbf{r}'_2), F_2(\mathbf{r}'_2), \dots)$ a $2M$-vector and G the following $2N \times 2M$-matrix:

$$\begin{pmatrix} G_{11}(\mathbf{r}_1 - \mathbf{r}'_1) & G_{12}(\mathbf{r}_1 - \mathbf{r}'_1) & G_{11}(\mathbf{r}_1 - \mathbf{r}'_2) & G_{12}(\mathbf{r}_1 - \mathbf{r}'_2) & \dots \\ G_{21}(\mathbf{r}_1 - \mathbf{r}'_1) & G_{22}(\mathbf{r}_1 - \mathbf{r}'_1) & G_{11}(\mathbf{r}_1 - \mathbf{r}'_2) & G_{12}(\mathbf{r}_1 - \mathbf{r}'_2) & \dots \\ G_{11}(\mathbf{r}_2 - \mathbf{r}'_1) & G_{12}(\mathbf{r}_2 - \mathbf{r}'_1) & G_{11}(\mathbf{r}_2 - \mathbf{r}'_2) & G_{12}(\mathbf{r}_2 - \mathbf{r}'_2) & \dots \\ G_{21}(\mathbf{r}_2 - \mathbf{r}'_1) & G_{22}(\mathbf{r}_2 - \mathbf{r}'_1) & G_{11}(\mathbf{r}_2 - \mathbf{r}'_2) & G_{12}(\mathbf{r}_2 - \mathbf{r}'_2) & \dots \\ \vdots & \vdots & \vdots & \vdots & \ddots \end{pmatrix} \tag{2.3}$$

Each experiment gives a displacement vector $\mathbf{u} \in R^{2N}$ and a Green matrix $G \in R^{2N \times 2M}$, which can be used to solve the inverse problem, that is to find the force vector $\mathbf{F} \in R^{2M}$. We use the usual χ^2-estimate, that is the quality of the estimate is measured by the sum of least squares $\chi^2 = |G\mathbf{F} - \mathbf{u}|^2/\sigma^2$ [139]. Here σ is the standard deviation of the distribution of measurement errors for the vector components of the displacement $\mathbf{u}$. χ^2-estimates are known to be useful even if the measurement errors are not normally distributed. Here we assume that this distribution is normal with the same standard deviation σ for each component of $\mathbf{u}$. Then the quantity χ^2 is drawn from a χ^2-distribution with $2(N - M)$ degrees of freedom, that is χ^2 has an average $2(N - M)$ and a standard deviation $\sqrt{4(N - M)}$.

In principle, the set of linear equations $\mathbf{u} = G\mathbf{F}$ can be solved by singular value decomposition. However, this procedure will in general not lead to reasonable results, since the problem at hand is ill-posed. This means that the singular values of the matrix G decay gradually to cero, thus the matrix G is ill-conditioned (in our analysis, condition numbers of the order of 1000 are typical). Following the usual procedure for discrete ill-posed inverse problems [139, 74], we now add a side constraint to the χ^2-minimization which in itself is not ill-posed and ensures a solution $\mathbf{F}$ which is robust. In more physical terms, the procedure aims at filtering out the parts of the displacement data which are due to noise. In the framework of Bayesian theory, the additional constraint is an *a priori* hypothesis about the physical nature of the expected solution.

The need for regularization necessitates two choices: which side constraint should be chosen in order to stabilize the inversion procedure, and how strongly this side constraint is enforced for each set of experimental data. The choice of the side constraint should be guided by physical considerations. The simplest choice is zero-order Tikhonov regularization, where one minimizes χ^2 under the constraint that the forces should not become exceedingly large:

$$\min_{\mathbf{F}} \left\{ |G\mathbf{F} - \mathbf{u}|^2 + \lambda^2 |\mathbf{F}|^2 \right\} \ . \tag{2.4}$$

The Lagrange parameter λ is called the *regularization parameter* since it parametrizes the trade-off curve between agreement with the given data (first term) and regularization (second term). For zero-order Tikhonov regularization, λ essentially determines below which level contributions from small singular values are filtered out of the solution. First and higher order regularization involves derivatives of F and should be chosen for enforcing smooth force fields. However, since neighboring focal adhesions can connect to different stress fibers, which might point in different directions, there is no reason to assume smooth force fields. Zero-order regularization both leads to a simple protocol for the numerical analysis and is the most reasonable choice in our case. The new target function is still quadratic in $\mathbf{u}$ and therefore again can be solved by singular value decomposition. For this numerical work, we used the package of Matlab routines *Regularization Tools* by P. C. Hansen. It can be found at Netlib (`http://www.netlib.org/`) in the file `numeralgo/na4`. Detailed explanations are provided in the book by the same author [74].

In order to choose the regularization parameter λ, we have used the χ-criterion [139] and the L-curve criterion [74]. The *χ-criterion* (also known as *discrepancy principle*) suggests that λ is chosen in such a way that the residual norm $R = |G\mathbf{F} - \mathbf{u}|^2$ as a function of λ assumes the value expected for an optimal fit, $2(N-M)\sigma^2$. The *L-curve criterion* suggests to determine the value of λ at which the residual norm starts to increase significantly as a function of λ. The name of this criterion comes from the fact that for discrete ill-posed problems, a plot of $\log |F|^2$ versus $\log |G\mathbf{F} - \mathbf{u}|^2$ very often has a L-shape. The corner of the L-curve corresponds to the optimal balance between data agreement and regularization, and it is this corner (which is intrinsic to the data at hand) which we detect with the L-curve criterion. One disadvantage of this method is that it introduces the need for a corner-finding algorithm. Another potential choice is the self-consistence criterion [82], which suggests that the regularization parameter λ is chosen in such a way that the resulting force pattern can be used to simulate displacement data which is consistent with the original set of data. Although this criterion is computationally expensive, the notion of self-consistence is very helpful in general. In particular, if σ is the standard deviation of the noise in the experimental data, then λ should be chosen sufficiently small that the standard deviation between experimental and reconstructed displacement equals σ.

2.4 Assumption of localized force and finite size effects

The lateral extension of FAs ranges up to few micrometers and can be visualized by GFP-labeling of FA-proteins like vinculin or paxillin. Initial and mature FAs are dot- and streak-like, respectively. In most cases, their shape resembles an ellipse with half axes a and b. Force is distributed over this area in a way which in general is unknown. However, as the distance to the force bearing region increases, details of the force distribution become less relevant for the determination of the displacement field. This is analogous to electrostatics, where the far field potential produced by a compact charge distribution is determined essentially by its highest multipole moment. In fact, the concept of a multipolar expansion can also be applied to elasticity theory. By expanding Eq. (2.1) for distances larger than the lateral extension of the force distribution, we find for the displacement field

$$u_i(\mathbf{r}) = \sum_{n=0}^{\infty} \frac{(-1)^n}{n!} \frac{\partial}{\partial x_{i_1}} \dots \frac{\partial}{\partial x_{i_n}} G_{ij}(\mathbf{r} - \mathbf{r}') P_{i_1 \dots i_n j} \tag{2.5}$$

where $\mathbf{r}'$ is some suitably defined midpoint of the force bearing region and the $P_{i_1 \dots i_n i}$ are its force multipoles

$$P_{i_1 \dots i_n i} = \int d\mathbf{s}\ s_{i_1} \dots s_{i_n} f_i(\mathbf{r}' + \mathbf{s}) \ . \tag{2.6}$$

The force monopole P_i is a vector which describes the overall force exerted from the force bearing region, and the force dipole P_{ij} is a second-rank tensor which describes pinch-like contractions or expansions. It follows from Eq. (2.2) that the displacements caused by force monopoles and force dipoles decay with distance like $1/r$ and $1/r^2$, respectively. The next term in the expansion of Eq. (2.5) is the force quadrupole P_{ijk}, that is a tensor of rank 3 which decays like $1/r^3$.

The major assumption of our numerical analysis will be that forces are exerted mainly at FAs and that the distributed force close to each FA can be approximated by its first multipole moment, the force monopole or overall force. In order to justify the mathematical part this assumption, we consider the following microscopic model for the force distribution over a FA. First, we assume that all of the distributed force is directed in the same direction. Second, we assume that the distribution of magnitude of force is Hertzian. This means that the force disappears continuously towards the rim and reaches its maximum in the middle. If we choose the x-axis to be the a-axis of the FA, we can write

$$\mathbf{F}(x,y) = \frac{3}{2\pi ab} \sqrt{1-\left(\frac{x}{a}\right)^2-\left(\frac{y}{b}\right)^2}\,\mathbf{F}_0 \ . \tag{2.7}$$

The corresponding force multipoles follow from Eq. (2.6). The force monopole $\mathbf{P} = \mathbf{F}_0$, the force dipole P_{ij} vanishes, and the force quadrupole has $P_{11i} = a^2 F_{0,i}/5$, $P_{22i} = b^2 F_{0,i}/5$ and vanishes otherwise.

We now consider how the displacement decays along the x- and y-axes for a force in x-direction; in these high symmetry directions, the displacement vector has a contribution only in x-direction, but it is easy to check that the following results also hold for arbitrary directions. For the monopole of our model, it follows from Eq. (2.5) that the displacement decays like $3F_0/2\pi Er$ along the x-axis and like $3F_0/4\pi Er$ (that is twice as fast) along the y-axis, respectively. For the quadrupole of our model, it follows from Eq. (2.5) that the displacement decays like $3F_0(a^2-b^2)/10\pi Er^3$ along the x-axis and like $3F_0(a^2+2b^2)/40\pi Er^3$ along the y-axis, respectively. For a symmetric FA, $a = b$, the contribution from the quadrupole vanishes along the x-axis. Along the y-axis, it becomes smaller than the contribution from the monopole for $r > \sqrt{3/10}a$. In general, a and b set the length scales over which the corrections to the monopole contribution become negligible. Thus we can expect the crossover between the displacement following from the distributed force and the displacement following from the force monopole to occur close to the rim of the FA, at a distance which is set by the size of the FA itself.

For our model force distribution, this conclusion can be checked numerically by using Eq. (2.2) and Eq. (2.7) in Eq. (2.1). In Fig. 2.2 we compare the full and approximate displacements (dashed and solid lines, respectively) for distributed force being directed parallel (upper row, a-c) and perpendicular (lower row, d-f) to the FA-elongation. Note that in contrast to the

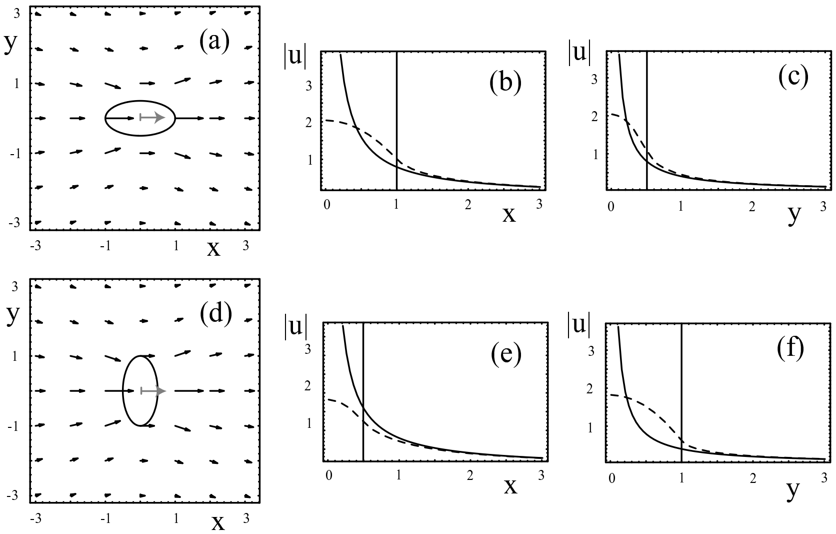

Figure 2.2: Theoretical model for force distribution over a finite-sized adhesion plaque like a focal adhesion: we assume that force points in x-direction and that its magnitude is distributed in a Hertzian manner over an ellipse. (a,b,c) Long axis of ellipse parallel to direction of force. (d,e,f) Long axis of ellipse perpendicular to direction of force. (a,d) Displacement following from the distributed force. (b,c,e,f) Dashed lines: magnitude of displacement following from the distributed force along the x- and y-directions (numerical result). Solid lines: magnitude of displacement following from equivalent point-like forces exerted at the origin (Boussinesq Green function). For Young modulus E = 6 kPa and overall force F = 10 nN, all distances are in μm.

displacement due to the point-like force monopole, the displacement due to the distributed force does not diverge at the origin (in fact it scales like F_0/Ea). As predicted from our multipole argument, it crosses over to the full solution (which scales like F_0/Er) close to the rim of the force-bearing region. In b and e, the magnitude of displacement is plotted along the x-axis, and in c and f, along the y-axis. In all cases, the crossover between full and approximate solutions occurs very rapidly outside the force-bearing regions, especially if the direction of force is parallel to the elongation of the focal adhesion. We conclude that as long as one does not consider displacements which are closer to a FA than the size of the FA itself, the divergence of the Green function is avoided and it is justified to approximate the distributed force exerted at a FA by a point force.

In our experiments, we used polymer films with thickness 40 μm and lateral size of a few cm. Typical displacements used during quantitative analysis were of the order of $\sqrt{F/E} \approx \mu$m, where $F = 10$ nN is the typical force at FAs and $E = 10$ kPa a typical value for the Young modulus. We now argue in more detail why finite size effects can be neglected in our treatment. In linear elasticity theory, forces and displacements are related by a second order differential equation. For a given force distribution, one first solves the *heterogeneous* differential equation for an infinite elastic medium. The resulting solution will be an inverse power of the distance and it will not be unique, since any solution to the *homogeneous* differential equation could be added to it. These additional solutions are called *image displacements* and will be polynominals in the distance. They can be used to statisfy the boundary conditions of the finite sized sample. For free and clamped surfaces, forces normal to the boundary and displacements have to vanish at the boundaries, respectively.

The Boussinesq Green function for an infinite elastic half-space is used throughout our work, although in principle one should use the Green function which also satisfies the clamped boundary conditions at the bottom and at the sides of the thick film. This Green function will be very complicated, but one can estimate its effect as follows. Conider one FA with overall force F. Then the displacement at a distance r scales as $u = F/Er$, while the image displacement scales as $u = cr$, where c is a dimensionless factor which has to be determined from the boundary conditions. For clamped boundary conditions, the two displacements have to cancel at $r = h$, where h is film thickness (a similar argument applies for the sides of the sample). Therefore $c = F/Eh^2 = (l/h)^2$, where $l = \sqrt{F/E}$ is the length scale set by forces and rigidity. Since l is also the length scale for displacements close to the FAs, c is negligible if displacements are much smaller than film thickness, as it is usually the case in elastic substrate experiments with thick films.

As explained above, the displacement at the position of the FA itself scales as F/Ea, where a is the size of the FA. If film thickness h decreases towards a, this scaling is changed to Fh/Ea^2 and our treatment is not valid anymore, since we neglect the effect of finite film size. Therefore an additional requirement for our method is that the size of FAs (or of a cluster of neighboring FAs if the corresponding forces point in the same direction) should be much smaller than the film thickness. Butler and coworkers recently used the same scaling argument to argue that cell size should be much smaller than film thickness, because they considered the case that stress is distributed uniformly over the whole cell [25]. However, in our analysis forces at different FAs (or at least at FAs in different parts of the cell) had different directions and therefore screen each other. In order to consider the effect of the whole cell, one should take at least into account that the vector sum of all forces will vanish due to Newton's third law. In the framework of the force multipolar expansion, the relevant term becomes the force dipole, and in fact force patterns from mechanically active cells often resemble pinching deformations. Below we analyse an experiment that shows that stationary fibroblasts might be considered to generate force dipoles of magnitude $P = -10^{-11}$ J. Then displacement decays as $u = P/Er^2$ and $c = P/Eh^3 = (l/h)^3$, where now $l = (P/E)^{1/3} \approx 10$ μm is the length scale set by force dipole and rigidity. Therefore the additional requirement now becomes that the length scale set by force dipole and rigidity should be much smaller than film thickness. Although both additional requirements discussed in this paragraph are somehow stronger than the usual one derived in the preceding paragraph, they are less drastic than the one suggested by Butler and coworkers and usually are satisfied in elastic substrate experiments with thick films.

2.5 Data simulation, regularization and resolution

Data simulation allows an accurate check of our method and to estimate its resolution. In Fig. 2.3a we show an artificial force pattern $\mathbf{F}_0$ which mimics traction by a polarized fibroblast as monitored in our experiments. The cell is assumed to be elongated, with FAs occuring close to the rim. Forces are assumed to be exerted only at the FAs at the lower and upper sides, which can be considered to be connected by stress fibers running parallel to the long axis of the cell. One test of our force reconstruction will be whether forces are generated at the focals at the sides which in the original pattern do not exert force. Neighboring forces along the upper and lower sides are separated by a distance of 4 μm and are assumed to alternate in magnitude, since this allows to test the resolution of our force reconstruction. Typical force is assumed to be 20 nN per FA. Fig. 2.3a also shows the displacement resulting from this force pattern. The relation between force and displacement is governed by the Young modulus E, which we assume to be 12 kPa (this is the smallest value

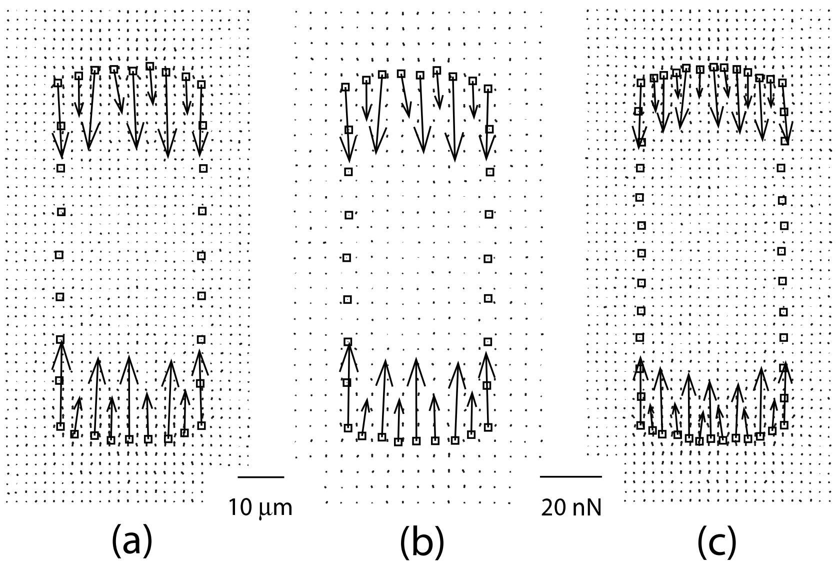

Figure 2.3: Artificial force patterns $\mathbf{F}_0$ mimicing traction by polarized fibroblasts and the resulting displacement fields $\mathbf{u}$. Young modulus E = 12 kPa. (a) Nine focals adhesions on each side with average distance 4 μm. The distance between the micro-fabricated dots is 2 μm. Typical magnitude of force is 20 nN. Displacement is subject to Gaussian noise with standard deviation $\sigma = 1$ pixel $= 0.133$ μm, largest displacement is 1.3 μm. (b) Same parameter values as in (a), but doubled distance between the micro-fabricated dots. (c) Same parameter values as in (a), but now there are 13 focal adhesions with distance 2 μm on each side.

obtained in our experiments). Displacements are calculated on a grid of dots with pitch 2 μm (like for the micro-patterned substrates) and are assumed to be subject to Gaussian noise with standard deviation $\sigma = 1$ pixel $= 0.133$ μm (this is the level of noise resulting from image processing with the water algorithm). Then the largest displacement picked up is 1.3 μm. Fig. 2.3b and Fig. 2.3c show two of the several changes to this reference case which we will discuss below: in Fig. 2.3b, the distance between micro-fabricated dots has been increased from 2 to 4 μm, and in Fig. 2.3c, the number of FAs has been increased from nine to 13 (thus the distance between FAs has been decreased from 4 to 2 μm).

In Fig. 2.4, we reconstruct the force pattern from the displacement data shown in Fig. 2.3a. In Fig. 2.4a, we plot residual norm $R = |G\mathbf{F}(\lambda) - \mathbf{u}|^2$

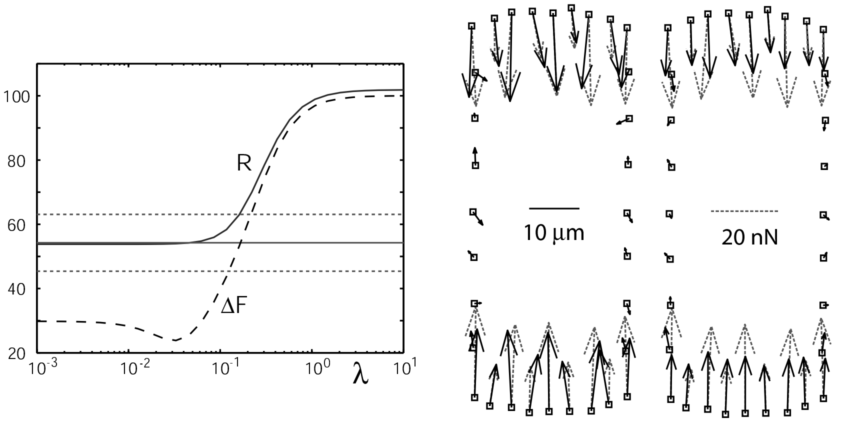

(a) (b) (c)

Figure 2.4: (a) Residual norm $R = |G\mathbf{F}(\lambda) - \mathbf{u}|^2$ (in absolute units) and deviation from original force $\Delta F = |\mathbf{F}(\lambda) - \mathbf{F}_0|$ (normalized to 100) as a function of regulariziation parameter λ for the force and displacement data from Fig. 2.3a. The solid and dotted straight lines indicate expectation value and confidence interval for the corresponding χ^2-estimate, respectively. For the choice of the regulariziation parameter λ, χ^2-criterion, L-curve criterion and the minimum in ΔF all suggest $\lambda = 0.04$. (b,c) Dashed and solid arrows are original and reconstructed forces, respectively. (b) Force reconstruction with $\lambda = 0.04$. Even for optimal reconstruction, some information is inevitably lost. (c) Force reconstruction with $\lambda = 0.1$. Regularization is too strong and spatial resolution is lost.

(in absolute units) and deviation from original force $\Delta F = |\mathbf{F}(\lambda) - \mathbf{F}_0|$ (normalized to 100) as a function of regulariziation parameter λ. For small regularization (small λ), maximal agreement with the data is achieved; the residual norm R nevertheless attains a finite value, since there is no force field which can exactly reproduce the displacements due to Gaussian noise. For large regularization (large λ), the force field vanishes and the residual norm levels off at the value $|\mathbf{u}|^2$. The solid and dotted straight lines indicate expectation value and confidence interval, respectively, for a χ^2-estimate. Its intersection with the R-curve suggests $\lambda = 0.04$ for the regularization. In fact this is also the value of λ for which R starts to rise as a function of λ, so this result agrees nicely with the L-curve criterion. More important, it also agrees with the minimum in ΔF, the deviation from the original force pattern. It

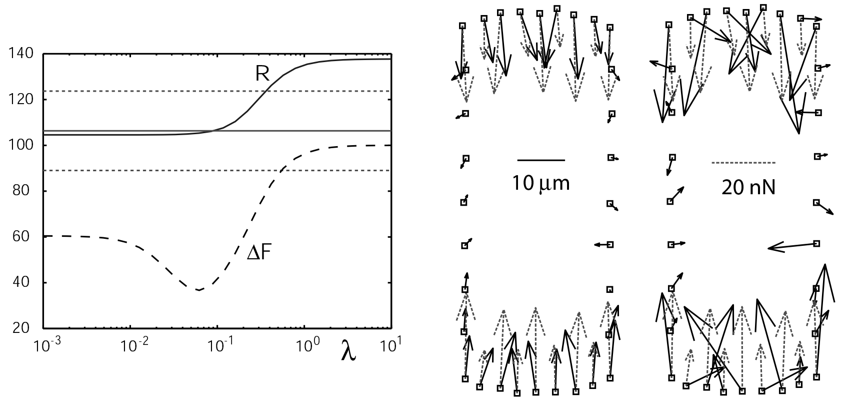

(a) (b) (c)

Figure 2.5: (a) Residual norm R and deviation from original force ΔF as a function of regulariziation parameter λ for the force pattern from Fig. 2.3a with the noise level increased to $\sigma = 2$ pixel $= 0.266$ μm. (b) Force reconstruction with $\lambda = 0.09$. Due to larger noise, more information is lost even for optimal regularization. (c) Force reconstruction without regularization ($\lambda = 0$) yields a rather erratic force pattern.

is important to note that even the optimal choice of λ cannot reproduce the original force pattern: Fig. 2.4a shows that ΔF has its minimum at 24 percent, that means a considerable part of the original information has been lost by the smoothing operation of the elastic kernel and cannot be retrieved by the inversion. This corresponds to a error of 4 nN for the reconstruction of the 20 nN original single force. The fact that ΔF rises again for smaller values of λ indicates the need for regularization: without regularization ($\lambda = 0$, ΔF = 30 percent), the agreement between reconstructed and original force is worse than for the proper value of regularization ($\lambda = 0.04$, ΔF = 24 percent). In Fig. 2.4b we plot the reconstructed (solid) and original (dashed) force pattern. Note that our method nicely reproduced the overall characteristics of the pattern: only small forces are generated at the sides, and for the forces at the upper and lower sides, both the directions and the alternating magnitudes are reproduced. In Fig. 2.4c, we show an example of larger regularization ($\lambda = 0.1$), which is still within the χ^2-interval and consistent with a noise level of $\sigma = 1$ pixel $= 0.133$ μm. Yet the resolution in the force magnitude is lost, and their values are estimated as being too low.

Until now we showed that for parameter values corresponding to our experiments, the spatial resolution can be considered to be better than 4 μm and the force resolution will be around 4 nN. We now demonstrate that for data containing less information than assumed here, force reconstruction will worsen considerably. In Fig. 2.5 we show the effect of a noise level increased to $\sigma = 2$ pixel $= 0.266$ μm. Monitoring R and ΔF as a function of λ (Fig. 2.5a) determines $\lambda = 0.09$ for optimal regularization, but this time ΔF is considerably higher (37 compared to 24 percent), and goes up to 60 percent for the case without regularization (compared to 30 percent for the reference case). As was to be expected, with increased noise, regularization becomes more relevant. Fig. 2.5b and Fig. 2.5c compare reconstructed and original force patterns for $\lambda = 0.09$ and vanishing λ, respectively. In the first case of optimal regularization, force reconstruction is worse than in Fig. 2.5b for less noise, and in the second case without regularization, the force pattern becomes rather erratic. In particular, now larger forces are generated at the sides, which compensate for lateral compression which in the original pattern results from the forces at the upper and lower sides.

We now return to a noise level of $\sigma = 1$ pixel $= 0.133$ μm, but decrease the density of micro-patterned dots, that is we pick up less displacements. The corresponding displacement data is shown in Fig. 2.3b: the distance between dots has been doubled from 2 to 4 μm. Fig. 2.6a shows that now the force reconstruction is even worse than in the case of increased noise: optimal regularization now corresponds to a 45 percent deviation in reconstructed from original force, and goes up to over 70 percent for the case without regularization. This drastic effect had to be expected, since the relevant information is stored in the displacements which are above the noise level, that is in the displacements close to FAs, of which now many are lost. We also confirmed that the reconstruction is not considerably improved when adding displacements farer away from the cell (data not shown). Note however that the procedure of choosing λ is not affected by adding data with little additional information.

In Fig. 2.6b and Fig. 2.6c, we show the effect of changing the distance between FAs from 4 μm to 2 μm and 7 μm, respectively (the displacement data for the first case is shown in Fig. 2.3c). In order to be able to compare the different case for the same level of noise, $\sigma = 1$ pixel $= 0.133$ μm, we adjusted the typical force in such a way that the largest displacement picked up remains close to 1.3 μm. This amounts to decreasing and increasing the typical force of 20 nN by about 5 nN, respectively. Then the deviation

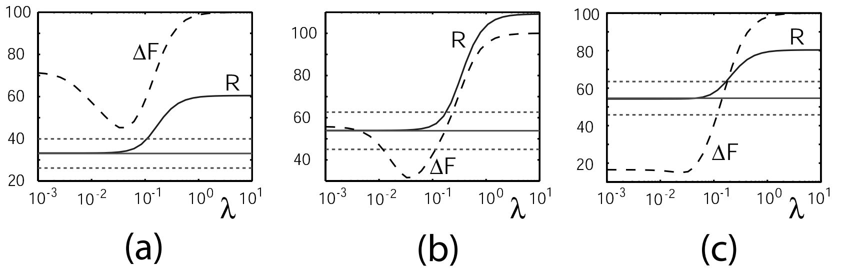

Figure 2.6: (a) Residual norm R and deviation from original force ΔF as a function of regulariziation parameter λ for the data from Fig. 2.3b, that is distance between micro-patterned dots is increased to 4 μm. (b) Same for data from Fig. 2.3c, that is there are 13 focal adhesions with distance 2 μm on each side. (c) Same for the case of five focal adhesions with distance 7 μm on each side. The more displacement is picked up and the larger the distance between focal adhesions, the better is the force reconstruction.

from original force at optimal regularization, which was 24 percent in the reference case, goes up to 31 percent and down to 15 percent for the two other cases, respectively. Although the corresponding standard deviations for single forces remain in the range of 4 nN, in the first case the spatial resolution is worsened, while in the second case it is improved. Moreover, in the case of well separated focal adhesions, regularization becomes less relevant: in Fig. 2.6c, there is only little difference in ΔF for all values of λ up to $\lambda = 0.04$, which is the level of optimal regularization.

2.6 Analysis of experimental data

As a control experiment, we first applied known forces to elastic substrates by lowering a micropipette onto the substrate and then shifting it tangentially (compare Fig. 2.1c for a phase-contrast image of such an experiment). In Fig. 2.7 we show the numerical analysis of such an experiment in terms of a point-like force applied at the midpoint of the micropipette contact region. The χ-criterion suggests $\lambda = 0.05$ (the L-curve criterion seems to suggest a somehow smaller value), which leads to a force estimate of F = 660 nN. A detailed analysis gives an error estimate of 13 nN. From the observed deflection of the micropipette, the applied force can be estimated to be 600 ± 90 nN, so the agreement is good. Note that the force applied by the

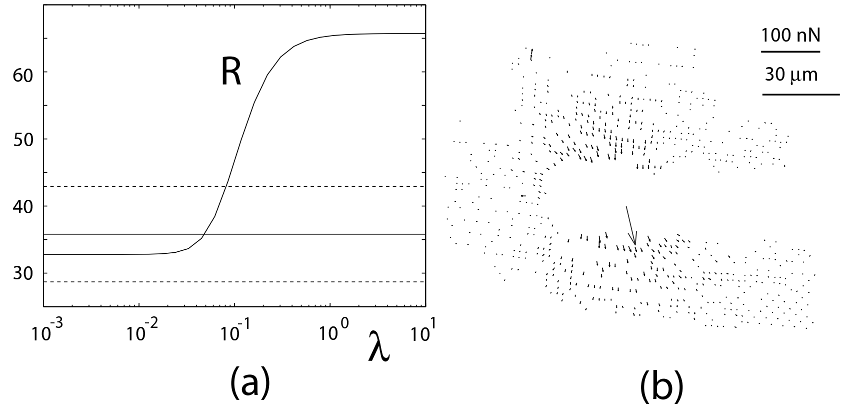

Figure 2.7: Analysis of a micropipette control experiment with one point-like force (Young modulus E = 12 kPa). (a) Residual norm R as function of regularization parameter λ. (b) Force reconstruction according to the χ-criterion ($\lambda = 0.05$). The result $F = 660 \pm 13$ nN for the overall force agrees with the experimental value $F = 600 \pm 90$ nN infered from the micropipette deflection.

micropipette is distributed, but since displacements are picked up only in the regions in which the field of view is not obscured by the micropipette, the force monopole approximation is appropriate. We also analyzed the same displacement data with increasing numbers of point forces distributed over the contact region and confirmed that this increases the estimate for the overall force only slightly. Moreover the different forces turn out to be more or less parallel (no twist) and decay if one moves away from the midpoint of the contact region.

The rigidity of our substrates has been optimized for studying traction from strong animal cells like fibroblasts and cardiac myocytes. In Fig. 2.8 we present the analysis for a whole human foreskin fibroblast. In order to resolve the displacement, such a high microscope resolution was needed that the cell did not fit into one single picture; the data presented here was assembled from two different pictures taken one after the other. Fig. 2.8a shows the resulting fluorescence picture for the whole cell, which is strongly polarized. Most FAs are located along the rim of the cell, and more or less elongated along the long axis of the cell itself. The residual norm R as a function of regularization parameter λ is shown in Fig. 2.8b. We see that the χ-criterion suggests $\lambda = 0.01$. However, the resulting regularization is

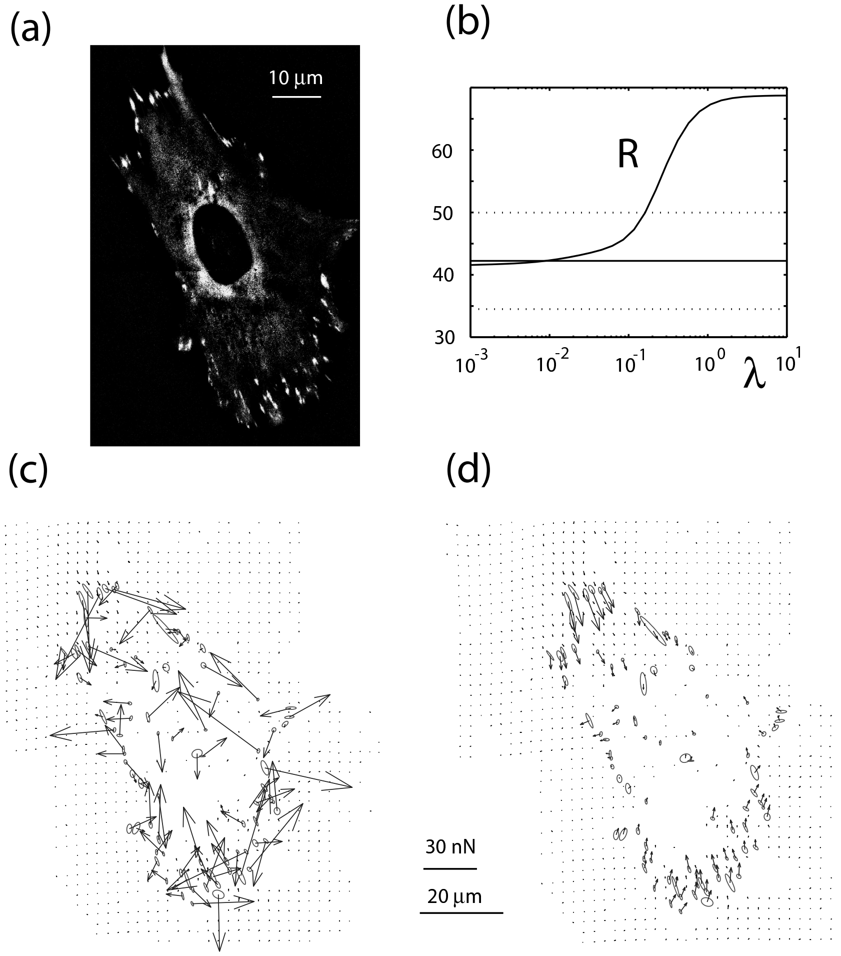

Figure 2.8: Cell traction from a stationary fibroblast (Young modulus E = 18 kPa). (a) Fluorescence image of the cell which is transfected with GFP-vinculin. Vinculin is a major component of focal adhesions and its localization is used to identifiy the regions which correspond to large forces. (b) Residual norm R as a function of regulariziation parameter λ for a whole human foreskin fibroblast. (c) Force reconstruction for $\lambda = 0.01$ (middle of χ-interval) and (d) $\lambda = 0.1$ (upper boundary of χ-interval). In (c), regularization is too weak, and the force pattern is erratic. In (d), there is an unexplained drift in the lower part of the force pattern, but the overall force pattern is reasonable. Ellipses are fits to the focal adhesions as marked by GFP-vinculin.

too weak, as can be seen from the resulting force pattern shown in Fig. 2.8c, which looks rather erratic. Therefore we use the upper boundary of the confidence interval, that is $\lambda = 0.1$, which is still consistent with the noise level (this choice also seems to be consistent with the L-curve criterion). The resulting force pattern is shown in Fig. 2.8d. Since we have fitted ellipses to the FAs in Fig. 2.8c and d, one sees clearly that for the stronger level of regularization, the forces in the upper part of the cell are more or less parallel to the elongation of the single FAs. This seems reasonable since one expects stress fibers to run in the same direction. In the lower part of the cell, the forces seem to be somehow rotated to the right. The main reason for this seems to be that displacement data is rather scarce in this region, so too much information has been lost as to achieve a reliable force reconstruction (the drastic effect of too little displacement information has been shown in Fig. 2.6a). We find that the force in the upper part can be as strong as 30 nN. In the lower part, most forces are in the order of 10 nN. Note that there are several small FAs at the sides which seem to carry only little force. In general, we find that the cell is highly polarized also in regard to the force pattern and that the two force bearing regions at the upper and lower sides more or less balance each other. Due to Newton's third law, the overall vector force is expected to vanish for a stationary cell, but in this analysis it amounts to 10 percent of the overall force magnitude, which is probabely due to the unreliable force reconstruction in the lower part of the cell. From the viewpoint of a force multipolar expansion, one might say that the cell forms a force contraction dipole of strength $P = -10^{-11} J$; this corresponds to a pair of forces, separated by a distance of 60 μm and each 200 nN strong. A similar result, $P = -3 \times 10^{-12} J$, was obtained by Butler and coworkers for a human airway smooth muscle cell [25].

Fig. 2.9 shows another analysis of a whole cell, this time of a cardiac myocyte. One clearly sees the striated organization of the actin system, which is typical for muscle cells. In fact in the experiment this cell was beating with approximately 1 Hz frequency, leading to periodic deformations of the elastic substrate, which is taken here at the peak value. Fig. 2.9 shows that the forces run more or less in parallel with the actin fibers and that opposing groups of forces tend to cancel each other. However, this data is difficult to analyse, because the regions of vinculin-rich adhesion are not clearly defined, thus the assumption of localized force might not be justified. For quantitative analysis, we therefore focused on those focal adhesions in fibroblasts which are well-separated from neighboring ones. Fig. 2.10 presents

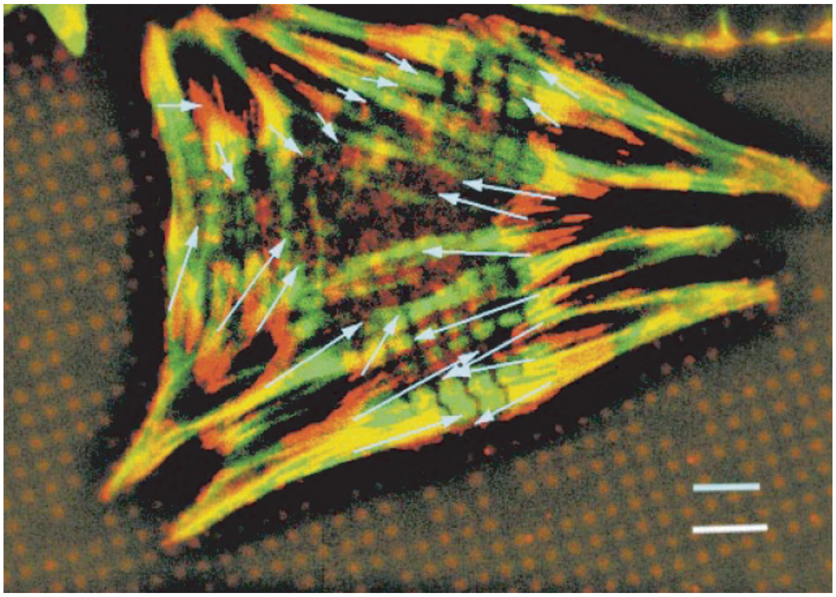

Figure 2.9: Distribution of forces in cardiac myocyte: staining for vinculin is shown in red, while staining for actin is shown in green (yellow are overlap regions). The light-blue arrows are force applied to the substrate at the vinculin-rich areas. White bar = 6 μm, blue bar = 70 nN.

our results in this respect. Fig. 2.10a shows that force and area show a linear relationship. Fig. 2.10b shows that the same holds true for the total fluorescence intensity, indicating that area and total intensity correlate well with each other, as found before [181]. Fig. 2.10c shows that the direction of force correlates nicely with the elongation of the focal adhesion. In Fig. 2.10d, displacements and forces are shown for a typical experiment, from which the quantiative analysis is made. Fig. 2.10e-h shows the effect of adding 15 mM 2,3-butanedione monoxime (BDM), which interferes with actomyosin contractility. As seen in Fig. 2.10h, as a result both aggregation area and force disappear at the focal adhesions. Fig. 2.10f and g show that the decay process for force and aggregation proceeds in parallel and is very fast, namely on the timescale of seconds, in accordance with the fact that the turnover time for proteins in focal adhesions is on the timescale of seconds [181]. Our main result is presented in Fig. 2.10e: a plot of area versus force including the BDM-data reveals a linear relationship between force F and area A at mature

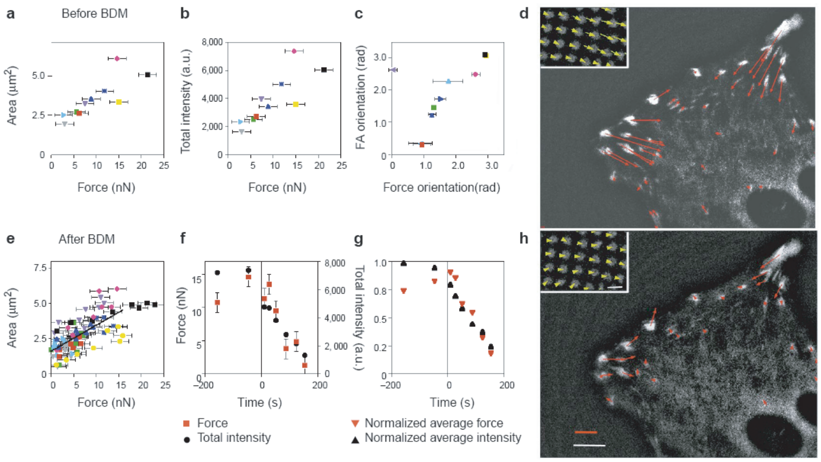

Figure 2.10: Correlation between force and size of focal adhesions. (a-d) Before and (e-h) after addition of 15 mM 2,3-butanedione monoxime (BDM), which interferes with actomyosin contractility. The green arrows in the insets in (d,h) show displacements. The red arrow in (d,h) show the calculated force. White bar = 4 μm, red bar = 10 nN, Young modulus = 12 kPa.

focal adhesions, A $\approx$ 1 μm^2 + 0.2 μm^2/nN F. The force-independent area of the focal adhesions is typical for focal complexes, which are the precursors of the large focal adhesions formed once force is applied. The force-dependent part of the relation implies a constant stress of 5.5 $\pm$ 2 nN/μm^2. We found the same value for the cardiac myocytes. Recently it has been confirmed in an independent study using smooth muscle cells plated on a bed of elastic microneedles [169].

2.7 Conclusions

In this chapter, we presented a novel computational technique which allows to calculate forces at the level of single focal adhesions (FAs) from displacement data of elastic (micro-patterned) substrates and fluorescence data of GFP-vinculin labeled FAs. Our main assumption is that forces exerted at FAs marked by fluorescent GFP-vinculin are appreciably higher than those developed in neighboring regions along the cell membrane. This assumption is based on the fact that we never observed traction near an area deprived of FAs. Our finding that large force corresponds to large FAs seems to justify our assumption *a posteriori*. Since displacements can be measured only at discrete points, the Fredholm integral equation relating forces to displacements is converted into a system of linear equations. The Boussinesq solution for the Green function of an elastic isotropic halfspace is used as kernel for the Fredholm equation. We showed in the framework of a force multipole expansion that the assumption of point-like forces is reasonable as long as displacements are picked up at a distance to the FAs which is similar to their lateral dimensions. The force multipolar expansion was also used to argue in detail why effects from the clamped boundary conditions at the bottom and at the sides of the polymer film can be neglected in our treatment.

It is well known that Fredholm integral equations of the first kind like the one of linear elasticity theory are ill-posed, irrespective of using the assumptions of localized or distributed force. By extensively simulating artificial data which mimic experimental conditions, we confirmed that in general the inverse elastic problem needs regularization in order to arrive at a reliable force estimate. In particular we showed that in most realistic cases, the deviation of reconstructed from original force ΔF shows a clear minimum at finite regularization parameter λ. In the absence of this information, that is in real experiments, one has to estimate the optimal value for the regularization parameter λ. We used two different criteria, the χ- (or discrepancy) criterion and the L-curve criterion, which lead to identical results for simulated data. For real data, the agreement between the two criteria is less good (possibly due to the presence of non-Gaussian noise or imperfections of the elastic substrate), but still sufficient. In the rare cases that these criteria lead to erratic force patterns (compare Fig. 2.8c), we used the upper limit of the χ-interval, since it is still consistent with the independently determined noise level.

It is important to note that spatial resolution for the force field is inherently restricted by the smoothing action of the Fredholm integral equation on the length scale $\sqrt{F/E} \approx \mu$m, where $F = 10$ nN is the typical force at FAs and $E = 10$ kPa a typical value for the Young modulus. Our simulations demonstrated that both spatial and force resolutions depend on the details of the displacement and force patterns. Although no generally valid values can be given, simulations for realistic situations showed that our spatial and force resolutions are better than 4 μm and 4 nN, respectively. This values have been derived above for a simulated reference pattern which is somehow more difficult to reconstruct than experimental force patterns, in which the high density of FAs of the reference pattern is realized only at certain regions of the cell. We conclude that calculated forces can be reliably attributed to single FAs if no other FAs are closer than a few μm. Although the smoothing action of the elastic kernel indicates a basic limitation of elastic subtrate experiments, it is worth noting that it also benefits our quantitative analysis, since it allows to neglect corrections arising from the modulation of the micro-pattern.

The method presented here can now be used to analyse mechanically active cells in quantitative detail. Experimentally, it requires the use of (micro-structured) elastic substrates and labeling of the force-transmitting system. We used GFP-vinculin to label FAs, but other possibilities include use of GFP-cDNA-constructs encoding other adhesion-associated proteins (like paxillin, zyxin, alpha actinin or actin) or specific antibodies. Numerically, it requires image analysis of the phase contrast and fluorescence pictures and use of the force reconstruction program. As the procedure described here is rather simple and robust, we expect that our protocol might become a standard tool for such a purpose. In contrast to the reconstruction of a continuous stress field [42, 116, 12], the reconstruction of a discrete force pattern is computationally rather cheap and needs only minutes on a standard PC. Therefore it could be used to study mechanical activity of cells in real time. Note that if the force-transmitting system cannot be marked, the standard assumption of distributed force has to be used.

It is interesting to consider which values for the rigidity should be chosen for an elastic substrate experiment. On the one hand, one expects that cells exert exactly the kind of forces which deform other cells. The effective Young modulus of a cell has been measured in AFM-experiments to be of the order of kPa [140]. PDMS-substrates as used in our study have somehow higher rigidities, but smaller rigidities can be achieved with other protocols or materials and could lead to larger deformations and a better signal-to-noise ratio. On the other hand, there are at least two reasons why the elastic substrate should not be too soft. First, in this case one would expect the force-generating cell to react in a specific way; in fact it has been observed that a elastic substrate which is very soft induces the cell to react by weakening the adhesion [135]. A systematic study of cell adhesion on substrates with varying elastic rigidity has shown that for fibroblasts there exists an optimal elastic substrate rigidity in the kPa range where the cells are maximally elongated [89]. Second, we explained above that the spatial resolution in such an experiment is limited to the length scale $\sqrt{F/E}$ due to the smoothing action of the elastic kernel. Thus, decreasing rigidity E leads to decreasing spatial resolution. Therefore elastic substrates with Young modulus of the order of kPa seem to be the right choice for the task at hand.

The main result of our work on cell traction on elastic substrates is that there exists a linear relationship between force and area of a FA, with an offset for area at vanishing force. This seems to indicate that the development of FAs is divided into two stages. In the initial stage, hardly no force is generated, and it can be speculated that this relates to the fact that integrin signaling suppresses Rho-signaling [142]. The later stage might be stimulated by Rho-signaling and might correspond to regular growth of a rather well-ordered supramolecular complex. This picture naturally explains the linear relationship, since now the addition of new components to the FAs adds a proportional amount of force. There seems to be a positive feedback loop acting between force and area. On the one side, larger area leads to increased signaling through Rho, including increased activity of myosin II molecular motors and thus larger force. On the other side, larger (external) force has been shown to lead to increased aggregation [144]. The mutual upregulation of force and aggregation cannot proceed without limits, and recent work suggests that the upper bounds are set by the action of microtubules inserting into mature focal adhesions and delivering some kind of stop-signal [165].

Our results suggest that focal adhesions act as mechanosensors converting force into protein aggregation and vice versa. In particular, cells can learn about the mechanical properties of their environment by monitoring the build-up of force at focal adhesions while pulling on it (*active mechanosensing*). In recent years, it has been shown that cells react in a typical way to the elastic properties of their environment, a phenomenon which has been termed *durotaxis*: most cell types upregulate their cytoskeleton and their cell-matrix contacts on stiff substrates [135], and locomote in favor of stiff or strained regions [116]. In principle, there are many different physical mechanisms which might be at work in the mechanosensor at focal adhesions. For example, it has been suggested that mechanosensing is based on force-induced conformational changes in specific FA-proteins like vinculin or on force-induced restructuring of the whole FA-complex [60, 59, 16]. Moreover a recent study has shown that the durotactic response is suppressed when stretch-activated ion channels are blocked with gadolinium [128]. Ion channels play a central role for mechanotransduction in the sensory systems [62], but the situation at focal adhesions is very different, since speed of response is not an issue here. In fact another recent study has shown that the aggregation response at focal adhesions under force persists even for permeabilized cells without any plasma membrane (that is without ion channels) [148]. Thus the exact mechanism at work in the mechanosensor is still an open issue, and in fact it is very likely that several mechanisms work in parallel here. In the next chapter, we will present a theoretical analysis of the rupture statistics in adhesion contacts, and discuss a possible relationship to focal adhesions. In the last chapter, we will explore how cells behave in a soft environment on the basis of the information gathered through the mechanosensor at focal adhesions.

Chapter 3

Stochastic dynamics of molecular bonds under force

3.1 Introduction

Biomolecular bonds are based on weak (non-covalent) interactions because in this way, biological systems can quickly rearrange in response to external stimuli. They have evolved specific structures which control not only the binding energy of the bond, but also the way ligands are guided into and out of the binding pocket. From a physics point of view, the simplest way to describe this situation is a one-dimensional potential energy landscape with one well representing the bound state and a transition state barrier separating it from the unbound state. Because biological systems are operating at finite temperatures, biomolecular bonds have evolved to function in the presence of thermal fluctuations. In principle, all biomolecular bonds will open at some point in time due to thermal fluctuations, which can overcome the transition state barrier between bound and unbound states. Naively, this implies that our own body should disintegrate with time. Obviously this is not happening, and the reason is that in physiological settings, rebinding stabilizes molecular bonds. However, the finite lifetime of specific bonds can be measured for single molecules, and more so for single molecules under force, which lowers the potential energy barrier stabilizing the bound state.

The mechanical opening-up of biomolecular bonds has become a subject of extensive research during the last decade or so, both experimentally and theoretically. The main experimental techniques in this field are atomic force

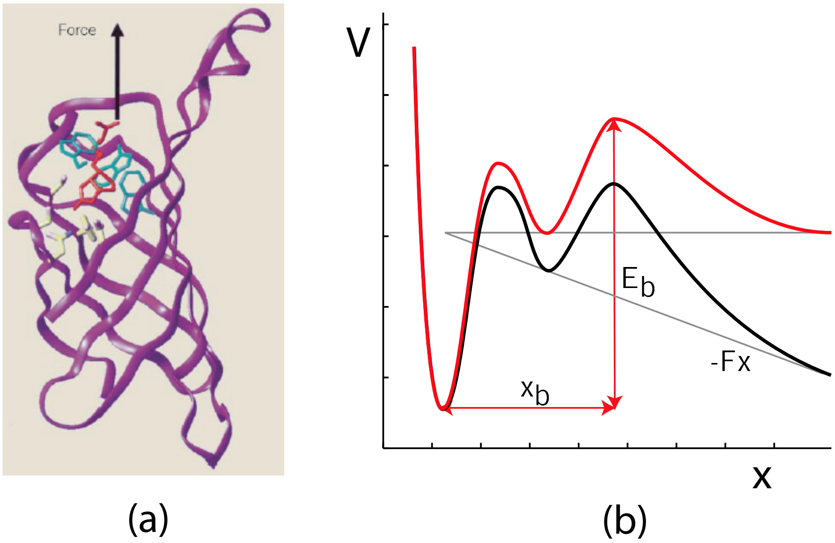

Figure 3.1: (a) Streptavidin-biotin bond: the large streptavidin molecule shown as ribbon diagram provides a binding pocket for the small biotin molecule. (b) Schematic representation of the energy landscape for the streptavidin-biotin interaction. The bound state to the left is separated by two transition state barriers from an intermediate state and the unbound state. Force tilts the energy landscape, with the effect being larger for the outer barrier. Each transition state barrier is characterized by barrier height E_b and separation to the bound state x_b.

microscopy (AFM) [54], laser optical tweezers (LOT) [93] and the biomembrane force probe (BFP) [124]. In AFM-experiments, bonds are attached to sharp tips mounted on soft cantilevers, which are moved on a piezostage. In LOT-experiments, bonds are attached to polymer beads, which are pulled into the focus of a laser beam due to dielectric effects. Finally, in BFP-experiments, bonds are attached to red blood cells, which are controled by micropipette aspiration. The main theoretical approaches in this field are Kramers theory (which describes thermally assisted escape over a transition state barrier) [51, 88, 160] and steered molecular dynamics (SMD) (atomic level simulations with force fields and an externally applied force) [69, 88]. The field of single molecule force spectroscopy was opened up by an AFM experiment from the Gaub group in 1994, which reported for the first time the mechanically induced unbinding of single biotin-strepatavidin bonds, with a binding strength of 140 pN [54]. In an experimental context, *binding strength* usually means the most frequent rupture force in the spectrum of rupture forces measured in different experiments. In a theoretical context, one might prefer the mean rupture force, but in most cases, the rupture force distributions feature a broad Gauss-like peak, thus the differences are small. Streptavidin (like the related molecule avidin) is a tetrameric glycoprotein with almost 8000 atoms that can bind up to four molecules of biotin. Biotin is a 32-atom vitamin which acts as an activated CO_2-carrier in some biochemical reactions. The biotin-avidin bond has an unusual high affinity ($K_d = 10^{-15}$ M), resulting in a lifetime of days. In Fig. 3.1a, a molecular representation is shown for the biotin-strepatavidin bond. In 1997, Evans and Ritchie pointed out that binding strength is not a static, but rather a dynamic quantity, which depends on the loading rate with which the bond is probed [51]. The faster one pulls, the less time thermal fluctuations have to assist unbinding, and the larger the binding strength will be (this is similar to the situation with commercial adhesive tapes, where fast loading also leads to large binding strength). Using Kramers theory for one transition state barrier, Evans and Ritchie predicted that the most frequent rupture force depends linearly on the logarithm of loading rate. For an energy landscape with several transition state barriers, they predicted a corresponding sequence of straight lines in the plot of binding strength versus logarithm of loading rate. Moreover, Evans and Ritchie conducted detailed computer simulations to predict the spectrum of unbinding strengths for biotin-avidin (based on energy landscape results from molecular dynamics simulations by other groups [69, 88]). Finally they pointed out that the binding strength of this bond will increase when investigated by LOT, BFP, AFM and SMD, respectively, because at that time, this sequence corresponded to increasing loading rates. The seminal paper by Evans and Ritchie gave a new name to the whole field, which is now called *dynamic force spectroscopy* (DFS) (for reviews, see [49, 87]). The theoretical analysis by Evans and Ritchie is in nice agreement with more sophisticated treatments by others [88, 160]. Still in 1997, the dynamic nature of binding strength was impressively confirmed by another AFM experiment from the Gaub group, namely mechanical unfolding of the large muscle protein titin [143]. At the same time, another titin pulling experiment from the Bustamante group with LOT gave conflicting results [93], which however can be explained by taking into account the role of the soft polymer linkages used in the experiments [52]. In 1999, the biotin-strepatavidin and biotin-avidin bonds were probed by an improved BFP-setup over a range of six orders of magnitude in loading rate, revealing bond strength ranging from 5 to 170 pN,

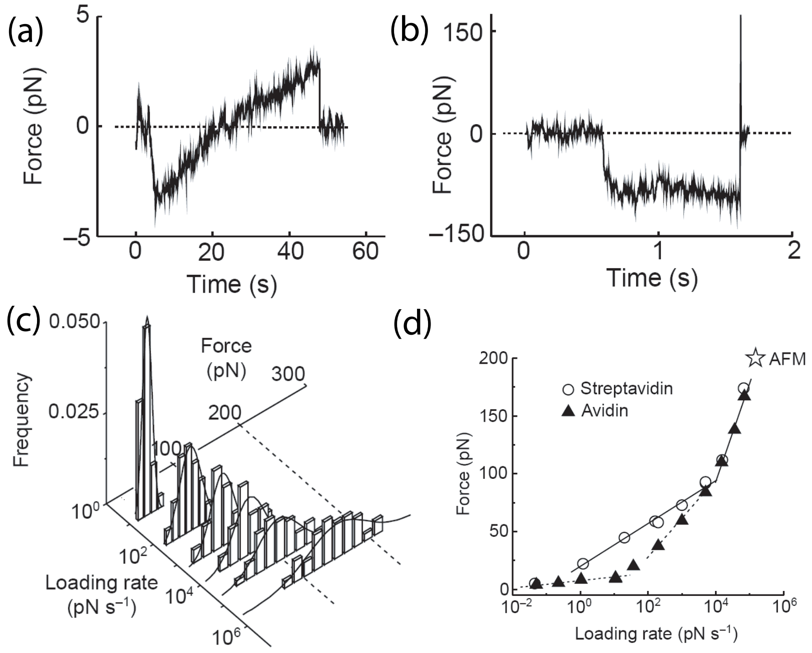

Figure 3.2: Dynamic force spectrosopy for biotin-avidin bonds with biomembrane force probe. (a) Slow loading gives long lifetime of 24 s and small bond strength of 3 pN. (b) Fast loading gives short lifetime of 0.003 s and large bond strength of 170 nN. (c) Rupture force histograms for loading rate varying over six orders of magnitude. (d) Most frequent rupture force varies like the logarithm of loading rate. Dynamic loading reveals two and three different transition state barriers for the streptavidin-biotin and avidin-biotin bonds, respectively.

compare Fig. 3.2 [124]. The same BFP-setup was also used to show for the protein A-IgG bond the crossover from spontaneous to force-induced bond dissociation with increasing loading rate [163]. During the last years, DFS has been used to characterize many more receptor-ligand systems, including some of the most important adhesion receptors, for example P-selectin [55], L-selectin [50], cadherin [8] and $\alpha_5\beta_1$-integrin [106].

Besides AFM, LOT and BFP, other experimental techniques have been employed for force-induced unbinding of biomolecular bonds, including the surface force apparatus [102], forced unbinding of adhering vesicles [71], micropipette techniques [33] and flow chambers [131, 182, 137]. Flow chambers are commonly used to study the adhesion of leukocytes to endothelium-like substrates. For diluted ligand, one usually observes first order dissociation kinetics, which traditionally has been interpreted as signature of single molecule events [5, 4]. Although recent results now point to a more complicated situation involving multiple bonds [44], flow chambers with diluted ligand can indeed be used to study single molecule unbinding, as has been done e.g. for biotin-avidin bonds [137].

Since thermal fluctuations are an integral part of DFS-experiments, theoretical analysis is essential for their evaluation. As already mentioned, the early work on single molecule force spectroscopy [54] received an adequate interpretation only after the theoretical analysis by Evans and Ritchie [51]. An important and still open question is what can be learned in principle about the energy landscape of molecular bonds from DFS-spectra (this can be called the inverse problem of DFS). Heymann and Grubmüller have developed an algorithm to reconstruct the enery landscape of molecular bonds from DFS-spectra [79]. A promising route is the use of a recently found exact theorem by Jarzynski which relates equilibrium properties to measurements of out-of-equilibrium processes [133].

In order to relate the features of DFS-experiments to molecular structure, the most promising approach is SMD. This method was pioneered in 1996 with a study of the streptavidin-biotin bond [69]. Later studies included forced unfolding of the avidin-biotin bond [88], titin [119] and fibronectin [96]. If one takes care to consider the effect of loading rate, reasonable agreement between theory and experiment can be achieved, e.g. for the biotin-avidin bond [124, 88]. The simulations show that the movement of the biotin molecule inside the binding pockets corresponds to a series of slips, each of which corresponds to the collective rupture of a group of hydrogen bonds. The experiment revealed three unbinding barriers, the first two of which can be identified with the slips found in the simulations. In Fig. 3.1b, a schematic sketch of the energy landscape of the biotin-avidin bond is shown as it emerged from the DFS-studies.

In the future, the rich spectrum of molecule properties now revealed by DFS has to be linked to their biological function. For example, it has been suggested that force-induced unbinding of fibronectin on the extracellular side [96, 159] and force-induced unbinding of certain cytoplasmic plaque proteins in focal adhesions (e.g. vinculin) [58, 59] might be involved in mechanosensory processes for tissue cells. In the same spirit, in rolling adhesion of leukocytes the specific behaviour of the selectin receptors under force is an essential part of effective cell capture and arrest [44, 28]. Recently, it has been reported that P-selectin, one of the three selectins involved in leukocyte rolling, might act as a catch bond, that is its lifetime increases under force (rather than decreases as for the regular slip bond) [121].

Regarding application of DFS to biological systems, it is very important to note that in cell adhesion, single molecules are the exception rather than the rule. Indeed most adhesion situations are based on clusters of molecular bonds. For example, cell-matrix adhesion is mainly provided by large focal adhesions, which can contain up to 10^5 integrin-mediated bonds, while an important part of cell-cell adhesion is provided by similarly large clusters of cadherin-mediated bonds [2]. Molecular bonds in a cluster can be arranged and loaded in different ways, including in parallel and serial ways, see Fig. 3.3. When probed in experiments with cells, the situation is further complicated by relaxation processes in the viscoelastic parts of the cell which act as force transducers. Then rather complicated force-extension curves result, even if they feature single molecule rupture events [14]. In order to arrive at general statements about the force-induced rupture of adhesion clusters, it is therefore favorable to start with simple generic situations, like clusters of parallel or serial bonds, with no special properties of the transducer. Parallel bonds loaded through a soft transducer are of special interest, because then force is shared equally between the closed bonds, thus leading to real cooperativity [10, 156]. When loaded through a stiff transducers, displacement rather than force is controled, all bonds feel the same force and a mean field theory can be used to make further progress [157]. Carefully designed experiments, for example uniform loading over a contact ring between a receptor-bearing cell and a ligand-bearing vesicle through a soft transducer [138], can be used to test the predictions of the theoretical models.

Since we are interested in understanding the role of force in cell adhesion, our main objective in this chapter will be to improve theoretical understanding of generic features of multiple bonds under shared loading. We start by recapitulating the most important results from recent advances in understanding *single* molecule force spectroscopy. In order to study cooperativity between bonds in a loaded adhesion cluster, we then introduce a stochastic model for rupture of *multiple* parallel bonds under shared loading. For the case of constant loading, we derive several new analytical results for special cases. For the general case, analytical progress seems hardly possible and we use numerical methods to solve the stochastic equations. The same holds true for the case of linear loading, which is of special interest for future DFS-experiments on multiple bonds.

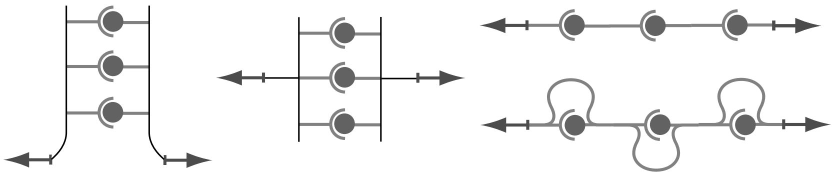

Figure 3.3: Different arrangements and loading scenarios for bonds in clusters. On the left, one bond is loaded after the other (serial loading), leading to a peeling process, e.g. for adhering cells in shear flow [41]. In the middle, all bonds are loaded simultaneously (parallel loading), which can be realized experimentally by moving the transducer perpendicular to the substrate [138]. On the right top, rupture of the first bond leads to complete failure. On the right bottom, this failure is prevented by an additional linker, like in the case of titin [143].

3.2 Single bond

Bond rupture can be modeled in the framework of Kramers theory as thermally activated escape over a sharp transition state barrier [51]. In the absense of force, the rate for barrier crossing k_0 depends on barrier height E_b as $k_0 = e^{-E_b/kT}/t_D$ [95, 73]. Here $kT = 4.1$ pN nm is thermal energy at room temperature and t_D is attempt time, which for biomolecular bonds is on the scale of nanoseconds. With a typical value for non-covalent binding, $E_b = 20$ kT, k_0 is on the scale of seconds, as it is typical for biomolecules. In the framework of Kramers theory, force applied to the bond tilts the energy landscape through an additional term $-Fx$. A sharp transition state barrier is therefore lowered by $-Fx_b$, where x_b is the distance between bound state and barrier along the linear reaction coordinate. This sets an internal force scale $F_b = k_BT/x_b$. With a typical value $x_b = 1$ nm, we have $F_b = 4$ pN. For the transition rate, we now have

$$k(t) = k_0 e^{F(t)/F_b} \ . \tag{3.1}$$

This is the famous Bell equation proposed in a seminal paper by Bell [10], although it was only later rationalized in the framework of Kramers theory [51, 88, 160].

We now discuss in detail the dependence of binding strength on loading rate. It has been shown by Shillcock and Seifert [160] that the adiabatic approximation used by Evans and Ritchie [51] is valid over a large range of parameter values. In the adiabatic approximation, one assumes that the escape process takes no time, thus the probability to rupture between t and $t+dt$ is $p(t)dt = k(t)S(t)dt$, where $k(t)$ is instantaneous rupture rate and $S(t)$ is the cumulative probability for survival up to time t. This quantitiy satisfies the relation

$$S(t+dt) = S(t)(1 - k(t)dt) \tag{3.2}$$

therefore

$$\frac{dS(t)}{dt} = -k(t)S(t) \tag{3.3}$$

and

$$S(t) = e^{-\int_0^t dt\ k(t)}\ . \tag{3.4}$$

In the adiabatic approximation, bond lifetime then follows as

$$T = \int_0^\infty dt\ t\ p(t)\ . \tag{3.5}$$

The simplest case is constant loading. Then $k(t)$ is independent of time, $S(t) = \exp(-kt)$, $p(t) = k\exp(-kt)$ and $T = 1/k$. This is nothing else than the classical Poisson process, or, in the language of chemical kinetics, first order dissocation.

For linear loading, $F = rt$ with loading rate r, Eq. (3.1) becomes

$$k(t)dt = k(\tau)d\tau = e^{\mu\tau} \tag{3.6}$$

where we have defined dimensionless time $\tau = k_0 t$ and dimensionless loading rate $\mu = r/k_0 F_b$. Then the probability of still being attached is

$$S(\tau) = e^{-\frac{1}{\mu}(e^{\mu\tau}-1)} \tag{3.7}$$

and the probability to rupture is

$$p(\tau) = S(\tau)k(\tau) = e^{-\frac{1}{\mu}(e^{\mu\tau}-1)+\mu\tau}\ . \tag{3.8}$$

In the following we are interested in the case $\mu > 1$, when rupture is induced by external loading (rather than by internal dissociation). While $S(\tau)$ decreases like in a Poisson process, $k(\tau)$ increases due to increased loading and as a consequence $p(\tau)$ has a peak at a finite time, which corresponds to the most frequent rupture event (for $\mu < 1$, the distribution peaks at vanishing time, because the bond dissociates internally in a Poissonian way). We change variables from τ to $f = F/F_b = \mu\tau$:

$$S(f) = \frac{d\tau}{df} S(\tau) = \frac{1}{\mu} e^{-\frac{1}{\mu}\int_0^f df' e^{f'}} = \frac{1}{\mu} e^{-\frac{1}{\mu}(e^f - 1)} \tag{3.9}$$

and therefore

$$p(f) = \frac{1}{\mu} e^{-\frac{1}{\mu}(e^f - 1) + f} \ . \tag{3.10}$$

For $\mu > 1$, this function has a maximum at f^*, which is the most frequent rupture force:

$$f^* = \ln \mu, \qquad F^* = F_b \ln \frac{r}{k_0 F_b} \ . \tag{3.11}$$

Thus rupture is a stochastical event with most frequent rupture force being proportional to the logarithm of loading rate. For the most frequent rupture time we have

$$\tau^* = \frac{f^*}{\mu} = \frac{\ln \mu}{\mu}, \qquad t^* = \frac{F_b}{r} \ln \frac{r}{k_0 F_b} \ . \tag{3.12}$$

Since the full probability distribution is known, one can also calculate the most probable rupture force and higher moments. This has been done by Tees and coworkers [170], who find

$$\langle f \rangle = e^{1/\mu} E(1/\mu) \tag{3.13}$$

where E is the exponential integral. For $\mu > 1$, we can expand for small arguments:

$$\langle f \rangle = \ln \mu - \gamma + O(1/\mu) \tag{3.14}$$

where $\gamma = 0.577$ is the Euler number. Thus for large loading rates, we get the same result for the average value as for the peak value. For $\mu < 1$, we can expand for large arguments:

$$\langle f \rangle = \mu + O(\mu^2) \ . \tag{3.15}$$

With vanishing μ, the bond decays by itself at cero force.

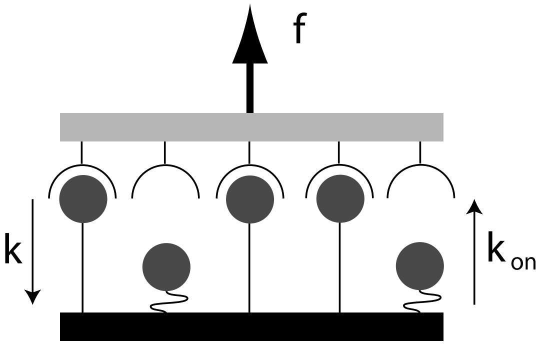

Figure 3.4: Schematic representation of our stochastic model for an adhesion cluster under shared force: in this case, there are $N_t = 5$ receptor-ligand pairs, of which $i = 3$ are closed and equally share the dimensionless force f. Single closed bonds rupture with dissociation rate $k = k_0 e^{f/i}$ and single open bonds rebind with force-independent association rate k_{on}. Our model has three parameters: cluster size N_t, dimensionless rebinding rate $\gamma = k_{on}/k_0$ and dimensionless force f.

We finally consider the composition of linear and constant loading, that is a ramp of force followed by a plateau. Thus there is linear loading $f = \mu\tau$ until time τ_0, followed by constant loading $f = f_0$. Note that there are only two independent parameters, τ_0 and f_0, since $\mu = f_0/\tau_0$. For the mean lifetime we find

$$T = \frac{e^{\frac{1}{\mu}}}{\mu}\left(E(\frac{1}{\mu}) - E(\frac{e^{\mu\tau_0}}{\mu}) + \frac{\mu}{e^{f_0}}e^{-\frac{e^{\mu\tau_0}}{\mu}}\right) \ . \tag{3.16}$$

Two limites are easily checked: for $\tau_0 \to 0$, we find the result for constant loading, $T = 1/e^{f_0}$, and for $\tau_0 \to \infty$, we find the result for linear loading, $T = e^{1/\mu}E(1/\mu)/\mu$.

3.3 Stochastic model for multiple bonds

We now turn to the case of multiple bonds. We consider a cluster with a constant number N_t of parallel bonds. At any time t, i bonds are closed and $N_t - i$ bonds are open ($0 \leq i \leq N_t$). Again we use dimensionless variables: dimensionless time $\tau = k_0 t$, dimensionless single molecule dissociation rate k/k_0 and dimensionless overall force $f = F/F_b$. Note that in general f can be time-dependent, $f = f(\tau)$. The i closed bonds are assumed to share force f equally, that is each closed bond is subject to the force f/i. This corresponds to loading through a soft transducer [156]. We also assume that each closed bond can rupture with the dissociation rate $k = e^{f/i}$, which corresponds to the case of one sharp transition state barrier along the rupture path [10, 51]. As long as the receptors are hold in proximity to the ligands, rebinding of open bonds can occur. Therefore we will assume that single open bonds rebind with the force independent association rate k_{on}. The dimensionless rebinding rate is defined as $\gamma = k_{on}/k_0$. Fig. 3.4 shows a cartoon of the situation described by our model.

Since bond rupture is a discrete process, the stochastic dynamics of the bond cluster can be described by a one-step Master equation [81, 64]

$$\frac{dp_i}{d\tau} = r_{i+1}p_{i+1} + g_{i-1}p_{i-1} - [r_i + g_i]p_i \tag{3.17}$$

where $p_i(\tau)$ is the probability that i closed bonds are present at time τ. The reverse and forward rates between the different states i follow from the single molecule rates as

$$r_i = ie^{f/i} \ , \quad g_i = \gamma(N_t - i) \ . \tag{3.18}$$

Depending on the experimental setup, rebinding from the completely dissociated state ($i = 0$) might be possible (*reflecting boundary*) or not (*absorbing boundary*). For $f = 0$ and a reflecting boundary at $i = 0$, we deal with natural boundaries, that is given reasonable initial conditions, no special equations are needed to treat the boundaries. For finite f, $r(0) = 0$ is required to prevent i from becoming negative. $g_0 = \gamma N_t$ represents a reflecting boundary for the completely dissociated state $i = 0$. In this case, the cluster will always regain stability and cluster lifetime T will be infinite. Since adhesion clusters (like single molecules) usually cannot rebind from the completely dissociated state due to elastic recoil of the transducer, we are mainly interested in an absorbing boundary at $i = 0$, which can be implemented by setting $g_0 = 0$. In this case, cluster lifetime T is the mean first passage time to reach the absorbing state $i = 0$. A full stochastic solution amounts to finding the set of state probabilities $p_i(\tau)$ as a function of the three dimensionless parameters N_0, γ and f. Below we will show that analytical solutions can be found for some special cases. In all other cases, the Master equation has to be solved numerically. For this purpose, we will use the Gillespie algorithm for efficient Monte Carlo simulations [61].

A quantity of large interest is the mean number of closed bonds, $N = \langle i \rangle = \sum_{i=1}^{N_t} i p_i$. From the Master equation Eq. (3.17), one can derive [81]

$$\frac{d\langle i \rangle}{dt} = -\langle r_i \rangle + \langle g_i \rangle \tag{3.19}$$

If r and g are both linear functions in i, Eq. (3.19) becomes an ordinary differential equation for N. This suggests to study the following deterministic equation

$$\frac{dN}{d\tau} = -N e^{f/N} + \gamma(N_t - N) \tag{3.20}$$

as has been done by Bell [10] for constant loading and by Seifert [156] for linear loading. However, for finite force f solution of Eq. (3.20) does not give the correct result for the first moment, since then the rate r defined in Eq. (3.18) is non-linear in i and the average in Eq. (3.19) cannot be taken. Instead, this equation now involves higher moments, so one ends up with a potentially infinite system of coupled differential equations. The same problem arises for higher moments. For example, for the second moment we have [81]

$$\frac{d}{dt}(\langle i^2 \rangle - \langle i \rangle^2) = 2\langle i g_i \rangle - 2\langle i r_i \rangle + (1 - 2\langle i \rangle)\langle g_i \rangle + (1 + 2\langle i \rangle)\langle r_i \rangle \tag{3.21}$$

which again involves higher order moments if r or g are non-linear function of i. It is also important to note that only the reflecting boundary leads to a deterministic equation like Eq. (3.20). For an absorbing boundary, a corresponding differential equation is not available, because the boundary condition is not natural, that is g_i does not obey the general form Eq. (3.18) for the special value $i = 0$ [81]. Thus this case can be studied only in the stochastic description Eq. (3.17).

Below we will present a detailed investigation of the stochastic model, both for constant [48] and linear loading [47]. In particular, we will compare the stochastic results with results for the deterministic model, which can be obtained by integration and scaling analysis of Eq. (3.20). Here cluster lifetime T can be identified with the time at which only one last bond is left, that is by $N(T) = 1$.

It is important to note that the difficult part of our analysis is the non-linear form of the reverse rate r_i, which follows from the Bell equation. In the force-free case, $f = 0$, the exponential factor vanishes and we deal with the well-known case of a linear one-step Master equation, which for a reflecting (i.e. natural) boundary can be solved with the help of a generating function, as has been done by McQuarrie [122]. We start by defining the generating function:

$$G(s,\tau) = \sum_{i=0}^{N_t} s^i p_i(\tau) \ . \tag{3.22}$$

Here the discrete index i is transformed to the continuous variable s. The back transform is

$$p_i(\tau) = \frac{1}{i!} \left. \frac{\partial^i G(s,\tau)}{\partial s^i} \right|_{s=0} \tag{3.23}$$

and the moments can be constructed as

$$\langle i^k \rangle = (s\frac{\partial}{\partial s})^k G(s,\tau)|_{s=1} = \left. \frac{\partial^k G(s,\tau)}{\partial (\ln s)^k} \right|_{s=1} \ . \tag{3.24}$$

The generating function has to satisfy the following differential equation:

$$\frac{\partial G}{\partial \tau} = \left[(\frac{1}{s} - 1) r(s\frac{\partial}{\partial s}) + (s-1) g(s\frac{\partial}{\partial s}) \right] G \tag{3.25}$$

where the reverse and forward rates r_i and g_i from Eq. (3.18) can be used as functions $r(i)$ and $g(i)$ of i due to the natural boundary. With $N(0) = N_0$, boundary and initial conditions are

$$G(1,\tau) = 1,\ G(s,0) = s^{N_0} \ . \tag{3.26}$$

The first moment is

$$N(\tau) = \langle i \rangle = \sum_{i=0}^{N_t} i p_i(\tau) = \left. \frac{\partial G(s,\tau)}{\partial s} \right|_{s=1} \tag{3.27}$$

and the variance is

$$D(\tau)^2 = \langle i^2 \rangle - \langle i \rangle^2 = \left. \frac{\partial^2 G}{\partial s^2} \right|_{s=1} + \left. \frac{\partial G}{\partial s} \right|_{s=1} - \left(\left. \frac{\partial G}{\partial s} \right|_{s=1} \right)^2 \ . \tag{3.28}$$

For the rates given in Eq. (3.18), specified to $f = 0$, we have the following differential equation:

$$\frac{\partial G}{\partial \tau} = (1 + (\gamma - 1)s - \gamma s^2)\frac{\partial G}{\partial s} + N_t\gamma(s-1)G \ . \tag{3.29}$$

For $N_0 = N_t$, its solution reads

$$G(s,\tau) = \left(\frac{(s-1)e^{-(1+\gamma)\tau} + 1 + \gamma s}{(1+\gamma)}\right)^{N_0} \ . \tag{3.30}$$

Using Eq. (3.23), we can derive the full solution of the stochatic equations:

$$p_i(\tau) = \binom{N_0}{i}\frac{\left(\gamma + e^{-(1+\gamma)\tau}\right)^i\left(1 - e^{-(1+\gamma)\tau}\right)^{N_0-i}}{(1+\gamma)^{N_0}} \ . \tag{3.31}$$

For the expectation value, we get

$$N(\tau) = \left.\frac{\partial G(s,\tau)}{\partial s}\right|_{s=1} = \frac{N_0}{(1+\gamma)}(\gamma + e^{-(1+\gamma)\tau}) \ . \tag{3.32}$$

Since here we deal with linear rates and the reflecting boundary, this results can also be derived directly from the deterministic equation for N, Eq. (3.20), which now reads

$$\frac{dN}{d\tau} = -N + \gamma(N_0 - N) \ . \tag{3.33}$$

It can be rewritten as

$$\frac{dN}{(1+\gamma)N - \gamma N_0} = \frac{1}{(1+\gamma)}\frac{d((1+\gamma)N - \gamma N_0)}{(1+\gamma)N - \gamma N_0} = -d\tau \tag{3.34}$$

therefore

$$N(\tau) = \frac{N_0}{(1+\gamma)}(\gamma + e^{-(1+\gamma)\tau}) \tag{3.35}$$

as above. For $\gamma = 0$ (no rebinding), we get the usual Poisson process. For finite γ, the fraction of bonds reaches a finite value $N_{eq} = \gamma N_0/(1+\gamma)$ on the time scale $1/k(1+\gamma) = 1/(k + k_{on})$. We can also evaluate the variance:

$$D(\tau)^2 = \frac{N_0(\gamma + e^{-(1+\gamma)\tau})(1 - e^{-(1+\gamma)\tau})}{(1+\gamma)^2} = \frac{N(\tau)(1 - e^{-(1+\gamma)\tau})}{(1+\gamma)} \ . \tag{3.36}$$

Thus we obtain the expected result that the effect of fluctuations diminishes like the inverse square root with increasing system size ($D/N \sim 1/N^{1/2}$).

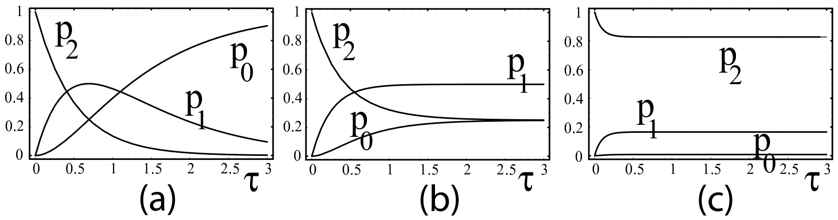

Figure 3.5: An analytical solution of the stochastic model based on a generating function is available for vanishing load and a reflecting boundary at $i = 0$, the completeley dissociated state. $p_i(\tau)$ is the probability that i bonds are closed at time τ $(0 \leq i \leq N_t)$. Here the state probabilities as given in Eq. (3.31) are plotted for two bonds and the initial condition $N_0 = N_t = 2$. (a) Rebinding rate $\gamma = 0$, (b) $\gamma = 1$, (c) $\gamma = 10$.

3.4 Two bonds under constant shared loading

Before addressing our stochastic model in the general case of N_t bonds, it is instructive to consider the case $N_t = 2$. The solution Eq. (3.31) derived from the generating function for the case $f = 0$ and a reflecting boundary now reads

$$p_2(\tau) = \frac{(e^{-(1+\gamma)\tau} + \gamma)^2}{(1+\gamma)^2} \ , \tag{3.37}$$

$$p_1(\tau) = \frac{2(e^{-(1+\gamma)\tau} + \gamma)(1 - e^{-(1+\gamma)\tau})}{(1+\gamma)^2} \ , \tag{3.38}$$

$$p_0(\tau) = \frac{(1 - e^{-(1+\gamma)\tau})^2}{(1+\gamma)^2} \ . \tag{3.39}$$

One readily checks that $\sum_i p_i = 1$ and $p_i(0) = \delta_{i2}$. In Fig. 3.5, we plot the p_i for $\gamma = 0, 1,$ and 10. Since now $N_{eq} = 2\gamma/(1+\gamma)$, the average number of closed bonds is close to 0 and 2 for weak and strong rebinding, respectively.

The probability for reaching the completely dissociated state is the probability for having one bond times the probability for this bond to rupture, that is $p_{1\to0}(\tau) = p_1(\tau)r(1) = p_1(\tau)$. For the case without rebinding, $\gamma = 0$, we have $p_{1\to0}(\tau) = 2(e^{-\tau} - e^{-2\tau})$. This result can also be obtained by a different route, namely through a recursive procedure which uses the fact that now cluster rupture corresponds to a well-defined sequence of events, 2 → 1 → 0, which are connected by two Poisson processes. For each Poisson process, the dissociation probability decays exponentially with time. We start with two bonds. Breakage of the first bond is a Poisson process with a rate which is doubled compared to the situation with one bond:

$$p_{2\to 1}(\tau) = 2e^{-2\tau}\ . \tag{3.40}$$

Breakage of the second bond is another Poisson process, this time with the single-bond rate, which however presupposes that a first bond has broken some time before:

$$p_{1\to 0}(\tau) = \int_0^\tau d\tau' p_{2\to 1}(\tau') e^{-(\tau-\tau')} = 2(e^{-\tau} - e^{-2\tau})\ . \tag{3.41}$$

Thus we obtained the same result as before. Note that $p_{1\to 0}(0) = 0$: in contrast to the case of single bond decay with $p_{1\to 0}(0) = 1$, there is no finite probability for the cluster to decay at the very beginning, because simultaneous decay of two bonds is a higher order process.

In contrast to the solution with the generating function, the recursive procedure can be generalized to the case $f > 0$. The basic idea here is that even in the case of finite force, we still deal with a well-defined sequence of two Poisson processes. We now have

$$p_{2\to 1}(\tau) = (2e^{f/2}) e^{-(2e^{f/2})\tau}\ , \tag{3.42}$$

$$p_{1\to 0}(\tau) = \int_0^\tau d\tau' p_{2\to 1}(\tau')(e^f) e^{-(e^f)(\tau-\tau')} = \frac{2e^f}{2-e^{f/2}}(e^{-e^f\tau} - e^{-2e^{f/2}\tau})\ . \tag{3.43}$$

Obviously the limit $f = 0$ gives the results given before. For the mean cluster lifetime, one gets

$$T = \int_0^\infty dt\ t\ p_{1\to 0}(\tau) = \frac{1}{2}\left(2e^{-f} + e^{-f/2}\right)\ . \tag{3.44}$$

The same result can be obtained more easily by noting that since we have a sequence of two independent Poisson processes, their lifetimes simply add up:

$$T = \sum_{i=1,2} \frac{1}{r_i} = \frac{1}{e^f} + \frac{1}{2e^{f/2}} = \frac{1}{2}\left(2e^{-f} + e^{-f/2}\right)\ . \tag{3.45}$$

For $f = 0$, cluster lifetime $T = 3/2$, thus it is not twice as large as single bond lifetime, but somehow reduced, because bonds decay in parallel. The recursive procedure can be generalized to arbitrary cluster sizes (see below), but not to the case of finite rebinding, because then one loses the property of having a well-defined sequence of Poisson processes.

In the case of finite rebinding, cluster lifetime is infinite for a reflecting boundary. For an absorbing boundary, cluster lifetime can be identified with the finite mean first passage time for reaching the state $i = 0$. Although a full stochastic solution cannot be found in this case, one can calculate cluster lifetime for arbitray values of f and γ. We note that starting from state 2, the system moves to state 1 with probability 1, after the mean time $1/r_2$. From there, it rebinds to state 2 with probability $w_R = g_1/(r_1 + g_1)$ or dissociates with probability $w_D = r_1/(r_1+g_1)$, after the mean time $1/(r_1+g_1)$. Thus after two steps the system has reached state 0 with probability w_D or returned to state 2 with probability w_R, with $w_D + w_R = 1$. In detail, the probabilities and mean times for both processes are

$$w_D = \frac{e^f}{e^f + \gamma}, \qquad t_D = \frac{1}{2e^{f/2}} + \frac{1}{e^f + \gamma}\ , \tag{3.46}$$

$$w_R = \frac{\gamma}{e^f + \gamma}, \qquad t_R = t_D\ . \tag{3.47}$$

$$\tag{3.48}$$

Different paths to dissociation only differ in the number of rebinding events i to state 2:

$$w_i = w_D w_R^i, \qquad t_i = t_D + i t_R\ . \tag{3.49}$$

We first check normalization:

$$\sum_{i=0}^{\infty} w_i = w_D \frac{1}{1 - w_R} = 1 \tag{3.50}$$

and then calculate cluster lifetime:

$$T = \sum_{i=0}^{\infty} t_i w_i = t_D + t_R w_D \sum_{i=0}^{\infty} i w_R^i \tag{3.51}$$

$$= t_D + t_R w_D \frac{w_R}{(1 - w_R)^2} = \frac{t_D}{1 - w_R} \tag{3.52}$$

$$= \frac{1}{2}\left(e^{-f/2} + 2e^{-f} + \gamma e^{-3f/2}\right)\ . \tag{3.53}$$

For $f = 0$, this simplifies to $T = (3+\gamma)/2$. For $\gamma = 0$, this simplifies to $T = (2e^{-f} + e^{-f/2})/2$, in agreement with the result found above from the recursive procedure. For both $f = 0$ and $\gamma = 0$, we have $T = 3/2$ as above.

3.5 Cluster under constant shared loading

We now turn to clusters of arbitrary size N_t under constant loading. We start with the deterministic equation. In general, it can be solved analytically only in the case $\gamma = 0$. Since there is no rebinding, N_t is not important. We have to solve

$$\frac{dN}{d\tau} = -Ne^{f/N} \ . \tag{3.54}$$

Changing to $z = 1/N$

$$-d\tau = -\frac{dz}{z}e^{-f/N} = -\frac{d(fz)}{(fz)}e^{-(fz)} = d(E(fz)) \tag{3.55}$$

where E is the exponential integral with $E(z)' = -e^{-z}/z$. Thus

$$\tau^* - \tau_0 = E(\frac{f}{N_0}) - E(\frac{f}{N^*}) \tag{3.56}$$

where $N_0 = N(\tau_0)$. With $\tau_0 = 0$ and $N^* = 0$, we find

$$T = E(f/N_0) \ . \tag{3.57}$$

This solution implies three different scaling regimes. For weak loading, $f < 1$, we deal with simple Poisson decay, $N = N_0 e^{-\tau}$, and

$$T = \ln N_0 \ . \tag{3.58}$$

For intermediate loading, $f > 1$ but with $f/N_0 < 1$, we can expand for small arguments:

$$T = E(f/N_0) \approx \ln \frac{N_0}{f} \ . \tag{3.59}$$

In this case, there are still f bonds left when exponential decay is over, then faster decay sets in. For strong loading, $f/N_0 > 1$, there is super-exponential decay right from the start. We expand for large arguments:

$$T = E(f/N_0) \approx \frac{e^{-f/N_0}}{1 + f/N_0} \ . \tag{3.60}$$

With increasing load, the scaling of T with N_0 becomes stronger, from logarithmic for weak loading to linear with strong loading. Note that for a single bond $T = e^{-f}$. For the cluster, an exponential dependence is obtained only for the case of strong loading.

Rebinding stabilizes the cluster. For a reflecting boundary and in the absence of force, lifetime is infinite. It has been shown by Bell that the cluster remains stable up to a critical force f_c [10]. For the following it is helpful to revisit the stability analysis by Bell. In equilibrium we have

$$N e^{f/N} = \gamma (N_t - N) \ . \tag{3.61}$$

There are two roots in $0 \leq N \leq N_t$, with the larger one corresponding to a stable equilibrium. Above a critical loading, no roots exist and the cluster becomes unstable. Exactly at critical loading, the two roots collapse and the slopes of the two terms become equal. This gives an additional equation to determine critical values of N and f:

$$e^{f/N}(1 - \frac{f}{N}) = -\gamma \ . \tag{3.62}$$

We now define a new quantity $\alpha = f/N - 1$ and rewrite the two equations:

$$N e^{\alpha+1} = \gamma (N_t - N), \quad \alpha e^{\alpha+1} = \gamma \ . \tag{3.63}$$

From the second equation, we can determine α:

$$\alpha = \mathrm{plog} \frac{\gamma}{\mathrm{e}} \tag{3.64}$$

where the product logarithm plog(a) is defined as the solution x of $x e^x = a$. When dividing the two equations, we get

$$N = \frac{\alpha}{1+\alpha} N_t \ . \tag{3.65}$$

Therefore the critical load is simply

$$f_c = N(1+\alpha) = \alpha N_t = N_t \mathrm{plog} \frac{\gamma}{\mathrm{e}} \ . \tag{3.66}$$

For small γ, we have

$$f_c \approx \frac{\gamma}{e} N_t \ . \tag{3.67}$$

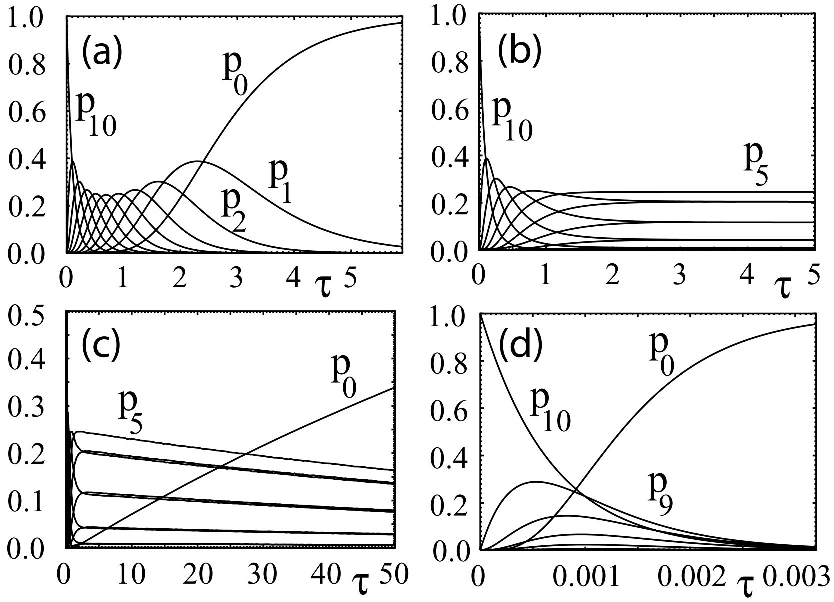

Figure 3.6: State probabilities p_i for $N_t = 10$. (a) $\gamma = 0$ and $f = 0$. (b) $\gamma = 1$ and $f = 0$ for a reflecting boundary at $i = 0$. (c) Same for absorbing boundary. (d) $\gamma = 0$ and $f = 50$. (a) and (b) follow from Eq. (3.31), (c) is obtained from Monte Carlo simulations, and (d) follows from Eq. (3.69).

For large γ, we have

$$f_c \approx 0.5 N_t \ln \gamma \ . \tag{3.68}$$

This result can be interpreted as follows: even for large γ (strong rebinding), the critical force per bond $F_c/N_t \approx F_b$, because the dependance on γ is only logarithmic. This means the simple force scale set by the potential well is sufficient to break the cluster even at strong rebinding. Note however that this is an equilibrium consideration: we did not specify the rupture time, which is expected to be a stronger function of γ. For small γ, the critical force goes to cero: for vanishing rebinding, no force is needed to break the cluster, which dissolves by itself.

We now turn to the stochastic model. For the case $f = 0$ and the reflecting boundary, it has been shown above that the Master equation can be solved exactly with the help of the generating function from Eq. (3.30), leading to the exact solution for the $p_i(\tau)$ given in Eq. (3.31). If rebinding vanishes,

$\gamma = 0$, we deal with *radioactive decay*, that is each bond decays independently of the others. Fig. 3.6a shows that in this case, a cluster with $N_t = 10$ bonds decays from $i = 10$ to 0 by visiting each of the intermediate states to an appreciable degree. In order to stabilize the cluster, one has to introduce rebinding. Then there is fast relaxation to a stable stationary state, as shown in Fig. 3.6b for $\gamma = 1$. For the biologically relevant case of an absorbing boundary at $i = 0$, a stable stationary state does not exist and the cluster will always dissociate on the long run. In this case, one has to solve the first passage problem of reaching the state $i = 0$ for the first time. This can be done semi-analytically by using Laplace transforms, where the last backtransform has to be done numerically. Alternatively, one can solve the Master equation numerically, as we always do in the general case, when both rebinding γ and force f are finite. Fig. 3.6c shows that in this case, the plateaus from Fig. 3.6b tilt downward, while p_0 increases steadily with time τ. Stability further decreases if force f is turned on. For very large force, rebinding (including the type of boundary at $i = 0$) becomes irrelevant, because the reverse rate r dominates the forward rate g. Then one has to deal with the case $\gamma = 0$, for which decay proceeds in a well-defined sequence of event. Then one can use a recursive scheme to construct p_i from p_{i-1}, as has been shown above for the case $N_t = 2$. In the general case, we find (with $N_0 = N_t$)

$$p_i(\tau) = \left(\prod_{j=i+1}^{N_t} r_j \right) \sum_{j=i}^{N_t} \left\{ \prod_{\substack{k=i \\ k \neq j}}^{N_t} \frac{e^{-r_j \tau}}{r_k - r_j} \right\} . \tag{3.69}$$

The probability for cluster dissociation at time τ is $p_1(\tau) r(1)$. Setting $i = 1$ in Eq. (3.69) and using Eq. (3.18), one obtains a formula which has been given before in Ref. [170]. Fig. 3.6d shows, for the case $f = 50$, that now the cluster decays very rapidly, with only few of the intermediate states being visited to an appreciable degree.

Once the set of state probabilities $p_i(\tau)$ is known, one can calculate any quantity of interest, in particular the mean number of closed bonds N as a function of time τ. We find that $N(\tau)$ usually decays exponentially. This is demonstrated in Fig. 3.7a for the case $f = 0$. The origin of the exponential decay can be understood as follows: first the system equilibrates into a binomial distribution peaked around $N_{eq} = \gamma N_t / (1 + \gamma)$ as described by the result for a reflecting boundary, that is Eq. (3.31). The lower tail of this distribution

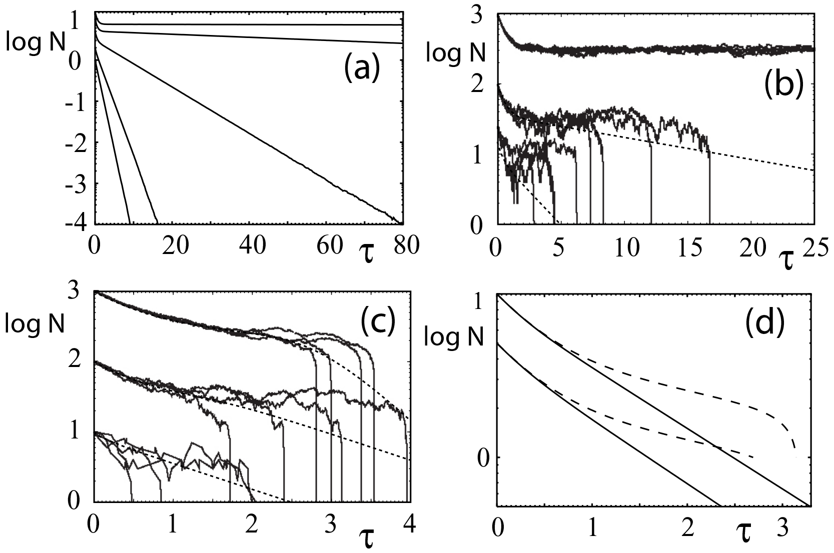

Figure 3.7: (a) Simulation results for the mean number of closed bonds N at time τ for $f = 0$, $\gamma = 1$ and $N_t = 1, 2, 5, 10$ and 15 (lower to upper lines). (b) Four typical simulation trajectories for each of the cases $N_t = 10, 100$ and 1000 for $\gamma = 1$ and $f/N_t = 0.25$. Dotted lines are $N(\tau)$. (c) Same for $f/N_t = 0.3$. (d) Comparision of stochastic (solid) and deterministic (dashed) results for $N(\tau)$ for $N_t = 5$ and 10 for $\gamma = 1$ and $f/N_t = 0.3$.

then 'leaks' into the state $i = 0$ due to the absorbing boundary. The smaller N_t or γ, the larger the tail contribution at $i = 1$ and the faster the systems loses realizations to the absorbing boundary. The resulting decay can be approximated by $N(\tau) \approx N_{eq} e^{-a\tau}$ with $a \approx p_1(\infty)$ from Eq. (3.31). For the values of N_t used in Fig. 3.7a, one finds $a \approx 4.6 \times 10^{-4}, 9.7 \times 10^{-3}, 0.16$ and 0.5 for $N_t = 2, 5, 10$ and 15. Numerically we find $a = 2.5 \times 10^{-4}, 8.5 \times 10^{-3}, 0.13$ and 0.6, thus the leakage estimate is rather good.

In order to assess the role of fluctuations, it is instructive to study single simulation trajectories. Since we use the Gillespie algorithm for exact stochastic simulations [61], they are expected to resemble experimental trajectories. Fig. 3.7b shows that for large cluster size and small force, typical trajectories fluctuate around a plateau value close to N_{eq}. However, for small cluster sizes, fluctuations to smaller bond numbers lead to fast loss of realizations to the absorbing boundary at $i = 0$. Final decay is rather abrupt due to force-accelerated rupture for increasingly smaller bond numbers. Fig. 3.7c shows that for sufficiently large force, also the large clusters decay quickly. The loss of stability for any cluster size follows from Bell's stability analysis of the deterministic equation Eq. (3.20) revisited above. For typical values of N_t and γ, f_c belongs to the intermediate force regime, $1 < f < N_t$. For $\gamma = 1$, we have $f_c/N_t = 0.278$. Fig. 3.7b and c are below and above the critical force, respectively. In contrast to Bell's continuum analysis, our stochastic analysis shows that for small clusters a small increase in loading can lead to the fast decay characteristic for the case without rebinding also for forces below f_c. Fig. 3.7d compares $N(\tau)$ as obtained from simulations to $N(\tau)$ as obtained from numerical integration of the deterministic equation Eq. (3.20). This shows that stochastic and deterministic results differ also on the level of the first moment.

The quantity of largest practical interest is cluster lifetime T as a function of the model parameters N_t, γ and f. In general, T can be calculated from the adjoint Master equation [172]. For $N_t = 2$ and 3, the solutions can also be found by directly summing with appropriate weights over all possible dissociation paths, each of which is a sequence of Poisson processes. This has been shown above for the case of two bonds, compare Eq. (3.51). For $N_t \geq 4$, the direct procedure becomes intractable. However, in the case of vanishing rebinding ($\gamma = 0$), there is only one dissociation path and the exact solution is simply

$$T = \sum_{i=1}^{N_t} \frac{1}{r_i} \tag{3.70}$$

for all values of N_t [170]. In the small force regime, $f < 1$, we have the case of radioactive decay and $T \approx H_{N_t} = \sum_{i=1}^{N_t} 1/i \approx \ln N_t + 1/(2N_t) + \Gamma$. Here H_{N_t} are the harmonic numbers and $\Gamma = 0.577$ is Euler's constant. In this regime, T depends only weakly (logarithmically) on N_t and large cluster sizes are required to achieve long lifetimes [66, 170]. In the intermediate force regime, $1 < f < N_t$, we find $T \approx H_{N_t} - H_f \approx \ln(N_t/f)$. Here the effective cluster size is reduced to N_t/f, because the cluster dissociates very rapidly for $i < f$. In the high force regime, $f > N_t$, only the term with $i = N_t$ contributes: if the first bond breaks, all remaining bonds break within no time. In Fig. 3.8a we plot T as a function of f/N_t for different cluster sizes N_t. At small forces, T plateaus at the value H_{N_t}, and at intermediate forces, it decays with a clear scaling with f/N_t.

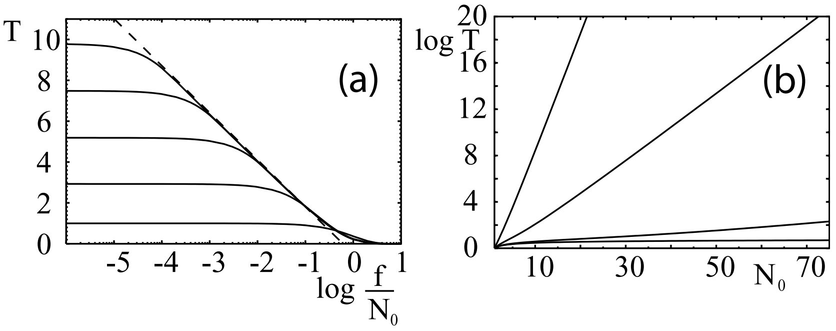

Figure 3.8: Analytical results for cluster lifetime T. (a) T as a function of f/N_t for $\gamma = 0$ and $N_t = 1, 10, 100, 1000$ and 10000 (lower to upper solid lines). The dotted curve is the approximation $T = \ln(0.61(N_t/f))$. (b) T as a function of cluster size N_t for $f = 0$ and $\gamma = 0.0, 0.1, 1.0$ and 10.0 (lower to upper lines).

The destabilizing effect of force can be counteracted by rebinding. In the case of vanishing force ($f = 0$), the exact solution can also be found by using Laplace transforms, because in order to obtain the mean first passage time based on the solution for the reflecting boundary, the backtransform does not have to be solved [64]. We find

$$T = \frac{1}{1+\gamma}\left(\sum_{n=1}^{N_t}\left\{\binom{N_t}{n}\frac{\gamma^n}{n}\right\} + H_{N_t}\right) . \tag{3.71}$$

For $\gamma = 0$, we recover the result $T = H_{N_t}$ from above. For $N_t = 2$, we get the result $T = (3 + \gamma)/2$ as above. In general, T scales $\sim \gamma^{N_t-1}$ with rebinding rate. In Fig. 3.8b we plot T as a function of N_t for different values of γ. For $\gamma < 1$, the logarithmic dependence of T on N_t is valid over a wide range of cluster size. However, for very large clusters, lifetime starts growing exponentially with N_t. For $\gamma > 1$, this strong increase of T with N_t is found for any value of N_t. Therefore increasing rebinding is much more effective than increasing cluster size in achieving cluster stability, and essential to ensure physiological cluster lifetimes with reasonable numbers of bonds. For example, in the absence of both force and rebinding and if the lifetime of each bond was 1 s ($k_0 = 1$ Hz), Eq. (3.71) predicts that the astronomical number of $\sim 10^{40000}$ independent bonds would be needed to achieve a cluster lifetime of one day ($T \sim 10^5$ s). In contrast, for $k_{on} = 1$ Hz ($\gamma = 1$), the same cluster lifetime T is achieved by $N_t = 20$. If rebinding is ten times slower than unbinding ($\gamma = 0.1$), cluster lifetime T is down to 7 s and one needs $N_t = 150$ bonds to regain a cluster lifetime of one day. In this way, knowing cluster lifetime and two out of the three parameters N_t, γ and f allows to estimate the unknown one.

3.6 Cluster under linear shared loading

We now turn to the case of linear loading, which is important for future experiments on adhesion clusters. Since now force increases in time without bounds, the cluster will always dissociate in the long run, both for absorbing and reflecting boundaries. The deterministic equation from Eq. (3.20) now reads

$$\frac{dN}{d\tau} = -Ne^{\mu\tau/N} + \gamma(N_t - N) \; . \tag{3.72}$$

It appears that this equation cannot be solved analytically even in the case $\gamma = 0$. It has been analyzed before by Seifert in the framework of a scaling approach [156]. For vanishing rebinding, the scaling analysis shows that like in the case of constant loading, decay can be divided into two parts. Initial decay is not yet affected by loading and thus is exponential with $N(\tau) = N_0 e^{-\tau}$. The second part of the decay is super-exponential and can be shown to be much shorter than the first part. Therefore the crossover time, which is defined by an implicit function, determines cluster lifetime T. In the regime of slow loading, $\mu < 1$, exponential decay persists until $N(\tau) = 1$ where cluster decay is complete and $T = \ln N_0$. In the regime of intermediate loading, $1 < \mu < N_t$, the crossover occurs before $N(\tau) = 1$ is reached, and lifetime is reduced to $T \sim \ln(N_0/\mu)$. In the regime of fast loading, $\mu > N_t$, lifetime scales even stronger with loading rate, $T \sim (N_0/\mu)\ln(\mu/N_0)$. In the case with rebinding, the scaling analysis is much more complicated. For intermediate loading, $1 < \mu < N_{eq}$, a power-law-like behaviour $T \sim (N_t/\mu)^{1/2}$ has been erroneously predicted in Ref. [156], as corrected in Ref. [157]. For fast loading, $\mu > N_t$, rebinding can be neglected and $T \sim (N_0/\mu)\ln(\mu/N_0)$ as above.

We first discuss the case of vanishing rebinding, $\gamma = 0$. In this case, the cluster can only decay and the total number of bonds N_t is not relevant, thus it is sufficient to specify N_0. In Fig. 3.9a we plot $N(\tau)$ as obtained from simulations of the Master equation (dashed lines) and from numerical

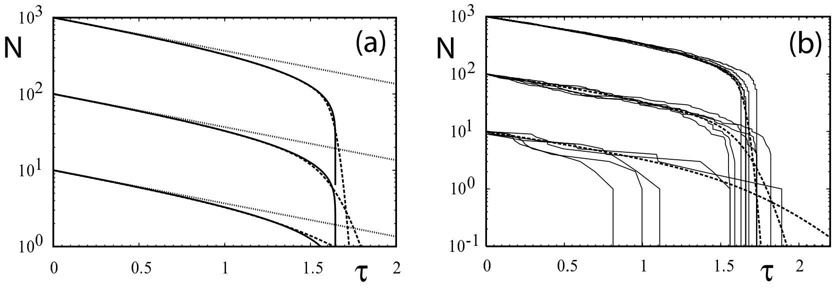

Figure 3.9: (a) Mean number of closed bonds N as a function of time τ for the case of vanishing rebinding, $\gamma = 0$, for $\mu/N_0 = 0.1$ and $N_0 = 10, 10^2$ and 10^3. Dotted lines: Initial exponential decay. Solid lines: numerical integration of deterministic rate equation for N. Dashed lines: first moment of the Monte Carlo simulation of the Master equation. (b) Individual trajectories from Monte Carlo simulations in comparison with the mean.

integration of the deterministic equation (solid lines) for $N_0 = 10, 10^2$ and 10^3. The dotted line is the exponential decay $N(\tau) = N_0 e^{-\tau}$ for vanishing loading. In the presence of loading, the later part of the decay process clearly is super-exponential. In detail, we find that the final stage of the rupture process is rather abrupt. This abrupt decay is typical for shared loading and has been found above also for shared constant loading. Interestingly, the first moment of the stochastic process decays less abrupt than the deterministic result. The reason is that at late stage, the stochastic treatment also includes the effect of clusters larger than in the deterministic equation, resulting in slower decay. In Fig. 3.9b, we show representative trajectories from Monte Carlo simulations, which show that fluctuations are most prominent for small clusters. For increasing cluster size, fluctuations become smaller and rupture events are concentrated around the rupture of the deterministic cluster. An analysis of the variance shows that for slow loading, it is close to the exact result for vanishing loading, $\langle i^2 \rangle - \langle i \rangle^2 = N_0 e^{-\tau}(1 - e^{-\tau})$ [122]. It vanishes for $\tau = 0$ due to the initial condition, then quickly rises to a maximum and finally decays exponentially. As loading rate μ increases, a large additional peak appears shortly before final rupture (not shown). This reflects the fact that fluctuations tend to change the timepoint of rupture, rather than the typical shape of the decay curve, as evidenced by Fig. 3.9b.

Cluster lifetime T is the mean time to reach the state $i = 0$. By defining

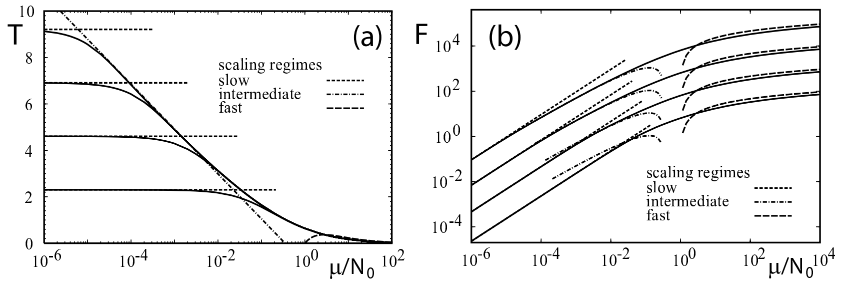

Figure 3.10: (a) Cluster lifetime T and (b) mean rupture force $F = \mu T$ for the case of vanishing rebinding, $\gamma = 0$, as a function of μ/N_0 for $N_0 = 10, 10^2$ and 10^3. Solid lines: numerical integration of deterministic equation (for $\gamma = 0$, stochastic results for T and F are rather similar). Dashed lines: curves for all three scaling regimes.

cluster dissociation rate $D = dp_0/d\tau = r_1 p_1$, cluster lifetime follows as $T = \int_0^\infty d\tau\ \tau D$. For $\mu < 1$, the simulation results are close to the analytical results for $\mu = 0$, $D(\tau) = N_0 e^{-\tau}(1 - e^{-\tau})^{N_0 - 1}$ [122] and $T = \sum_{i=1}^{N_0} 1/i \approx \ln N_0 + (1/2N_0) + 0.577$ [66, 170]. For large N_0, the deterministic scaling $T = \ln N_0$ results. For $\mu > 1$, the functions $D(\tau)$ become narrowly peaked around the mean value T. As suggested by the scaling analysis, we find that now T depends only on the value of μ/N_0. In Fig. 3.10a, we plot deterministic results for T as a function of μ/N_0 and for different values of N_0. The stochastic results are very similar, except for the differences in the initial plateau values. Initially, the different curves plateau at the values $\ln N_0$ for $\mu < 1$. For $1 < \mu < N_0$ and sufficiently large N_0, they collapse onto a universal curve, which can be approximated by $0.84 \ln(0.35 N_0/\mu)$. For $\mu > N_0$, they collapse onto another universal curve, $(N_0/\mu)\ln(\mu/N_0)$. In Fig. 3.10b, we plot the logarithm of the mean rupture force, $F = \mu T$, as a function of μ/N_0. For large N_0, one clearly sees the sequence of the three different scaling regimes. For decreasing N_0, the intermediate scaling curve becomes an increasingly bad fit.

We now turn to the case of finite rebinding. In the stochastic framework, cluster lifetime can be identified with the finite mean first passage time of reaching the absorbing boundary at $i = 0$. For vanishing loading, $\mu = 0$, an exact result T_{stoch} has been derived in Eq. (3.71). In the deterministic framework, Bell's stability analysis has shown that cluster stability is lost

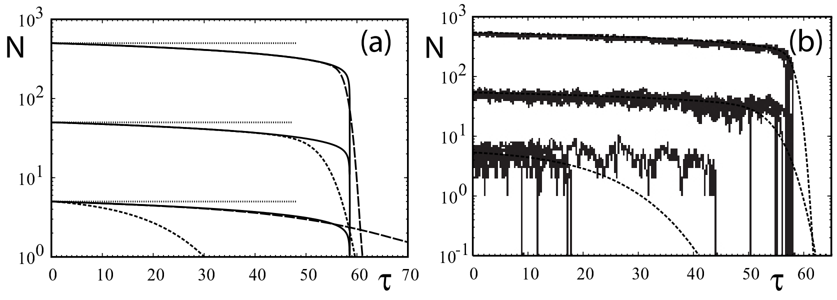

Figure 3.11: (a) Mean number of closed bonds N as a function of time τ for rebinding rate $\gamma = 1$ and loading rate $\mu/N_{eq} = 0.01$. Cluster sizes $N_t = 10$, 10^2 and 10^3, initial condition $N_0 = N_{eq} = \gamma N_t/(1+\gamma)$. Dotted lines: Initial number of closed bonds. Solid lines: numerical integration of deterministic equation. Short dashed lines: first moment of the Monte Carlo simulations. Long dashed line: reflecting boundary for $N_t = 10$. (b) Individual trajectories from Monte Carlo simulations in comparison with the mean.

beyond the critical force $f_c = N_t \text{plog}(\gamma/\text{e})$, compare Eq. (3.66) [10]. For slow loading, $\mu < 1$, the adhesion cluster will follow the quasi-steady state until the critical force f_c is reached at the time $\tau_c = f_c/\mu$. The remaining time to rupture is smaller and thus the lifetime of the adhesion cluster is close to

$$T_{det} = \frac{N_t}{\mu} \text{plog} \frac{\gamma}{\text{e}} \ . \tag{3.73}$$

It diverges with the inverse of loading rate in the limit of vanishing μ, as it is required by the existence of a stable steady state and a finite rupture force $F = \mu T = f_c$. In Fig. 3.11a $N(\tau)$ is plotted for $\gamma = 1$ as obtained from Monte Carlo simulations (short dashed lines) and from numerical integration of the deterministic equation (solid lines). The three different initial conditions N_0 for $N_t = 10, 10^2$ and 10^3 are represented by the dotted lines. In Fig. 3.11b individual trajectories from the simulations are compared to the stochastic averages from Fig. 3.11a. For the small cluster size $N_t = 10$, loading rate is so small that $f_c/\mu > T_{stoch}$. Then $T \approx T_{stoch}$ and the cluster decays by itself due to stochastic fluctuations to the absorbing boundary (*ultra-slow regime*). In this case, stochastic and deterministic results deviate strongly from each other. For the case of a reflecting boundary (long dashed line in Fig. 3.11a), stochastic and deterministic results agree rather well up the

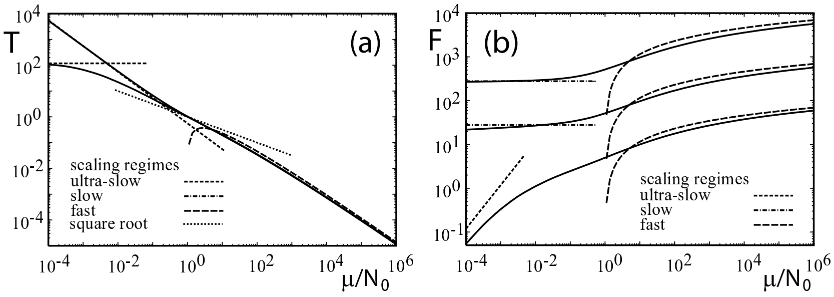

Figure 3.12: (a) Cluster lifetime T and (b) mean rupture force $F = \mu T$ for the case $\gamma = 1$ as a function of μ/N_0 for $N_0 = 10, 10^2$ and 10^3. In (a), the curves for the two larger clusters are nearly identical.

abrupt decay of the deterministic solution, but show considerable differences beyond this point. For the large clusters, $N_t = 10^2$ and 10^3, fluctuations are less probable until the force is close to f_c. Therefore the individual clusters fluctuate around the quasi-steady state and decay occurs only close to the deterministic cluster lifetime T_{det}. Due to the large force on a single bond at f_c, the absorbing boundary condition has little influence here. A detailed analysis of the variance confirms this description (not shown): for the smallest cluster, when fluctuations dominate during the whole time evolution, the variance shows a broad peak. For the larger clusters, it develops a narrow peak around the mean rupture time.

In Fig. 3.12, we show cluster lifetime T and the mean rupture force $F = \mu T$ for $\gamma = 1$ as a function of μ/N_0 for the cases $N_t = 10$, 10^2 and 10^3. For the smallest cluster, fluctuations to the absorbing boundary determine the lifetime at small loading rates, thus T starts at the value of T_{stoch} and ends in the scaling regime for fast loading, where the curves are practically identical for all different parameter values at a given value for μ/N_{eq}. The curves for the two larger clusters are nearly identical. They start at the values of T_{det} for small loading rates and end in the same fast loading regime that is found for the smallest cluster (at extremely small loading rates, they show the constant scaling with μ). An intermediate loading regime seems to exist only as a transient between the regimes of slow and fast loading. In particular, it does not fit well to an inverse square root dependence (dashed line in Fig. 3.12a).

In summary, for the case of vanishing rebinding, $\gamma = 0$, our full treatment nicely confirms the scaling analysis of the deterministic equation for cluster lifetime T as a function of μ and N_0 [156]. However, in contrast to the scaling analysis, the full treatment presented here allows for detailed comparision with experiments, e.g. in regard to typical unbinding trajectories or binding strength over a range of loading rates spanning different scaling regimes. For the case with finite rebinding, $\gamma > 0$, we identify a sequence of two new scaling laws within the regime of slow loading, $\mu < 1$. For ultra-slow loading, T is independent of μ and is determined by stochastic fluctuations towards the absorbing boundary. For larger μ (but still with $\mu < 1$), T starts to scale inversely with μ, due to the finite rupture strength at constant loading. In contrast to the case of vanishing rebinding, a scaling regime of intermediate loading, $1 < \mu < N_{eq}$, could not be identified.

3.7 Biological relevance

The case of linear loading is relevant mainly to future experiments on forced unbinding of adhesion clusters. Recently, dynamic force spectroscopy experiments have been reported for clusters of bonds between $\alpha_\nu\beta_3$-integrins on endothelial cells and RGD-lipopeptides on vesicles [138]. Since the vesicles act as soft transducers, shared loading over a contact ring is expected. For this experiment, parameter values can be estimated to be $N_t \approx 100$, $F_b \approx 40$ pN, $k_0 \approx 0.01$ Hz and $\gamma \approx 1$. Loading rates have been varied from $r = 20 - 4 \times 10^3$ pN/s, corresponding to $\mu/N_t = 0.5 - 100$, that is to the intermediate and fast loading regimes. We expect that future improvements in experimentation will make it possible to access also the slow loading regime, for which our work predicts interesting stochastic effects.

In physiological settings, force will never increase without bounds like in experiments with linear loading ramps. In particular, in cell-matrix and cell-cell adhesion, cluster lifetime is usually much larger than the time scale for changes in loading. Then the case of constant loading can be assumed to be a good approximation. However, the modeling presented above for constant loading does certainly not hold for cell-matrix adhesions, for which we have shown in chapter 2 that they grow rather than decay under force. At the current stage, additional experimental evidence would be very helpful to proceed with modeling the mechanosensor at focal adhesions. However, one intriguing possibility is that force at focal adhesions leads to mechanical opening-up of domains in certain focal adhesion proteins like vinculin [6, 59, 16]. This then might result in certain signaling events leading to recruitment of additional bonds (instead of loss of bonds like in the physical case without signaling). In this context, the model presented in this chapter suggests that the stress constant ~ 5.5 nN/μm^2 found in chapter 2 might be close to the critical force $f_c = N_0$ plog(γ/e), because then small changes in cytoskeletal loading would result in strongly accelerated cluster decay, possibly leading to mechanical opening-up of signaling domains. Recent single molecule experiments for activated $\alpha_5\beta_1$-integrin binding to fibronectin gave $k_0 = 0.012$ Hz and $F_b = 9$ pN [106]. Setting $F_c = 5.5$ nN and using $N_0 = 10^4$, we predict $\gamma = 0.2$, corresponding to a rebinding rate $k_{on} = 0.002$ Hz. Estimates like this are useful, because if they could be validated in an independent experiment, it would give support to the notion that focal adhesions (or parts of them) are regulated to be close to critical thresholds, a property which is known from certain signaling pathways. However, it should also be pointed out that other mechanisms might account for the mechanosensor at focal adhesions, including large-scale rearrangements of the submembrane plaque or changes in transport rates in and out of the plaque effected by force.

Our model for constant loading is expected to apply to situations in cell adhesion in which no reenforcement processes counteract the destabilizing effect of force. Recently, we have argued that this might be the case for tethering and rolling of leukocytes on blood vessel walls [44, 149]. As explained in the introduction, leukocytes roll on the endothelium in order to survey it for signs of inflammation. Initial capture is provided mainly by L-selectin. A physiological ligand density, tethering through L-selectin leads to deceleration, but not to complete stop, because the later part of the extravasation cascade is determined by more specific signals. Therefore, L-selectin tethers are meant to break quickly, in marked contrast to focal adhesions. There are two properties of L-selectin tethers which ensure this requirement: short bond lifetimes and small cluster sizes due to low ligand density. Since the pioneering experiments on L-selectin rolling in flow chambers, it has been widely believed that L-selectin tethers are based on single molecule binding events [5, 4]. The main piece of evidence for this interpretation has been that L-selectin tether kinetics in flow chambers shows first-order dissociation kinetics with a dissociation rate which depends exponentially on shear force, as predicted by the Bell equation. One remaining puzzle in this field however has been the explanation for the shear threshold, that is the observation that appreciable tethering through L-selectin and subsequent rolling only occurs above a threshold in shear [53], even in cell-free systems [3, 67].

Several explanations have been suggested for the shear threshold. Chang and Hammer suggested that faster transport through increased shear flow leads to increased probability for receptor ligand encounter [27]. However, new high resolution data from the Alon lab (video camera resolution 2 ms) now indicate that below the shear threshold, the issue is insufficient stabilization rather than insufficient ligand recognition [44]. Earlier work has used a time resolution of 30 ms and therefore has missed the formation of short-lived tethers below the shear threshold [5, 4]. Chen and Springer suggested that increased shear helps to overcome a repulsive barrier, possibly resulting from negative charges on the mucin-like L-selectin ligands [30]. However, the Alon lab showed that small oligopeptide ligands for L-selectin presented on non-mucin avidin scaffolds exhibit the same shear dependence as their mucin counterparts [44]. Evans and coworkers have argued that increased shear leads to cell flattening and formation of additional bonds [50]. However, the Alon lab found that fixation of PSGL-1 presenting neutrophils does not change the properties of tethers formed on low density immobilized L-selectin, thus cell deformation as well as stretching and bending of microvilli do not play any significant role in L-selectin tether stabilization. Recently, the unusual molecular property of catch bonding has been suggested as explanation for the shear threshold [121]. However, the data by the Alon lab suggest that force-related processes do not account for the shear threshold of L-selectin mediated tethering [44].

In Fig. 3.13a, we plot the recent data from the Alon lab which suggests a new explanation for the shear threshold [44]. The main idea here is that by adding 6 percent of the non-toxic sugar Ficoll, viscosity and thus shear stress (but not shear rate) is increased by a factor of 2.6. Below the shear threshold at shear rate $\dot{\gamma} = 40$ Hz, the high resolution data show tethering events which have been missed earlier, since with 250 Hz the dissociation rate below the shear threshold is unusually large. Fig. 3.13a shows that it is independent of the viscosity of the medium. At the shear threshold, we find a 14-fold reduction in dissociation rate. In the case of added Ficoll, a similar stabilization takes place at the same value of shear rate (although dissociation at the shear threshold is now increased 3-fold compared to the case without Ficoll, roughly as expected from the Bell equation). The fact that there is no shift of the shear threshold on addition of Ficoll indicates that stabilization at the shear threshold results from shear-mediated transport, rather than from a force-dependent process. Transport might result in the formation of multiple bonds, most likely of two bonds distributed over two microvilli.

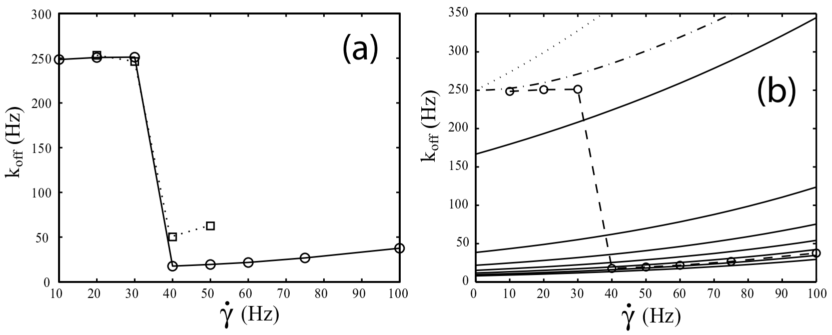

Figure 3.13: (a) Tether dissociation rate k_{off} determined from kinetic analysis of flow chamber experiments plotted as function of shear rate $\dot{\gamma}$. Solid line with circles versus dotted line with squares: without versus with Ficoll. (b) Theoretical predictions compared to the experimental data without Ficoll from (a). Dotted line: single bond dissociation rate with instantaneous loading. Dash-dotted line: effect of finite loading rate. Solid lines from top to bottom: cluster dissociation rate for two-bonded tether with increasing values of rebinding rate.

However, as we have argued above, simple increase in bond number has only a weak effect on cluster lifetime. In particular, the lifetime of two independently decaying bonds is increased only by a factor of 1.5 compared to a single bond. Eq. (3.70) predicts that without rebinding, the astronomical number of 6×10^5 bonds was needed to achieve the 14-fold stabilization found experimentally. For the case of diluted ligand studied here, this is clearly unrealistic. The modeling presented above therefore suggests that fast rebinding made possible by the presence of multiple bonds leads to the dramatic stabilization at the shear threshold.

In Fig. 3.13b, we present our detailed modeling for the experimental data in Fig. 3.13a [149]. The dotted line is the single bond dissociation rate as given by the Bell equation, with the assumption of a force-free dissociation rate $k_0 = 250$ Hz and instantaneous loading. As suggested in earlier work, here we use an internal force scale $F_b = 200$ pN and force $F = 180$ pN per dyn/cm^2 of shear stress [5, 4]. In order to explain the plateau in dissociation rate observed below the shear threshold, we take into account the effect of finite loading rate. Modeling the loading protocol as a ramp of force with initial loading rate r, which plateaus at the constant force F after deceleration time t_s (compare Eq. (3.16)), we obtain the dash-dotted line, which is in much better agreement with the experimental results. Here the detailed values follow from the laws of Stokes flow [65]. Right at the shear threshold, $r = 10^4$ pN/s, $F = 72$ pN and $t_s = 8$ ms. The main issue here is that with $r = 10^4$ pN/s, we are below the critical loading rate $r_c = k_0 F_b = 5 \times 10^4$ pN/s, thus the bond essentially decays by itself before it starts to appreciably feel the effect of force. Dissociation above the shear threshold is modeled as dissociation of a cluster with two bonds. Because now tether dissociation rate is much larger than initial loading rate, force can be assumed to be constant and we can use Eq. (3.53). The solid lines from top to bottom show the resulting cluster dissociation rate with rebinding rate $k_{on} = 0, 10, 20, 40$ and 60 k_0. The two-bonded tether with $k_{on} \approx 10^4$ Hz agrees well with the experimentally measured data. In fact this estimate is supported by other estimates using tethering behaviour observed for certain L-selectin mutants and affinity experiments in solution [149]. A detailed analysis also shows that small clusters with fast rebinding show the same characteristics in the dissociation behaviour as observed in flow chamber experiments for L-selectin tethering above the shear threshold, namely effectively first order dissociation with exponential dependance on shear rate [149]. Although the new interpretation for the shear threshold has to be checked carefully in future experiments, our modeling shows that theoretical estimates indeed can help to narrow down the list of possible mechanisms at play in complex cellular systems.

Chapter 4

Elastic interactions of cells with soft materials

4.1 Introduction

Anchorage-dependent cells like fibroblasts in connective tissue show a remarkable degree of mechanical activity. As explained in detail in chapter 2, cellular forces can be measured with elastic substrates. Using micropatterned elastic substrates, we found that fibroblasts typically exert forces of 10 nN at mature focal adhesions [6, 151]. Using a bed of flexible microneedles, similar values were found for smooth muscle cells [169]. Since adherent cells can have up to hundreds of focal adhesions, the overall force exerted by the cell can amount to μN. The forces exerted by cells on their environment result from non-equilibrium processes inside the cell and are generated by myosin II molecular motors interacting with the actin cytoskeleton. Since typical forces produced by molecular motors are in the pN-range [83], there must be up to 10^6 myosin II molecular motors contributing to overall cell traction.

When Harris and coworkers first observed the strong mechanical activity of cells on elastic substrates [76, 75], they concluded that they are required for the physiological function of the specific cell type under consideration. For example, fibroblasts are believed to maintain the integrity of connective tissue by mechanically pulling on the collagen fibers. Moreover, they are an integral part of the wound contraction process. Harris and coworkers also noticed that cells react to mechanical changes in their environment caused by traction of other cells. Since cells are known to align along topographic features in their environment (*contact guidance*), they suggested that cells react to traction-induced reorganization of collagen fibers. This mechanism amounts to a mechanical interaction of cells and has been addressed theoretically in coupled transport equations for fiber and cell degrees of freedom [132, 7].

During recent years, the sophisticated use of elastic substrates has shown that cells also react to purely elastic features in their environment, including rigidity, rigidity gradients and prestrain [135, 116, 179]. It is now generally accepted that these effects are related to the special properties of focal adhesions [59]. In particular, it has been shown that application of external force leads to growth of focal adhesions and therefore to strong signaling activity [175, 35, 144]. The same aggregation has been found for mature focal adhesions under internally generated force [6, 151, 169], suggesting that focal adhesions act as mechanosensors that convert force into biochemistry and vice versa. Therefore the mechanical activity of cells is not only related to the physiological function of their cell type, but is also a general way to collect information about the mechanical properties of the environment (*active mechanosensing*). There is strong evidence that this mechanism is involved in many important physiological situations, including tissue maintenance, wound healing, angiogenesis, development and metastasis [34, 56, 84].

The dynamics of focal adhesions is a subject of much current research [60]. Anchorage-dependent cells constantly assemble and disassemble focal adhesions, thereby probing the mechanical properties of their environment. Initial focal adhesions (*focal complexes*) are local processes based on integrin clustering. If initial clustering is stabilized by the properties of the extracellular environment, focal complexes can mature into focal adhesions. In this case, they connect to the actin cytoskeleton and a contractile force pattern builds up, that is actively generated by myosin II molecular motors interacting with the actin cytoskeleton. The minimal configuration of this machinery is a set of two focal adhesions connected by one bundle of actin filaments (*stress fiber*), that leads to a pinch-like force pattern, see Fig. 1.4. In condensed matter physics, such an object is known as an *anisotropic force contraction dipole* [161]. The concept of force dipoles has been applied before mainly for the description of point defects in traditional condensed matter systems, including hydrogen in metal (e.g. platinum) [173], atoms adsorbed onto crystal faces (e.g. argon on gold) [100], or intercalation compounds (e.g. lithium in graphite) [147]. The concept of force dipoles has also been used to model active biological particles in a fluid environment, e.g. ion pumps [141]

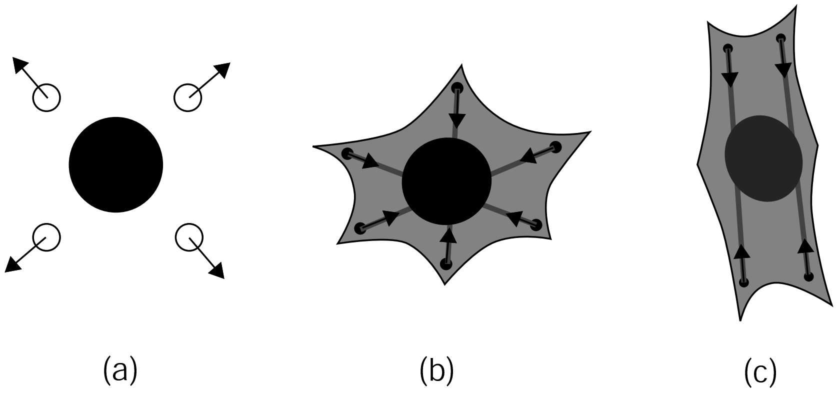

Figure 4.1: Schematic representation of physical and cellular force dipoles. (a) Physical case: an intercalated defect deforms the simple cubic host lattice, thus acting as an isotropic force expansion dipole. (b) Cellular case: anchorage-dependent cells probe the mechanical properties of the soft environment through their contractile machinery. Actin stress fibers (lines) are contracted by myosin II molecular motors and are connected to the environment through focal adhesions (dots). Even if cell morphology is round or stellate, different stress fibers probe different directions of space and compete with each other for stabilization of the corresponding focal adhesions. Therefore the probing process can be modeled as anisotropic force contraction dipole. (c) Cell morphology becomes elongated in response to anisotropic external stimuli, during locomotion or spontaneously during times of strong mechanical activity. Then most stress fibers run in parallel and the whole cell appears as an anisotropic force contraction dipole.

and rotary motors [105] embedded in fluid membranes, or self-propelled particles like swimming bacteria [162]. In chapter 2, we have used this concept to analyze the assumption of localized force and the use of finite film thickness in our work on elastic substrates. Recently, we have suggested to use the concept of force dipoles also to model the mechanical activity of cells [153]. Cells in an isotropic environment often show isotropic (that is round or stellate) morphologies. However, since the focal adhesion dynamics is local, even in this case there is an anisotropic probing process, that can be modeled by anisotropic force contraction dipoles. As we will argue below, only an anisotropic probing process can react to anisotropies in the environment. The anisotropy of focal adhesion dynamics becomes apparent when stress fibers start to orient in one preferential direction, either spontaneously during a period of large mechanical activity, or as a response to some external anisotropy, or during cell locomotion. In this case, cellular dipoles have been measured to be of the order of $P \approx -10^{-11} J$ (this corresponds to two forces of 200 nN each, separated by a distance of 60 μm) [151, 25]. In Fig. 4.1 we show schematic representations of the physical and cellular cases discussed here.

In order to sense the mechanical properties of their environment, cells can make use of the fact that these properties modulate the build-up of their own force patterns. In this chapter, we focus on the role of stress and strain in the extracellular material for cellular decision making in regard to positioning and orienting in a soft environment. In order to calculate how stress and strain are propagated in the environment, the extracellular material is modeled using isotropic linear elasticity. This is certainly true for synthetic elastic substrates (usually made from polydimethylsiloxane or polyacrylamide). The typical physiological environment for anchorage-dependent cells are hydrogels, whose mechanical properties are more difficult to model, in particular due to their viscoelastic and non-linear behaviour. Yet our calculations will show that our model has large predictive power also for this case, possibly because elastic deformations of hydrogels become encoded in plastic changes that later can be detected by active mechanosensing in a similar way as persistent elastic deformations. Given the assumption of isotropic linear elasticity, we can calculate how stress and strain follows from the force dipoles by solving the elastic equations for the geometry and boundary conditions of interest.

The most critical part of our modeling is the way in which physical or cellular force dipoles react to stress and strain in their environment. This subject has been treated extensively for the case of atomic defects in traditional condensed matter systems [173, 100, 147]. Here defects are usually modeled as isotropic force expansion dipoles. The equilibrium configuration follows by minimizing the sum of the elastic energy of the strained medium and the direct interaction energy between force dipole and elastic environment. The first term represents a restoring force and raises the energy (i.e. its sign is always positive), while the second term is a driving force that reduces the total energy (i.e. its contribution will always be negative). The equilibrium configuration will correspond to the minimum of the total energy as a function of position and orientation of the force dipoles, which results in an effective, so-called *elastic interaction* between the force dipole and other dipoles, sample boundaries or external strain fields. One central result of these studies is that the direct interaction between isotropic force dipoles in an isotropic elastic material vanishes [161] and that they interact through a boundary-induced (*image*) interaction that varies on the length scale of the sample size (leading to *macroscopic modes*) [173]. For anisotropic force dipoles, the direct elastic interaction does not vanish.

In contrast to this physical case, the effective behavior of active cells usually follows from dynamic and tightly regulated non-equilibrium processes inside the cell. In this chapter, we will show that despite this severe complication, it is still possible to describe the active response of mechanosensing cells in an elastic material in the same framework as the physical case [18, 17]. In particular, we consider interactions with external strain fields, sample boundaries or other physical force dipoles/cells. Although there are marked conceptual differences between the physical and cellular cases, they both require to solve the elastic boundary value problem to predict the resulting structure formation. Since cells are modeled as *anisotropic* force dipoles, these calculations are in general more involved than similar calculations for isotropic force dipoles. Our model can consistently explain a large body of experimental evidence for the behaviour of fibroblasts both on elastic substrates and in collagen gels. Our theory not only contributes to a better understanding of physiological processes involving mechanical activity of cells (including tissue maintenance, wound healing, angiogenesis, development and metastasis), in the future it also might be used to predict cell behaviour in artificial tissues, close to implants and on compliant biosensors.

4.2 Modeling

4.2.1 Force multipoles

In the following, we model a mechanically active cell as a localized force distribution in an elastic medium. In order to describe its mechanical action, we use the concept of a force multipolar expansion, which has been applied before for the description of point defects in condensed matter systems [173, 100, 147]. Force multipoles have been defined in chapter 2, compare Eq. (2.6). For both the cellular and physical situation we are interested in, we can assume local forces. For point-like defects, one can moreover assume that the overall force vanishes, because due to Newton's Third Law, the forces exerted by the defect on the elastic medium and by the elastic medium on the defect have to balance each other (the same argument applies to point defects in a fluid medium [141, 105, 162]). For cells, the situation is more complicated, because they are at the same time in contact with the elastic matrix and an aqueous medium, thus unbalanced forces might appear in the elastic matrix, which are balanced by viscous forces in the aqueous medium. However, viscous processes in the fluid medium decay very rapidly on the timescale of cell movement. Therefore unbalanced forces might occur for short periods of time, e.g. during back retraction of locomoting cell, but during most of the time, cells can be expected to be in mechanical equilibrium, as suggested by experiments measuring force patterns of both stationary and locomoting cells on elastic substrates [42, 151]. Our model for cellular force patterns can be interpreted as one stress fiber connecting two focal adhesions. Obviously this minimal system obeys mechanical equilibrium. Then overall force vanishes and the force dipole is the first relevant term in the multipolar expansion Eq. (2.6).

Force dipoles are classified according to their symmetry properties into isotropic dipoles (centers of contraction or dilation), anisotropic dipoles without moment and anisotropic force dipoles with moment [118]. Force dilatation and force contraction dipoles have only positive and only negative eigenvalues, respectively. For example, in three dimensions three pairs of juxtaposed forces, one for each coordinate direction, form an isotropic force dipole, where $P_{ij} = P\delta_{ij}$. Such a force dipole describes a spherical inclusion in a simple cubic lattice, see Fig. 4.1a [173]. Applied to two dimensions, it describes atomic defects adsorbed onto a substrate [100]. An anisotropic force dipole without moment is a non-diagonal, but symmetric tensor. For example, for a couple of juxtraposed forces with a dipole strength P and an orientation in direction $\vec{l}$, we can write the force dipole tensor as $P_{ij} = P\hat{l}_i\hat{l}_j$. Such dipoles are used below to describe the probing force patterns of cells, see Fig. 4.1b and c [153]. An anisotropic force dipole without moment oriented in the z-direction reads $P_{ij} = P\delta_{iz}\delta_{jz}$ and describes for example an atomic defect intercalated in graphite [147]. Finally, an anisotropic force dipole with an angular moment describes a set of two opposing forces $\vec{F}$ separated by a distance $\vec{l}$ oriented arbitrarily with respect to $\vec{F}$, which leads to $P_{ij} \neq P_{ji}$. In this paper, we only consider force dipoles without such moments.

4.2.2 Elastic interactions for physical dipoles

The elastic medium surrounding a particle can mediate an *elastic* interaction with other particles, sample boundaries or external strain fields. It is important to note that this effect requires a *direct* interaction of the particle with its elastic environment. In traditional condensed matter systems, the direct interaction is usually a quantum effect (e.g. Born repulsion for defects intercalated into a crystal lattice or van der Waals attraction for defects adsorbed onto a crystal lattice). The interaction of a single particle localized at $\vec{r}$ with the elastic medium can be described by an interaction potential $V_d(\vec{r}, \vec{u})$, which not only depends on position $\vec{r}$, but which also is a functional of the displacement field $\vec{u}(\vec{r'})$ of the elastic medium. For a fixed particle position $\vec{r}$, we can expand the interaction potential with respect to the displacement field:

$$V_d(\vec{r}, \vec{u}) \approx -\int f_i(\vec{r}+\vec{s}) u_i(\vec{r}+\vec{s})\ d^3 s\ , \tag{4.1}$$

where $f_i = -\delta V_d / \delta u_i|_{u_i=0}$ is the force density exerted by the defect onto the elastic medium in its undeformed reference state. Here and in the following, summation over repeated indices is always implied. The expansion can be terminated after the linear term because we assume small deformations, or, equivalently, small forces. This linearized interaction potential is widely used in the literature on elastic defects in traditional condensed matter materials [173, 100, 147]. For later use, we also note that Eq. (4.1) can be rewritten in terms of the force multipoles defined in Eq. (2.6), if one makes the assumption that the interaction of the defect with the medium is short-ranged. Then

$$V_d(\vec{r}, \vec{u}) \approx -\sum_{n=0}^{\infty} \frac{1}{n!} P_{i_1 \dots i_n i} u_{i, i_1 \dots i_n}(\vec{r})\ , \tag{4.2}$$

where indices after the comma denote derivatives of the displacement field with respect to position ($u_{,i} = \partial u / \partial r_i$). In this way, all the details of the direct interaction between medium and defect are subsumed in the defect force pattern and one can study elastic effects in different materials within a common theoretical framework, as long as the two assumptions of small and localized forces are valid.

The displacements of the elastic medium are controlled by a competition between the direct interaction between defect and medium and the elastic strain energy of the medium under the constraints of adequate boundary conditions. The strain energy is [99]

$$V_e = \frac{1}{2} \int d^3 r\ C_{ijkl} u_{ij}(\vec{r}) u_{kl}(\vec{r}) \tag{4.3}$$

where $u_{ij}(\vec{r})$ is the strain tensor and C_{ijkl} the elastic constant tensor of the medium. Consider now the general case of an elastic medium subject to loading with defects with an overall volume force density $\vec{f}(\{\vec{r^\alpha}\},\vec{r}) = \sum_\alpha \vec{f}^\alpha(\vec{r})$, where α numbers the different defects. Then the total energy of the system is

$$V_t = \frac{1}{2}\int d^3r\ C_{ijkl}u_{ij}(\vec{r})u_{kl}(\vec{r}) - \int d^3r\ f_i(\{\vec{r^\alpha}\},\vec{r})u_i(\vec{r}) - \oint dS\ f_i^s(\vec{r})u_i(\vec{r}) \tag{4.4}$$

where the first term is the strain energy V_e and the second term the direct interaction $V_d = \sum_\alpha V_d(\vec{r^\alpha})$. The surface force density $\vec{f^s}$ in the third term acts as a Lagrange multiplier that enforces the boundary conditions at the sample surface S. For a fixed defect configuration, the displacements $\vec{u}(\vec{r})$ are determined from $\delta V_t/\delta\vec{u} = 0$, which defines mechanical equilibrium:

$$C_{ijkl}u_{kl,j}(\vec{r}) = -f_i(\{\vec{r^\alpha}\},\vec{r}) \qquad \vec{r} \text{ in } V, \tag{4.5}$$

and the boundary condition at the surface of the elastic material:

$$C_{ijkl}u_{kl}(\vec{r})n_j(\vec{r}) = f_i^s(\vec{r}) \qquad \vec{r} \text{ on } S, \tag{4.6}$$

where $\vec{n}$ is the outward directed surface normal of the surface element dS. By combining Eq. (4.5) and Eq. (4.3), one finds $V_e = \frac{1}{2}\int d^3r\ f_iu_i = -\frac{1}{2}V_d$. Therefore the overall energy $V_t = V_d + V_e = \frac{1}{2}V_d = -V_e$ and the overall energy can be written as function of the defect configuration only. In this way, the *direct* interactions of the particles with the medium can be rigorously transformed into an *indirect* interaction between defects. This also allows the calculation of the interaction of a single defect with a boundary induced strain field or an external strain field applied at the boundary. The groundstate configuration of elastically interacting defects is obtained by minimizing total energy V_t.

4.2.3 Elastic interactions for active cells

The forces exerted by mechanically active cells on the environment are mainly due to actomyosin contractility. Thus, in contrast to the interaction of physical force dipoles with the elastic medium, where the force can be derived from conventional interaction potentials, cellular forces are continuously and actively generated by the cell and involve non-equilibrium processes, that

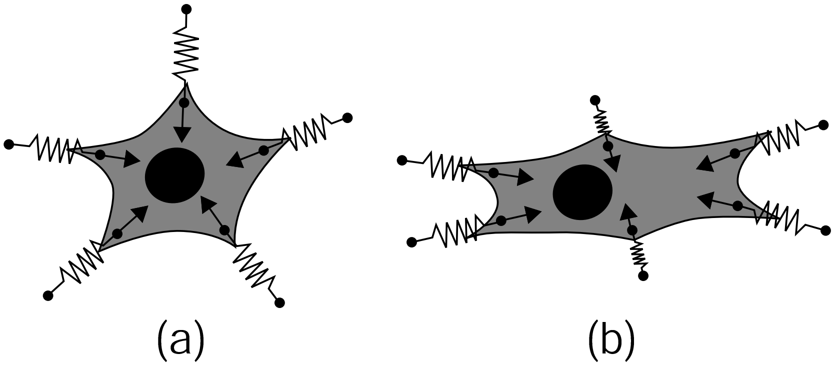

Figure 4.2: An adherent cell actively pulls on its soft environment through cell-matrix contacts. Experimentally, one finds that cells orient themselves in the direction of maximal stiffness of the environment. With this cartoon, we present one possible mechanism by which active mechanosensing in an elastically anisotropic medium might lead to cell orientation. The local elastic environment is represented by linear springs with different spring constants K, as indicated by differently sized springs. For upregulation of a contact, the cell has to invest the work $F^2/2K$. Therefore, upregulation is more efficient for larger K. (a) In an isotropic environment, all spring constants are the same, growth at different contacts is similar and the cell does not orient. (b) If spring constants are largest in one specific direction, the corresponding contacts outgrow the others and the cell orients in the direction of maximal stiffness of the environment.

are tightly regulated by biochemical events inside the cell. Hence, the interactions of cells with an elastic environment are more complicated than for physical defects and there is little a priori reason why they should be described by Eq. (4.1). Motivated by recent experiments with elastic substrates [135, 116, 179], we will now argue that despite these complications, a similar description as for the physical case can be employed for the cellular one [18, 17]. We ask which kind of information a cell can extract from its elastic environment using its contractile machinery. An appropriate scalar quantity to characterize the environment is the work the cell has to perform in order to build up a certain level of force against the elastic environment. Experimental observations suggest that active cell behaviour amounts to a simple preference for large effective stiffness, which corresponds to a minimization of this energy. As a simple analogue, consider a linear spring. In order to build up a certain force F, the energy $W = Kx^2/2 = F^2/2K$ has to be invested into the spring, where x is displacement and $F = Kx$ is force at equilibrium. If there is a choice of different springs with different spring constants K, the smallest amount of energy W to build up F has to be invested into the spring with the largest value for K. In the case of cells, the different springs correspond to different directions as probed by different stress fibers, and on the long run, the cell will orient in that direction that corresponds to the largest value of K, possibly because in this direction, the build-up of force is most efficient. The example of the linear spring can also be used to illustrate the main difference to the physical case, when the final configuration is determined by the overall energy $V_t = Kx^2/2 - Fx = -F^2/2K = -W$. Thus in contrast to the case of cellular force dipoles, for physical dipoles minimal values of stiffness K are most favorable. Our suggestion is presented in Fig. 4.2 as a cartoon.

We now explain our reasoning in more detail for the case of cells in a three-dimensional environment described by continuum elasticity theory. In order to identify a suitable analogue to the spring constant K, we introduce the concept of *local effective stiffness* of the elastic environment. We define this quantity to be the work W required to build up a unit force in the elastic medium. The deformation work W required to build up an arbitrary force distribution $\vec{f}(\vec{r})$ is given by:

$$W = \int d^3r \int_0^{u_{ij}^{\vec{f}}} C_{ijkl} u_{kl}(\vec{r}) du_{ij}(\vec{r}), \tag{4.7}$$

which in the absence of external prestrain is equivalent to the energy stored in the elastic medium given in Eq. (4.3). Then integration by parts gives

$$W = -\frac{1}{2} \int d^3r \; u_i(\vec{r}) C_{ijkl} u_{kl,j}(\vec{r}) + \frac{1}{2} \oint dS \; n_j C_{ijkl} u_{kl}(\vec{r}) u_i(\vec{r}) \; . \tag{4.8}$$

Applying the mechanical equilibrium conditions of the elastic medium, Eqs. -(4.5,4.6), yields

$$W = \frac{1}{2} \int d^3r \; u_i(\vec{r}) f_i(\vec{r}) + \frac{1}{2} \oint dS \; u_i(\vec{r}) f_i^s(\vec{r}) \; . \tag{4.9}$$

In an infinite medium the boundary condition at the surface yields a vanishing surface integral. Hence for a force distribution centered around $\vec{r}$, the volume integral can be turned into a local expression by using the definitions of

Eq. (2.6):

$$W^{\infty} = \frac{1}{2}\int f_i(\vec{r}+\vec{s})\ u_i(\vec{r}+\vec{s})\ d^3s = \frac{1}{2}\sum_{n=0}^{\infty}\frac{1}{n!}P_{i_1\ldots i_n i}u_{i,i_1\ldots i_n}(\vec{r}). \qquad (4.10)$$

In particular, for a force monopole and a force dipole one finds $W^{\infty} = \frac{1}{2}P_i u_i^{\infty}(\vec{r})$ and $W^{\infty} = \frac{1}{2}P_{ij}u_{ij}^{\infty}(\vec{r})$, respectively, where $\vec{u}^{\infty}$ and u_{ij}^{∞} are the displacement and strain tensor fields caused by the respective force multipole in an infinite homogeneous medium. W^{∞} relates the effective stiffness encountered by a cell to the elastic constants. Since strain scales inversely with elastic constants, W^{∞} decreases if the elastic constants increase. For an elastically anisotropic medium, W^{∞} varies with the direction of force application, which provides an orientational clue for cell orientation. As we will see below, tensile prestrain or boundary-induced tensile image strain also leads to an increased effective stiffness. Therefore minimization of W^{∞} corresponds to the experimentally observed cellular preference for large effective stiffness.

4.2.4 Isotropic elastic medium

The mechanical equilibrium condition Eq. (4.5) states that the applied body forces $f_i(\vec{r})$ are balanced by the internal restoring forces $\sigma_{ij,j}(\vec{r})$, where $\sigma_{ij}(\vec{r}) = C_{ijkl}u_{kl}(\vec{r})$ is the stress tensor. In the following, we will consider only isotropic elastic materials, that is there are two elastic constants, e.g. the Lamé coefficients μ and λ or Young modulus E (*elastic rigidity*) and Poisson ratio ν (that describes the relative importance of shear and compression modes). For our purpose, it is convenient to define a third pair of elastic constants, $\Lambda = \lambda/\mu$ and $c = 2\mu + \lambda = \mu(2+\Lambda)$. Therefore Poisson ratio $\nu = \Lambda/2(\Lambda+1)$ and $\nu = 1/2, 1/4$ and 0 correspond to $\Lambda \to \infty$, $\Lambda = 1$ and $\Lambda = 0$, respectively. In practice, E will be of the order of a few kPa, which is a typical value for physiological tissues (simple scaling shows that for a typical force $F = 10$ nN at focal adhesions, a deformation in the μm-range corresponds to $E = 10$ kPa). Values for the Poisson ratio ν are close to $1/2$ (incompressible medium) both for synthetic elastic substrates and physiological hydrogels. However, other values for ν might be realized in future applications, e.g. for artificial tissues or on compliant surfaces of biosensors. For isotropic elasticity, the elastic constant tensor of the medium reads $C_{ijkl} = \lambda\delta_{ij}\delta_{kl} + 2\mu\delta_{ik}\delta_{jl}$

and Eq. (4.5) is conveniently rewritten using a vector notation as:

$$\triangle\vec{u}(\vec{r}) + (1+\Lambda)\nabla\nabla\cdot\vec{u}(\vec{r}) = -\frac{\vec{f}(\vec{r})}{\mu} \qquad \vec{r} \text{ in V}, \tag{4.11}$$

which is a linear second order differential equation for the displacement field and has to be solved with the appropriate boundary conditions.

Since the differential equation Eq. (4.11) is linear, the superposition principle applies and the boundary value problem is formally solved by determining the Green tensor $G_{ij}(\vec{r},\vec{r'})$, i.e. the kernel for a point-like body force $f_i(\vec{r}) = f_i\delta(\vec{r}-\vec{r'})$. The elastic fields of more complicated force distributions can be obtained by convolution of the Green tensor with the force density, i.e. $u_i(\vec{r}) = \int G_{ij}(\vec{r},\vec{r'})f_j(\vec{r'})d^3r'$. The elastic fields resulting from force dipoles are obtained by differentiation of G_{il}, $u_i(\vec{r}) = G_{il,k}(\vec{r},\vec{r'})P_{kl}$ and $u_{ij}(\vec{r}) = G_{il,kj}(\vec{r},\vec{r'})P_{kl}$. In general, the determination of Green functions in elasticity theory for a given geometry and boundary condition is rather difficult, since the second term in Eq. (4.11) couples different components of the displacement field. By taking the Laplacian of Eq. (4.11), one arrives at the biharmonic equation $\triangle\triangle\vec{u} = 0$ for the displacements. Thus, harmonic potential theory is frequently used, for instance in the stress function χ-method [99] and in the Galerkin-vector approach [126], in addition to other methods like expansion of $\vec{u}$ in terms of a suitable complete basis set of orthonormal functions [80].

4.2.5 External strain

We now consider how a cell establishes a force pattern in a prestrained homogeneous medium. The work required to generate a force pattern in the presence of an externally imposed strain tensor field $u^e_{ij}(\vec{r})$ is given by:

$$\begin{aligned} W &= \int d^3r \int_0^{u^e_{ij}+u^{\vec{f}}_{ij}} C_{ijkl}u_{kl}(\vec{r})du_{ij}(\vec{r}) \\ &\quad - \int d^3r \int_0^{u^e_{ij}} C_{ijkl}u_{kl}(\vec{r})du_{ij}(\vec{r}) = W^\infty + \Delta W^e \end{aligned} \tag{4.12}$$

with

$$\Delta W^e = \int d^3r\ C_{ijkl}u^{\vec{f}}_{ij}u^e_{kl}(\vec{r}) = \sum_{n=0}^{\infty}\frac{1}{n!}P_{i_1\ldots i_n i}u^e_{i,i_1\ldots i_n}(\vec{r}). \tag{4.13}$$

The derivation of Eq. (4.13) proceeds along the same lines as for Eq. (4.10). In particular, for a single force dipole one gets $\Delta W^e = P_{ij} u^e_{i,j}(\vec{r})$. Because of contractile cell activity, P_{ij} has negative eigenvalues ($P < 0$). Thus, tensile prestrain ($u^e_{ij} > 0$) decreases W as does a larger rigidity E and hence is interpreted by the cell as an increase in effective stiffness (*strain-stiffening*). In contrast, compressive prestrain corresponds to a decrease in effective stiffness and hence is avoided by the cell.

4.2.6 Boundary-induced image strain

We now consider the energy involved to deform an elastic medium in the presence of a sample boundary. In order to quantify the effect introduced by the boundary, we split $u_{ij} = u^{\infty}_{ij} + u^b_{ij}$ into a contribution arising in an infinite medium u^{∞}_{ij} and a boundary induced strain field u^b_{ij} (*image strain*), that depends on sample geometry and boundary condition. $\vec{u}^{\infty}$ ensures that the force balance is satisfied everywhere in the sample volume V. However, $\vec{u}^{\infty}$ will not satisfy the boundary condition at S, that requires to introduce $\vec{u}^b$. In order to keep the force balance in the sample, the image displacements have to be homogeneous solutions of Eq. (4.11). Otherwise they can be chosen in such a way that the boundary conditions are satisfied. Now $W = W^{\infty} + \Delta W^b$, where W^{∞} is the energy of the infinite medium and ΔW^b is the additional energy due to the boundary effect. For the latter, we have

$$\Delta W^b = \frac{1}{2} \int d^3r \; f_i(\vec{r}) u^b_i(\vec{r}) + \frac{1}{2} \oint dS \; f^s_i(\vec{r}) u_i(\vec{r}) \tag{4.14}$$

which includes both the effects of fixed boundary strain and fixed boundary forces. In principle, the boundary conditions in a physiological context can be very complicated. In our calculations we will restrict ourselves to two fundamental reference cases, namely *free boundaries*, where the normal tractions vanish at the boundary, i.e. $f^s_i(\vec{r}) = 0$, and *clamped boundaries*, where the displacements vanish at the boundary, i.e. $u_i(\vec{r}) = 0$. We will refer to the former as the *Neumann problem* and to the later as the *Dirichlet problem.* In both cases, the surface integral in Eq. (4.14) vanishes. Thus, the change in effective stiffness induced by a boundary as encountered by a force dipole reads $\Delta W^b = \frac{1}{2} P_{ij} u^b_{i,j}(\vec{r})$. In this way, cells can actively sense not only the presence of a close-by surface, but also its shape and boundary condition.

4.2.7 Elastic interactions between cells

Strain fields produced by other cells may be large enough to be detected as external strain by the cell, which gives rise to an elastic interaction of cells. Even if cells have initially isotropic force patterns, they will sense anisotropic strain and begin to polarize. The change in stiffness encountered by a force pattern $\vec{f}$ centered around $\vec{r}$ caused by a second force pattern $\vec{f'}$ centered at $\vec{r'}$ reads:

$$\begin{aligned}
\Delta W^{\vec{f}\vec{f'}} &= \int d^3s f_i(\vec{r}+\vec{s}) u_i(\vec{r}+\vec{s}) \\
&= \int\int d^3s d^3s' f_i(\vec{r}+\vec{s}) G_{ij}(\vec{r}+\vec{s}, \vec{r'}+\vec{s'}) f'_j(\vec{r'}+\vec{s'}) \\
&= \sum_{n=0}^{\infty}\sum_{m=0}^{\infty} \frac{1}{n!}\frac{1}{m!} P_{i_1 \ldots i_n i} G_{ij,i_1 \ldots i_n j_1 \ldots j_m}(\vec{r}, \vec{r'}) P'_{j_1 \ldots j_m j} \ , \qquad (4.15)
\end{aligned}$$

where the indices $i_1 \ldots i_n$ denote derivatives of the Green function with respect to the unprimed coordinates and $j_1 \ldots j_m$ derivatives with respect to the primed coordinates. For translationally invariant geometries, for instance in infinite space, $G_{ij}(\vec{r}, \vec{r'}) = G_{ij}(\vec{r} - \vec{r'})$ and derivatives for j_k become equivalent to derivatives for $-i_k$. As a model for elastically interacting cells, we consider how identical, static anisotropic contraction dipoles organize in a soft medium in order to sense maximal effective stiffness in their environment. The case $n = m = 1$ in Eq. (4.15) corresponds to the force dipolar interaction:

$$\Delta W^{PP'} = P_{li} u_{i,l}(\vec{r}) = P_{li} G_{ij,lk}(\vec{r}, \vec{r'}) P'_{kj} \qquad (4.16)$$

and will be discussed in more detail below.

4.2.8 Summary modeling section

To summarize the first part of this chapter, both physical defects and active cells respond to elastic deformations in their environment and we suggest that the same mathematical formalism can be used to describe both situations. In fact, all formulae derived in this section for interactions of cells with external strain, sample boundaries and other cells as quantified by W describe the corresponding interactions of physical dipoles as quantified by V_t, with W and V_t being related to each other simply by a switch in sign. This result is typical for situations described by energies with quadratic scaling, as explained above for the simple case of a linear spring. For different situations of interest we found the same result $\Delta W = P_{ij} u_{ij}$, where u_{ij} is the strain tensor evaluated at the position of the force dipole P_{ij}. Depending on the situation of interest, this strain tensor can correspond to externally imposed strain, image strain induced by a sample boundary or strain due to the traction of other force dipoles. Our formula shows that cells can sense anisotropies in their environment only through an anisotropic probing process: if the probing process were isotropic, $P_{ij} = P\delta_{ij}$, we would find $W = Pu_{ii}$ and cells could only sense the scalar quantity u_{ii} describing the local relative change in volume, but not any tensorial quantity like the direction of external strain.

It is important to note that the above equations for active cells are not interaction potentials in a strict physical sense. Rather these equations try to quantify information that cells can gain by pulling on their environment and show how external perturbations result in changes in effective stiffness. The experimental observation that active cells prefer large effective stiffness in their environment leads to the interaction laws for cells given in Eqs. - (4.13,4.14,4.15). In this way, we can predict cellular self-organization in soft media from an extremum principle in elasticity theory, in excellent agreement with experimental results [18, 17]. The structure formation for physical dipoles follows simply by inverting the sign of the interaction laws derived for active cells. This case might also apply to artificial or inert cells [153]. For biomimetic systems, one might think of vesicles or nanocapsules which contract on adhesion to an elastic environment. For cellular systems, one might think of cells which are deficient in regard to the experimentally observed dynamic response of normal cells to elastic properties of the environment.

In regard to modeling of active cells, we assume that they probe their elastic environment through an anisotropic process in which force is of central importance, and that this process results in a cellular preference for large effective stiffness in the environment. Although the phenomena described here are closely related to cell morphology and the dynamics of focal adhesions, these aspects are not the subject of the present work. In particular, the magnitude P of the cellular force dipole tensor does not enter our predictions, in contrast to the positions and orientations represented by the dipole tensor P_{ij}. This reflects the fact that our model focuses on the extracellular properties that can be sensed by the cell. Since we avoid modelling cell morphology and dynamics of focal adhesions, we are able to describe the active behavior of cells in the same mathematical framework developed before to describe physical defects in a deformable medium. In particular, both cases require the solution of the corresponding elastic boundary value problem given in Eq. (4.5) and Eq. (4.6). In the next section, we present exact solutions for different cases of interest.

4.3 Examples of cell organization

4.3.1 Interaction with external strain

As an example for cell organization in a prestrained environment, we consider a homogeneously prestrained elastic slab with an uniaxial stress p acting along the z-axis. The other faces are traction free, i.e. the stress tensor has only one non-zero component, $\sigma_{zz} = p$. Then the corresponding strain tensor has only diagonal components $u^e_{ij} = \frac{p}{E}\{(-\nu, 0, 0), (0, -\nu, 0), (0, 0, 1)\}$ independent of position. Contraction of this external strain tensor with the force-dipole tensor P_{ij} according to Eq. (4.13) leads to:

$$\Delta W^e = \frac{pP}{E}[(1+\nu)\cos^2\theta - \nu] \ , \tag{4.17}$$

where θ is the orientation of the dipole relative to the direction of externally applied strain. Eq. (4.17) applies to both a cell on the top surface of the strained slab (elastic substrate) or inside a strained infinite elastic material (hydrogel). For tensile strain ($p > 0$) the cell senses maximal effective stiffness along the direction of stretch $\theta = 0$, thus cells orient preferentially in the direction of stretch in a prestrained environment (in Ref. [18], tensile strain has been defined with the opposite sign, thus Eq. (4.17) carries the opposite sign there, too). On the other hand, due to lateral contraction, cells in a precompressed environment ($p < 0$) will orient perpendicularly to the axis of compression, which is a combined effect of compressive strain avoidance in the z-direction and maximal tensile strain detection in the perpendicular directions, which will be most pronounced for incompressible media ($\nu \approx 1/2$). In contrast, a physical anisotropic contraction dipole, causing a local contraction of the environment along its axis, is repelled (attracted) by tensile (compressive) strain, because the negative interaction energy with the medium is reduced (increased) due to the expansion (compression) of the environment caused by the external field. Physical anisotropic contraction dipoles therefore orient in the opposite way as mechanosensing cells with respect to external homogeneous strain. As an aside, we note that there exists another interesting possibility for the reaction of a force dipole to external strain, which however cannot be described in terms of minimizing W^e or $V_t = -W_e$. Namely, if there was some mechanism which would lead to the avoidance of both tensile and conpressive strain, then the optimal configuration would be $V_t = -W_e = 0$. One easily calculates that this case corresponds to $\theta = \arccos\sqrt{\nu/(1+\nu)}$. For $\nu \approx 0.4$, this yields $\theta \approx 60°$. In fact, such an response has been reported for stationary cells on elastic substrates cyclically stretched with a 1 Hz frequency [38]. However, in this case cells are subject to large *passive* deformations, while here we are concerned with *active* mechanosensing.

4.3.2 Dipoles on elastic halfspace

Mechanically active cells adhering to an elastic substrate can interact elastically with each other according to Eq. (4.15). If the thickness of the substrate is much larger than the elastic displacements on the top surface, it can be modelled as a semi-infinite elastic space [151]. The Green function for a force applied to the surface of a semi-infinite space is given by the well known Boussinesq solution [99]. Since tangential forces are expected to be much larger than normal forces, P_{ij} can be restricted to the x-y-plane. Moreover the normal displacement component contributes very little to the elastic interaction and we may use the two-dimensional (2D) Green function, i.e. only the x- and y-components of the Boussinesq solution:

$$G_{ij}^{2D}(\vec{r},\vec{r'}) = a_1 \left\{ a_2 \delta_{ij} + \frac{R_i R_j}{R^2} \right\} \frac{1}{R}, \tag{4.18}$$

where $\vec{r} = \vec{r} - \vec{r'}$ and

$$a_1 = \frac{\Lambda(\Lambda+2)}{4\pi c(1+\Lambda)} = \frac{\nu(1+\nu)}{\pi E}\ , \quad a_2 = \frac{2+\Lambda}{\Lambda} = \frac{1-\nu}{\nu}\ . \tag{4.19}$$

Note that the case $\nu = 1/2$ has been used in Eq. (2.2) for our elastic substrate work. It is convenient to define the angles θ, θ' and α via the scalar products $\cos\theta = \vec{l} \cdot \vec{r}$, $\cos\theta' = \vec{l'} \cdot \vec{r}$ and $\cos\alpha = \vec{l} \cdot \vec{l'}$. Then the change in effective stiffness encountered by one cell due to the traction of the other is given by:

$$\Delta W^{PP'} = a_1 \frac{PP'}{2R^3} f(\theta, \theta', \alpha) \tag{4.20}$$

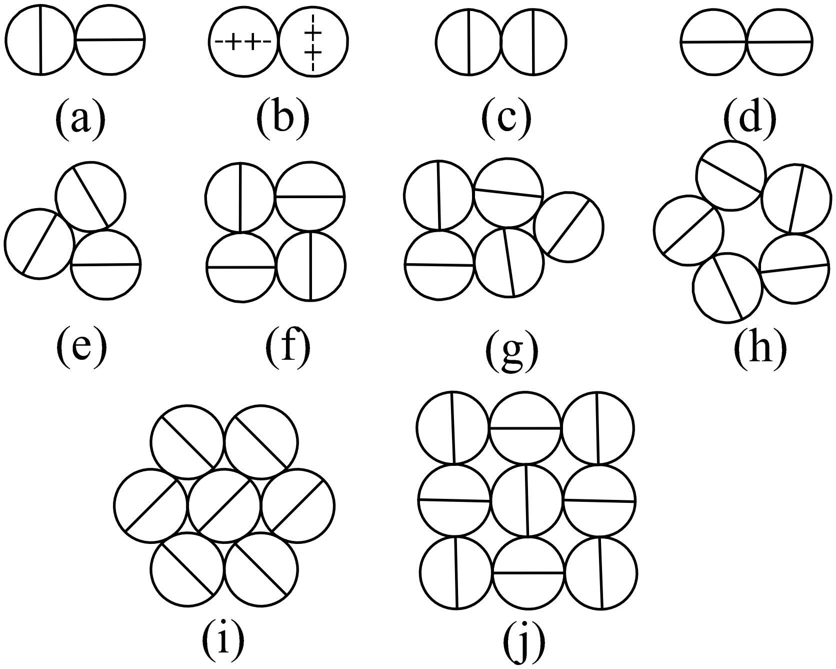

Figure 4.3: Different structures arising from elastic interactions of anisotropic force dipoles on top of an elastic halfspace. (a) Physical force dipoles for Poisson ratio $\nu \approx 1/2$ locally form a T-configuration. (b) Linear electric quadrupoles have the same optimal configuration. (c) Physical force dipoles for Poisson ratio $\nu \approx 0$ align side by side in a railway track like configuration. The crossover between (a) and (c) occurs at $\nu = 1/5$. (d) Cellular force dipoles align in strings, similar to electric dipoles and independent of the value for ν. (e) - (h) Small clusters of physical force dipoles are subject to surface reconstruction. For five particles, (g) and (h) are nearly degenerate. (i) At high densities, herringbone order results. (j) In terms of energy, the square lattice is most favorable.

with the angular dependence:

$$\begin{aligned} f(\theta,\theta',\alpha) &= 3(\cos^2\theta+\cos^2\theta'-5\cos^2\theta\cos^2\theta'-\frac{1}{3}) \\ &- (1-a_2)\cos^2\alpha-3(a_2-3)\cos\alpha\cos\theta\cos\theta'. \end{aligned} \tag{4.21}$$

Since the displacements of a force dipole scale $\sim R^{-2}$, the strain field scales $\sim R^{-3}$ with distance, which leads to a long-ranged elastic interaction ($W^{PP'} \sim R^{-3}$) typical for dipolar interactions. The complicated angular dependence in Eq. (4.21) results in a highly anisotropic interaction. Note that for the planar geometry, there are only two independent angles. Nevertheless here we prefer to write the interaction symmetric in the primed and unprimed coordinates, since this is favorable for numerical implementations.

$\Delta W^{PP'}$ has a pronounced minimum for aligned dipoles ($\theta = \theta' = \alpha = 0$), independent of ν. A contractile cell causes a local compression of the substrate underneath the cell along the contraction axis and tensile strain at more distant points. Hence at distant points maximal strain-stiffening occurs along the axis of contraction. A second cell will therefore upregulate its mechanical activity along the same direction. This scenario constitutes a positive mechanical feedback loop for cell alignment, since in the aligned configuration the mechanical activity of one cell upregulates the activity of the other and vice versa. At low cell densities, a common pattern for the organization of elastically interacting cells will therefore be the formation of strings of cells, similar to the case of electric dipoles [171]. Strings might close into rings so that each cell is fully activated by its neighbors.

The 2D case for physical dipoles has been discussed before for the isotropic case [100]. Then

$$V_t = -P\delta_{li}G_{ij,lk}(\vec{r},\vec{r'})P'\delta_{kj} = -PP'G_{ij,ij}(\vec{r},\vec{r'}) = \frac{(2+\Lambda)^2PP'}{4\pi(1+\Lambda)cR^3}. \tag{4.22}$$

Thus, for identical dipoles the interaction is isotropic and repulsive. The case of an isotropic physical dipoles is described by the negative of Eq. (4.20). Then the groundstate configuration strongly depends on the Poisson ratio ν via the angular dependence of Eq. (4.21). For incompressible media, $\nu = 1/2$ ($\Lambda \to \infty$), dipoles arrange with perpendicular orientations in a local T-configuration. This leads to rather compact structure formation, with a square lattice pattern at intermediate and a herringbone pattern at high dipole densities, similar to the situation with electric quadrupoles [153]. For highly compressible media, $\nu \to 0$ ($\Lambda \to 0$), dipoles prefer to align side by side in a railway track like configuration. For $\nu = 1/5$ ($\Lambda = 2/3$), both states have degenerate energies. Fig. 4.3 schematically shows the different structures predicted by our analysis.

4.3.3 Dipoles in elastic full space

Strain propagation in an elastic three-dimensional (3D) infinite medium is described by the Thomson Green function [99]:

$$G_{ij}^{\infty}(\vec{r}, \vec{r'}) = a_1^{\infty} \left\{ a_2^{\infty} \delta_{ij} + \frac{R_i R_j}{R^2} \right\} \frac{1}{R}, \tag{4.23}$$

with

$$a_1^{\infty} = \frac{1+\nu}{8\pi E(1-\nu)} = \frac{\Lambda + 1}{8\pi c}\ , \quad a_2^{\infty} = (3 - 4\nu) = \frac{3+\Lambda}{1+\Lambda}\ . \tag{4.24}$$

The most important result for physical dipoles is the fact that since $G_{ii}^{\infty} = 0$, the elastic interaction of isotropic dipoles in 3D vanishes [161]. Therefore their interaction is completely determined by boundary-induced interactions, like for hydrogen in metal samples of finite size [173].

For the elastic interaction of two active cells, we find

$$\Delta W^{PP'} = a_1^{\infty} \frac{PP'}{2R^3} f^{\infty}(\theta, \theta', \alpha) \tag{4.25}$$

with the angular function $f^{\infty}(\theta, \theta', \alpha)$ given by Eq. (4.21) by replacing the constants a_1 and a_2 with a_1^{∞} and a_2^{∞}, respectively. Note that in 3D there are three independent orientational degrees of freedom. In Fig. 4.4 we show a density plot of $\Delta W^{PP'}$ for dipoles with relative orientations $\alpha = 0$ and $\alpha = \pi/2$ positioned in the x-z-plane for two different values of the Poisson ratio, $\nu = 0$ and $\nu = 1/2$. Like on 2D substrates, cells in a 3D environment encounter a mechanical feedback loop favoring cell alignment. In Fig. 4.5, we show a Monte Carlo simulation of elastically interacting cells. The finite temperature used can be interpreted as a measure of the stochastic element of cell organization. As expected from Eq. (4.25), the cells form strings, which moreover are alinged in parallel due to an added external strain field in z-direction. For two parallel dipoles in z-direction placed along the z-axis,

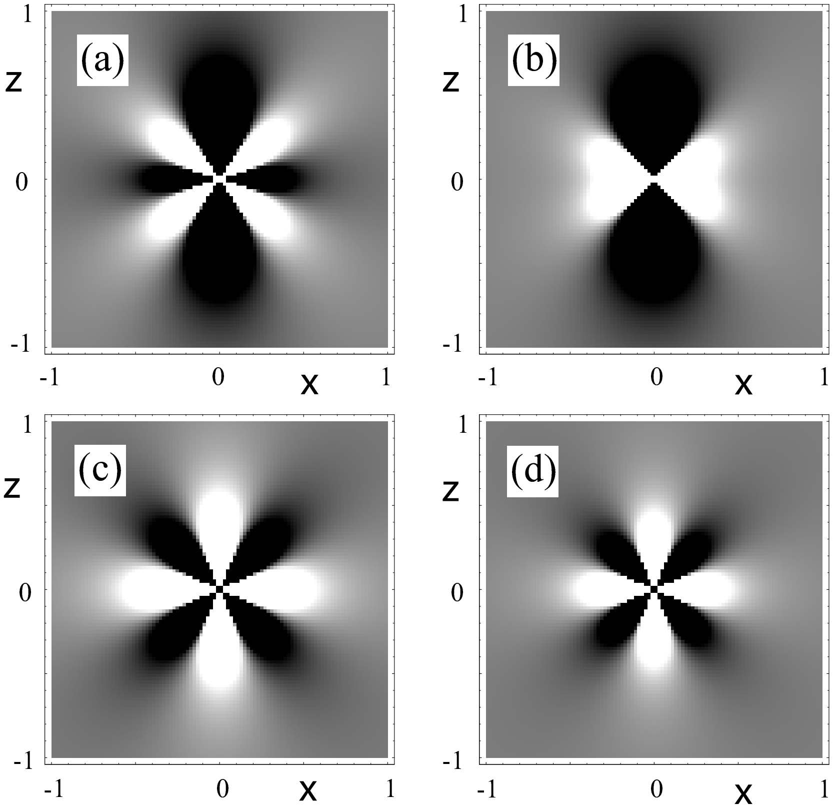

Figure 4.4: Density plots of cellular interaction potential $\Delta W^{PP'}$ from Eq. (4.25) for (a,b) parallel and (c,d) perpendicular orientations. In (a,c), Poisson ratio $\nu = 1/2$, and in (b,d), $\nu = 0$. One dipole oriented along the z-axis is fixed at the origin, while the other is moved in space. Black denotes areas of attraction and white areas of repulsion. The interaction potential for physical force dipoles simply differs in sign, thus black and white exchange meaning. (a,b) Independent of the value for ν, two cells prefer alignment (black region along z-axis). The interaction in the railway track configuration (along x-axis) changes sign at $\nu = 1/4$, when the black cone vanishes. (c,d) The T-configuration is the ground state for physical dipoles in 3D independent of the value for ν (white regions along z- and x-axes). This is different on an elastic halfspace, in which case the groundstate changes from the T- to the railway track configuration for $\nu = 1/5$.

Eq. (4.25) gives

$$\Delta W^{PP'} = -\frac{(\Lambda+2)P^2}{2\pi c}\left(\frac{1}{z}\right)^3 , \tag{4.26}$$

which yields the optimal configuration independent of the value for Λ (or, equivalently, ν). Again this behaviour is similar to the ones of electric dipoles [171]. For two parallel dipoles in z-direction placed along the x-axis (railway track configuration), we find

$$\Delta W^{PP'} = \frac{(\Lambda-1)P^2}{8\pi c}\left(\frac{1}{x}\right)^3 . \tag{4.27}$$

Thus $\Delta W^{PP'}$ changes sign as Λ varies through 1 ($\nu = 1/4$). Finally, in the T-configuration, where the first dipole is fixed in z-direction at the origin and the second dipole is positioned in the x-y-plane oriented perpendicular to the z-axis, we find:

$$\Delta W^{PP'} = -\frac{(\Lambda+1)P^2}{4\pi c}\left(\frac{1}{r}\right)^3 \tag{4.28}$$

which is always positive and yields a globally maximal $\Delta W^{PP'}$. Therefore it corresponds to a globally minimal $V_t = -\Delta W^{PP'}$ and the T-configuration is the groundstate of two physical anisotropic contraction dipoles, independent of the value for ν. The aggregation of physical dipoles in 3D is more complicated than in 2D, since the T-configuration cannot be continued in 3D without causing frustration. This leads to the existence of many metastable states.

4.3.4 Dipoles in elastic halfspace

The elastic isotropic halfspace with a clamped surface at $r_3 = 0$ constitutes a Dirichlet problem with vanishing displacements at the planar boundary, $u_i(\vec{r}) = 0$ for $r_3 = 0$, whereas the free surface leads to a Neumann boundary value problem with vanishing surface tractions, $\sigma_{ij}(\vec{r})n_j = 0$ for $r_3 = 0$ with $\vec{n} = (0, 0, 1)$ being the surface normal. The boundary value problem of the semi-infinite space can be solved using the concept of image singularities. Image approaches are well known from electrostatics: the simplest example is the charge in front of a metal plate. Here, the field due to a charge Q at

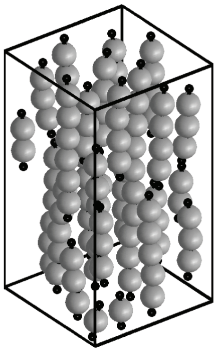

Figure 4.5: Monte Carlo simulations of elastically interacting cells in an external strain field. The temperature used in the simulation represents the stochastic element of the process of cell organization. Without external strain, cells form strings. In its presence, strings align in parallel.

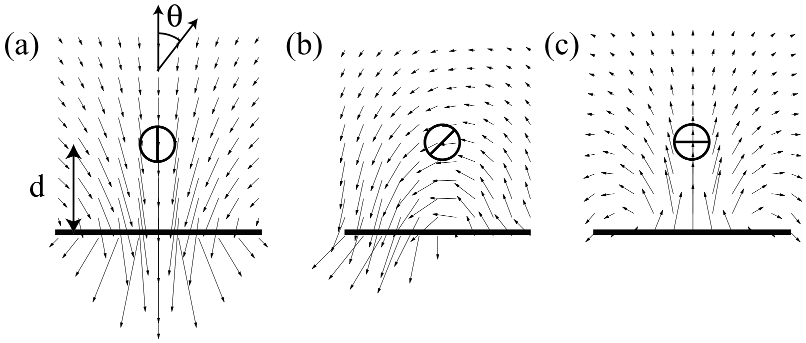

Figure 4.6: Image fields $\vec{u}^b$ for a contraction dipole P_{ij} positioned at $\vec{r'} = (0, 0, d)$ in front of a clamped surface of a semi-infinite space for Poisson ratio $\nu = 1/2$. Dipole orientations are (a) $\theta = 0$, (b) $\theta = \frac{\pi}{4}$ and (c) $\theta = \frac{\pi}{2}$ with respect to the surface normal. At the clamped surface the image displacements $\vec{u}^b$ balance the displacements $\vec{u}^\infty$ of an infinite space. Inside the sample, they are homogeneous solutions of the elastic equations. The interaction of a dipole with the clamped surface is equivalent to the interaction of the dipole with a set of image singularities placed at $\vec{r'}_{\mathrm{im}} = (0, 0, -d)$. For a free surface, the normal tractions vanish and all image displacements change sign. For $\nu < 1/2$, there is an additional contribution to $\vec{u}^b$ derived from line images. However, the interaction of force dipoles with the boundary does not change qualitatively as ν is varied.

$\vec{r'} = (r'_1, r'_2, r'_3)$ with the boundary at $r_3 = 0$ is equivalent to the field of the charge and an image charge $-Q$ at $\vec{r'}_{\mathrm{im}} = (r'_1, r'_2, -r'_3)$ without a boundary. In analogy, the displacement field due to a unit force at $\vec{r'}$ close to a planar surface of a semi-infinite space is equivalent to the superimposed fields of a set of force nuclei placed in a homogeneous infinite substrate, i.e.:

$$G_{ij}(\vec{r}, \vec{r'}) = G^{\infty}_{ij}(\vec{r}, \vec{r'}) + G^{\mathrm{im}}_{ij}(\vec{r}, \vec{r'}), \tag{4.29}$$

where G^{∞}_{ij} is the Green function in an infinite medium, Eq. (4.23), and G^{im}_{ij} specifies its image system, which is a sum of functions derived from G^{∞}_{ij} by differentiation (point images, i.e. forces and force dipoles) or integration (line images, i.e. a line of force nuclei). Despite its rather simple geometry, the image system of the elastic half-space is rather complicated and consists of up to 15 image nuclei, including point nuclei located at $\mathbf{r}'_{\mathrm{im}} = (r'_1, r'_2, -r'_3)$ and line images running normal to the surface and extending from $-r'_3$ to infinity. The image system of the free halfspace was calculated by Mindlin using a Boussinesq-Galerkin representation [126]. The Green function of the clamped half-space has been derived by Phan-Thien applying a Papkovitch-Neuber ansatz, however without revealing the image system in detail [136]. Quite recently, Walpole [174] used methods of general harmonic potential theory and presented the image system for two joined half-spaces, which includes the clamped or free half-space as limiting cases of infinite or vanishing shear rigidity in one of the joined spaces. Using his results, we obtained exact expressions for G^{im}_{ij} for both the clamped and free boundary conditions [17]. In Fig. 4.6 we plot the image displacements $\vec{u}^b$ resulting by differentation of the image Green function for three different dipole orientations with respect to the surface normal of a clamped halfspace. For the value $\nu = 1/2$ used here for the Poisson ratio, all image displacements happen to point in the opposite direction for a free surface.

According to Eq. (4.14), the change in effective stiffness encountered by a force dipole P_{ij} positioned a distance $r'_3 = d$ away from the surface is proportional to the induced image strain at the position of the dipole, i.e. $\Delta W^b(\vec{r'}) = \frac{1}{2} P_{ij} \frac{\partial^2 G^{\mathrm{im}}_{ik}(\vec{r}, \vec{r'})}{\partial r_j \partial r'_l} P_{kl}|_{\vec{r} \to \vec{r'}}$. Because of rotational symmetry with respect to the surface normal, the surface induced change in effective stiffness sensed by a dipole depends only on its distance d to the surface and the angle $\cos\theta = \vec{n} \cdot \vec{l}$ between dipole orientation and surface normal. We find:

$$\Delta W^b(d, \theta) = \frac{P^2}{256\pi E d^3}(a_\nu + b_\nu \cos^2\theta + c_\nu \cos^4\theta), \tag{4.30}$$

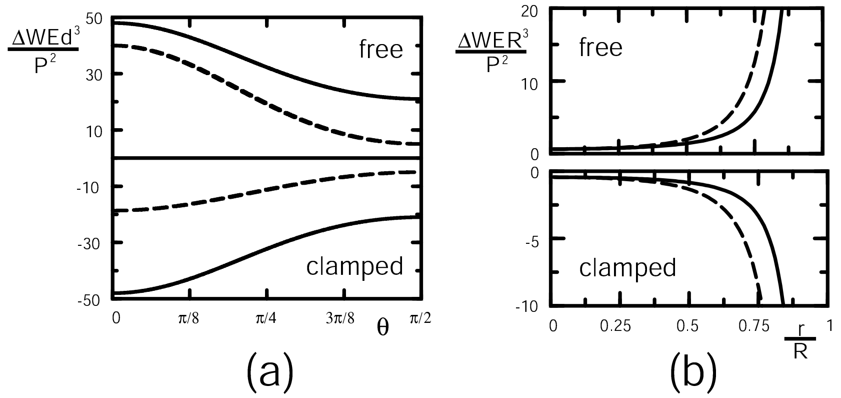

Figure 4.7: (a) ΔW for a cell with dipole strength P which is a distance d away from the surface of an elastic halfspace with rigidity E, plotted in units of P^2/Ed^3 as a function of angle θ between cell orientation and surface normal (rescaled by 256π). Solid and dashed lines correspond to Poisson ratios $\nu = 1/2$ and $\nu = 0$, respectively. (b) ΔW for a cell in an elastic sphere of radius R, plotted in units of P/ER^3 as a function of distance r to the sphere center in units of R for $\nu = 1/3$ (rescaled by 15/8). Solid and dashed lines are parallel ($\theta = \pi/2$) and perpendicular ($\theta = 0$) orientations, respectively (all other orientations yields curves which lie inbetween the ones shown).

with the coefficients

$$\begin{aligned}
a_\nu^f &= \frac{(1+\nu)(5+2\nu(6\nu-1))}{1-\nu} & a_\nu^c &= -\frac{(1+\nu)(15+32\nu(\nu-1))}{(1-\nu)(3-4\nu)} \\
b_\nu^f &= \frac{(1+\nu)(22+4\nu(2\nu-9))}{1-\nu} & b_\nu^c &= -\frac{(1+\nu)(34+32\nu^2-72\nu)}{(1-v)(3-4\nu)} \\
c_\nu^f &= \frac{(1+\nu)(13(1-2\nu)+12\nu^2)}{1-\nu} & c_\nu^c &= -\frac{(1+\nu)(7-8\nu)}{(1-\nu)(3-4\nu)}
\end{aligned} \tag{4.31}$$

being rational function of the Poisson ratio ν. ΔW^b scales quadratically in P, because the image strain scales linearly in P, in other words, the force dipole interacts with its own images. The interaction of the force dipole with the surface is a long-ranged effect and scales like a dipole-dipole interaction potential, that is $\sim d^{-3}$. For free and clamped surfaces, all coefficients in Eq. (4.31) are positive and negative, respectively, irrespective of ν. Therefore, the prefered cell orientation close to the surface , i.e. the configurations of

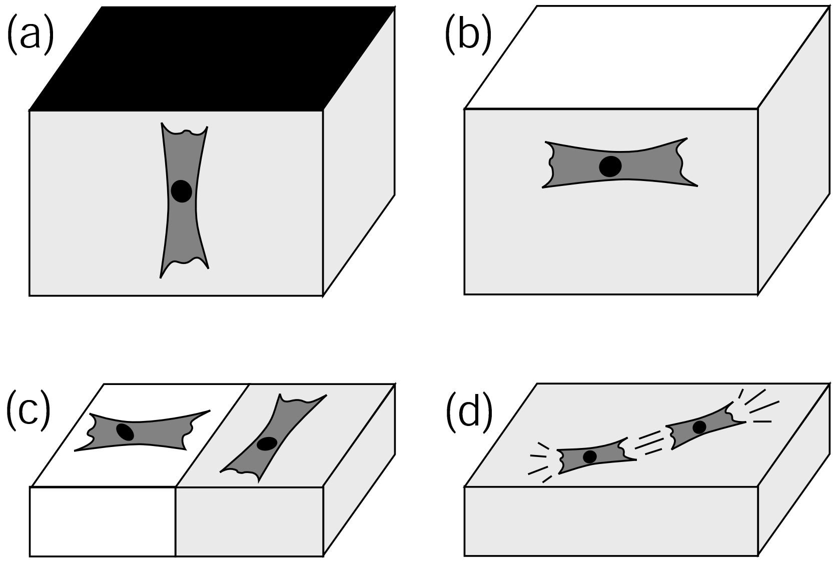

Figure 4.8: Predicted cell orientation in a hydrogel close to a surface (a,b) and on elastic substrates (c,d). (a) Cells prefer the direction of maximal effective stiffness. Thus, they orient perpendicular to a clamped surface. (b) For a free surface, this direction is parallel to the surface. (c) Cells close to a boundary between soft (left) and rigid (right) regions prefer analogous orientations as cells close to clamped and free surfaces in a hydrogel, respectively. (d) Cells interact elastically to form strings, because in nose-to-tail alignment, the mechanical activity of one cell triggers the one of the other cell, thereby forming a positive feedback loop.

minimal ΔW^b, are parallel ($\theta = \pi/2$) and perpendicular ($\theta = 0$) orientation for free and clamped boundaries, respectively. In Fig. 4.7a we plot the angular dependence of ΔW^b for $\nu = 1/2$ and $\nu = 0$.

Since $|\Delta W^b| \sim 1/d^3$ increases if d decreases, the overall mechanical activity of a cell increases towards a clamped surface ($\Delta W < 0$), but decreases towards a free surface ($\Delta W > 0$). Thus we predict that cells preferentially locomote towards a clamped boundary, but tend to migrate away from a free boundary. In general, free and clamped boundaries have always opposite effects. One may think of a clamped (free) surface as the interface between the medium and an imaginary medium of infinite (vanishing) rigidity, which effectively rigidifies (softens) the medium towards the boundary. Thus for clamped (free) boundary conditions, the cell senses maximal stiffness towards (away) from the boundary. For clamped boundaries, mechanical activity of cells is favored and cells can amplify this effect by adjusting orientation. For free boundaries, mechanical activity of cells is disfavored and the orientation response is an aversion response. In Fig. 4.8a-c, we schematically depict our predictions for cell organisation near boundaries.

For the interaction of a physical dipole with the surface, we simply have to switch sign in Eq. (4.30). Hence, physical dipoles are attracted by free and repelled from clamped surfaces. A clamped surface prevents the defect from displacing its environment to lower its potential energy, which results in a repulsive interaction. In contrast a free surface favors displacements close to the surface since at a free surface there exist no internal restoring forces acting normal to the surface. This results in an attractive interaction of the defect with the surface. Since $V_t \sim P^2$, the sign of P does not matter, i.e. dilation and contraction dipole interact in the same way with the surface.

4.3.5 Dipoles in elastic sphere

As an example for a finite sized sample, we consider the elastic sphere with radius R. Before we turn to the full problem of anisotropic dipoles, it is instructive to consider the simple case of an isotropic force dipole $P_{ij} = P\delta_{ij}$ at the center of the sphere. The displacement in an infinite sample is

$$u_i^{inf} = -G_{ij,k}P_{kj} = \frac{P}{4\pi c}\frac{x_i}{r^3} \ . \tag{4.32}$$

We now have to use solutions of the homogeneous differential equation in order to arrive at an image displacement which guarantees the correct boundary conditions. In this highly symmetric case, it is sufficient to use the trivial, i.e. linear solution as an ansatz:

$$u_i^{img} = a x_i \tag{4.33}$$

where a has to be determined from the boundary conditions. For force dipoles in general, $\mathbf{u}^{inf}$ diverges $\sim 1/r^2$ and $\mathbf{u}^{img}$ vanishes at the origin. For a free spherical surface, $n_j = x_j/r$ and normal stress is

$$\sigma_{ij}^{inf} n_j + \sigma_{ij}^{img} n_j = \frac{-P\mu}{\pi c}\frac{x_i}{r^4} + a\mu(2+3\Lambda)\frac{x_i}{r} \ . \tag{4.34}$$

If normal stress should vanish at $r = R$, we need

$$a_{free} = \frac{P}{\pi c(2+3\Lambda)R^3} \ . \tag{4.35}$$

Therefore the effect of the free surface is to *increase* the radial displacement at the boundary (for a force dilation dipole, that is $P > 0$; for a force contraction dipole, $P < 0$, all displacements change sign). For a clamped surface, the displacement at the boundary has to be *decreased* to cero:

$$a_{clamped} = \frac{-P}{4\pi c R^3} \ . \tag{4.36}$$

The elastic interaction between isotropic force dipoles vanishes in an infinite isotropic elastic medium. However, for finite sized samples, an interaction is induced by the image displacements:

$$W = -P_{ij}\partial_i u_j = -P\epsilon_{ii} = -3Pa \ . \tag{4.37}$$

Thus this interaction is attractive and repulsive for free and clamped surfaces, respectively. It is independent of separation and vanishes $\sim 1/R^3$ for large R.

For the general problem of the elastic sphere, no image system has been constructed that solves the elastic boundary value problem and it is not clear whether such an image system exists. Nevertheless, the elastic equations for the elastic sphere can be solved analytically by applying an expansion in terms of vector spherical harmonics. This approach has been used by Hirsekorn and Siems [80] to solve the Neumann problem of an anisotropic force dipole in an elastic sphere with a free boundary. We will follow this approach also in order to solve the Dirichlet problem of a force dipole in a clamped sphere. Both results are then used to calculate the change in effective stiffness encountered by a force dipole in clamped and free spheres, respectively.

Analytical solutions to differential equations for scalar fields in spherical coordinates can be obtained by an expansion in terms of spherical harmonics, which form a complete orthonormal basis set on the unit sphere. In a similar way, the general solution to the equilibrium condition Eq. (4.11) for the vector field $\vec{u}(\vec{r})$ can be expressed as a sum over so-called *vector spherical harmonics* (VSH). These calculations are rather involved [17]. Our results can be shown to simplify in the limit of isotropic force dipoles to the results

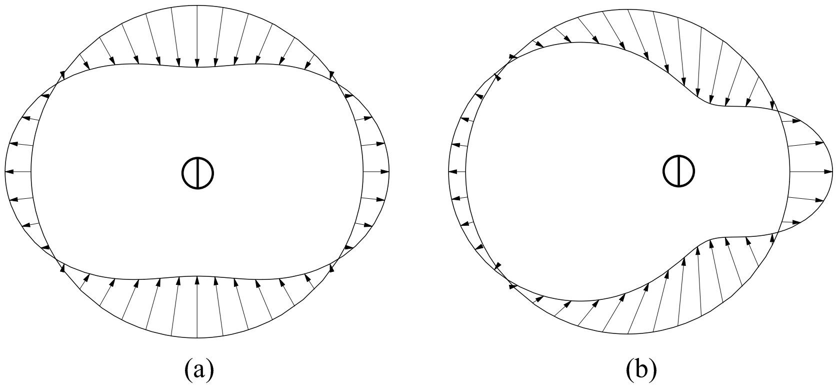

Figure 4.9: Deformation of an elastic sphere ($R = 1$, $\Lambda = 2$, $c = 1$) with a free surface by a contraction dipole oriented in the z-direction. In (a) the dipole is placed at the origin, $\vec{r} = (0,0,0)$. In (b) the dipole is placed off-center at $\vec{r} = (\frac{R}{4},0,0)$. The pictures show a cut through the x-z-plane, but it has rotational symmetry only in (a).

obtained formerly for the case of hydrogen in metal [173]. In Fig. 4.9 we use our results to plot two examples for a deformed elastic sphere with free boundaries under the action of a contraction dipole. The final result for ΔW^b, that is for the interaction of the dipole with the sphere surface, has the following scaling form:

$$\Delta W^b = \frac{P^2}{ER^3} f_\nu(\frac{r}{R},\theta) \ , \tag{4.38}$$

where r is the distance to the sphere center and θ is the dipole orientation with respect to the surface normal. The function f_ν contains a sum over all angular momenta of the expansion in vector spherical harmonics and does not vary qualitatively as ν (or, equivalently, Λ) is varied. With regard to cell orientation, we find the same results as for the elastic halfspace: cells will orient parallel (perpendicular) to a free (clamped) surface, respectively. As shown in Fig. 4.7b, we also find a similar result for the effect of distance to the surface: for free (clamped) boundary conditions, a small (large) distance to the sphere center is more favorable, since the surface favors (disfavors) mechanical activity. The new aspect here is the role of the sphere radius R. Since $|\Delta W|$ increases when R decreases, one can effectively rigidify (soften) a material with a clamped (free) surface by reducing system size. For the in-

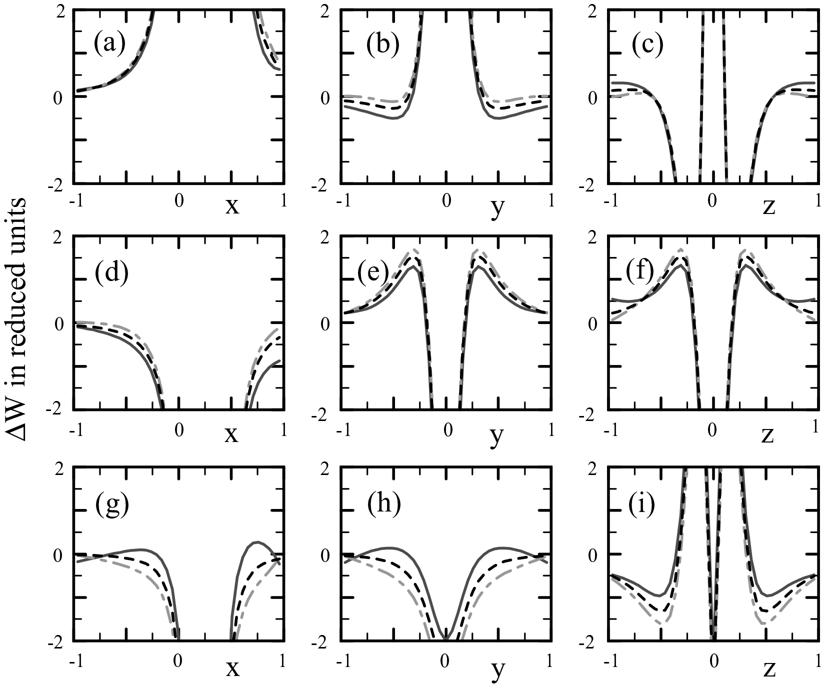

Figure 4.10: Cellular dipole-dipole interactions $\Delta W = \Delta W^{\infty} + \Delta W^{b}$ in an elastic sphere ($\Lambda = 2$) in units of PP'/cR^3 for clamped (dashed gray) and free (full gray) boundary conditions. A z-dipole is fixed at $\vec{r} = (\frac{R}{4}, 0, 0)$. A x-dipole (a,b,c), y-dipole (d,e,f) and z-dipole (g,h,i) is moved along the coordinate axes. The boundary condition introduces corrections to the interaction in infinite medium (black line).

teraction of a physical dipole with the surface embedded in an elastic sphere, we once more obtain the opposite results. Dipoles are attracted (repelled) and orient towards (away from) a free (clamped) surface.

So far we have considered the interaction of a force dipole with the boundary. One may extend our model of cell-cell interactions to cells embedded in finite geometries and study how their boundaries alter the interaction between cells. In an elastic sphere containing many cells, we can separate the contributions to the effective stiffness into a contribution from the boundary induced field, i.e. a cell-surface interaction as discussed above, and a contribution from the elastic fields of other cells embedded in the sphere, i.e. a cell-cell interaction term. This contribution is modified with respect to the interaction term in infinite medium, Eq. (4.26), by a boundary mediated interaction term. The indirect interaction term is given by contracting the dipole tensor of the first dipole with the image strain caused by the second dipole. The most important result here is that the image term varies on the macroscopic scale R. For physical dipoles, elastic interactions in finite sized geometries have been studied extensively, in particular for *isotropic* dipoles, that do not interact in infinite medium and where the interaction between dipoles is mediated solely via the boundary [173]. The interaction of physical isotropic defects is always attractive (repulsive) for isotropic dipoles in a free (clamped) sphere. Due to the macroscopic interaction range of isotropic physical dipoles the indirect interactions lead to structure formation on the macroscopic scale (*macroscopic modes*), e.g. in hydrogen-metal alloys. For anisotropic dipoles the image interaction introduces corrections to the direct interaction term, which vary on the macroscopic scale. In Fig. 4.10 we plot the interaction of two anisotropic dipoles in infinite medium and the modified interactions in clamped and free spheres, respectively. For example, the image correction in a free sphere for two parallel z-dipoles (one placed at the sphere center) along the x-axis reads

$$\begin{aligned}\Delta W^b(x) = PP'\big((112 + 352\Lambda + 370\Lambda^2 + 135\Lambda^3) \\ - 12(7+4\Lambda)(2+5\Lambda+3\Lambda^3)\left(\frac{x}{R}\right)^2\big)/\big(4(2+3\Lambda)(14+19\Lambda)\pi c R^3\big)\ .\end{aligned} \tag{4.39}$$

For $\Lambda \to \infty$ ($\nu = 1/2$), this becomes

$$\Delta W^b(x) = \frac{PP'}{76\pi\mu R^3}\left[45 - 48\left(\frac{x}{R}\right)^2\right]\ . \tag{4.40}$$

For a clamped sphere, we find

$$\Delta W^b(x) = \frac{PP'\left[-(686 + 280\Lambda + 24\Lambda^2) + 45(1+\Lambda)(7+4\Lambda)\left(\frac{x}{R}\right)^2\right]}{120(7+2\Lambda)\pi c R^3} \tag{4.41}$$

which for $\nu = 1/2$ becomes

$$\Delta W^b_{\mathrm{c}}(x) = \frac{PP'}{20\pi\mu R^3}\left[-2 + 15\left(\frac{x}{R}\right)^2\right]\ . \tag{4.42}$$

Again we find that clamped and free surface result in opposite effects. On the microscopic scale (i.e. for small cell-cell distances), the direct interaction

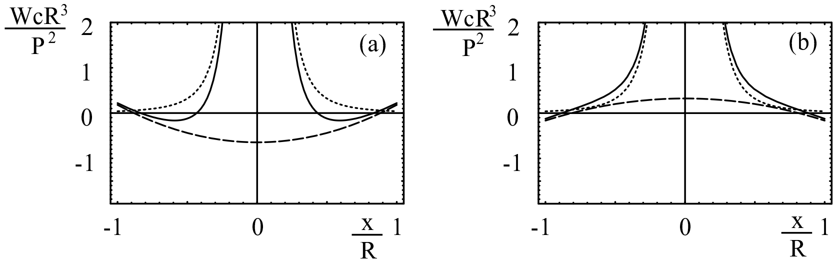

Figure 4.11: Elastic interaction energy V_t in units of P^2/cR^3 for two parallel anisotropic physical force dipoles of magnitude P in an isotropic elastic sphere with radius R and elastic constants c and $\Lambda = 2$ (Poisson ratio $\nu = 1/3$). For this value of Λ, the direct elastic interaction is repulsive (dotted lines). (a) Free surface: the image correction (dashed line) is attractive and generates a new minimum in the full interaction potential (solid line). (b) Clamped surface: the image correction is repulsive.

dominates. For macroscopic cell separations, the boundary term introduces significant contributions that dominate over the direct term close to the surface. For some cases, the boundary can induce new maxima or minima in the dipole-dipole interaction landscape. Note that for a full treatment, the dipole-surface interactions have to be included. In conclusion, in contrast to isotropic dipoles, structure formation of anisotropic dipoles is dominated by effects on cellular and elastic scales, which result from direct interactions. Since they compete with boundary induced effects on a macroscopic scale, in general we expect hierarchical structures.

4.3.6 Summary example section

In the second part of this chapter, we applied the general formalism from the first part to different situations of interest. In general, we found that physical and cellular force dipoles interact in opposite ways with each other, external strain field or sample boundaries, because $V_t = -W$. For example, physical anisotropic force dipoles on top of thick elastic films or in infinite elastic material locally prefer the T-configuration (for Poisson ratio $\nu = 1/2$), while cellular anisotropic force dipoles align in strings (independent of the value for ν). The predicted structure formation for physical force dipoles and active cells is similar to the ones of electric quadrupoles and dipoles, respectively. We also found that in general, free and clamped boundaries will have opposite effects. For example, cellular anisotropic force dipoles are repeled and attracted by free and clamped boundaries, respectively. In the vicinity of these boundaries, they will align in parallel and perpendicular, respectively. In general, all the interaction laws derived here show the universal scaling $W \sim (P^2/El^3) f_\nu(\theta_i)$, where f is a non-trivial function of Poisson ratio ν and the different angles θ_i, which has to be calculated for each situation of interest. Except for the case of external strain, the cellular force pattern interacts with itself (case of boundaries) or with another cellular force pattern (case of elastic interaction of cells), therefore $W \sim P^2$. The scaling $W \sim 1/l^3$ is typically for force dipoles. Here the length l can either be distance (e.g. between cell and boundary or between two cells) or sample size (in the elastic sphere). Finally, $W \sim 1/E$. Although W decreases with increasing Young modulus E, that is elastic effects become smaller, at the same time mechanical activity of cells usually increases. For this reason, we expect that there exists a range of optimal values for E for which the elastic effects in cell adhesion described here should be most pronounced (possibly around $E = kPa$, the physiological order of magnitude for cell and tissue stiffness).

Our predictions for cell organization in soft media are in excellent agreement with experimental observations. Cell orientation with the direction of external strain has been reported experimentally many times, both for fibroblast on elastic substrates [77] and in collagen gels [9, 45]. In the experimental community, it is also well known that mechanical activity of cells increases for clamped boundary conditions [68]. The predicted orientation effects close to boundaries have been observed numerous times, e.g. the parallel orientation of cells close to free surfaces [9]. Our model predicts the same orientation effects for an elastic substrate with two regions of different rigidities (Fig. 4.8c): cells on the soft and stiff sides of the boundary orient perpendicular and parallel to it, respectively. Indeed fibroblasts migrating from a soft to a stiff region keep their perpendicular orientation and cross over to the stiff side, while fibroblasts migrating from a stiff to a soft region do not cross the boundary, but turn by 90 degrees and move parallel to the boundary [116]. Cell organisation in elastic spheres has been monitored before mainly for rather large cell densities, e.g. for fibroblast-populated collagen microspheres, an assay which has been introduced to study compaction of tissue equivalents [127]. In order to study the interaction between single cells and boundary discussed above, one had to use much lower cell densities. In general, collective effects might be of large importance when studying tissue equivalents. For example, it has been reported that when boundary condition are changed from clamped to free by cutting the collagen gel, fibroblasts show the predicted reorientation by 90 degrees only when sufficiently many cells are present [168]. In fact our calculations and simulations show that cells can orient in parallel even with respect to clamped boundaries, if there are sufficiently many cells such that the direct elastic interaction between cells dominates the single cell response of perpendicular orientation. In practice, the single cell response might also be disturbed because elastic signals could be screened by traction of randomly oriented cells. Indeed such an effect has been reported for experiments with elastic substrates [116].

4.4 Conclusions

It has long been known, especially in the medical and bioengineering communities, that cell organization in soft media is strongly influenced by the mechanical properties of the environment. Here we presented a model which is able to explain numerous experimental observations that have been reported for organization of cells (especially fibroblasts) both on elastic substrates and in hydrogels. The excellent agreement of our results with experiments suggests that cell organization can be predicted from local mechanical properties which the cell actively senses in its environment. In fact the only property of cellular regulation which enters our model is the assumption that cells locally prefer large effective stiffness. Otherwise our modelling focuses on the elastic properties of the extracellular environment.

We close this chapter by discussing some open issues. Modelling the soft environment of cells as an isotropic elastic medium is certainly a good assumption for elastic substrates. The situation is more complicated for hydrogels, in particular because they might not behave elastically and because they feature fiber degrees of freedom. Cell organization in gels is often explained by contact guidance, the alignment of cells along topographic features like collagen fibers. Since fibers can become aligned due to cell traction, contact guidance provides a long-ranged and persistent mechanism for cellular self-organization in tissue equivalents [132]. This process has been modeled before. In the theory of Ref. [132], flux equations for cellular and matrix densities are combined with mechanical equations which include cells as centers of isotropic contraction. This might be a good model for chondrocytes, which tend to show a spherical morphology. The anisotropic biphasic theory (ABT) from Ref. [7] aims at cells like fibroblasts and smooth muscle cells, whose typical morphology in tissue equivalents is bipolar. ABT introduces a cell orientation tensor, which is coupled to a fiber orientation tensor, since cells are assumed to react foremost to fiber degrees of freedom. In our model, the force dipole tensor represents cell orientation as does the cell orientation tensor in ABT, but it is coupled to elastic degrees of freedom, since cells are assumed to react foremost to large effective stiffness.

Because models for contact guidance in tissue equivalents focus on fiber degrees of freedom and high cell densities, they do not explain the single cell responses observed on elastic substrates, where contact guidance usually is ruled out [77, 116]. The large predictive power of our model for elastic substrate experiments suggests that active mechanosensing by single cells might also be involved with cell organization in hydrogels. However, for the collagen assay from Ref. [63] it has been shown that as a result of external strain, fibers become rearranged and stress relaxes towards zero. In a matrix which cannot support any stress, our elastic considerations do not apply and contact guidance through formerly aligned fibers might be the only relevant clue for cell organization [63]. However, it is important to note that in our model, stress is actively generated by cells and thus needs to be supported only over time scales in which the cell actively senses the mechanical properties of its environment. In particular, if fiber alignment has resulted in some anisotropic mechanical environment, the cell might sense the anisotropic mechanical properties of the matrix and orient itself correspondingly. This might explain why cells have been found to align to a greater extent with respect to external strain than the surrounding collagen fibrils [63] and why our modelling is also successful for hydrogels. In general, future experiments are needed to clarify the relative importance of topographic versus mechanical clues for cell organization in hydrogels, while future modelling is needed to account for the mechanical (in particular, viscoelastic) properties of hydrogels.

We also want to point out that contact guidance is a bidirectional clue and provides only guidance, in contrast to external elastic strain, which provides taxis. In our model, taxis is reflected by the position dependence of ΔW. For example, our theory not only predicts that cells prefer to orient parallel to free boundaries, but also that cells prefer to move away from them. Moreover a simple preference for cell alignment along fibers does not predict what cells do if they encounter a fiber junction in the gel. Although we are not concerned with cell locomotion here, our modelling would suggest that cells prefer the fiber under largest tension, exactly as has been observed experimentally for neutrophils migrating in human amnion [120].

As explained before, there is a growing body of evidence now that integrin-based cell-matrix contacts act as local mechanosensors which channel mechanical information about the environment directly into cellular decision making. Although this does not concern our modelling directly, here we suggested that the upregulation of growth of cell-matrix contacts in a stiff environment might result from the fact that it is triggered by a threshold in force, whose build-up is more efficient for larger stiffness. An equivalent viewpoint is that growth of cell-matrix contacts is faster on stiffer substrates. As experimental test for this hypothesis, we suggest correlation studies for growth of cell-matrix contacts and cellular organization, especially close to sample boundaries, where cells can amplify the mechanical input provided by boundary induced strain through active mechanosensing. Quantitative data about growth behavior of cell matrix contact will allow us to further refine our model in a more quantitative way, possibly also including modelling of cellular features like morphology and force pattern, which are not the focus of this work.

Since elastic effects are long-ranged and propagate quickly, they provide an appealing mechanism for signal transduction for mechanically active cells in soft media. However, they are also unspecific and cells might not be able to distinguish between different sources. On the other hand, additional information channels, like soluble ligands, will certainly supplement elastic signals. Moreover, cells in highly differentiated organisms are likely to interprete mechanical signals only in their own physiological context, which is more restricted than for cells in an arbitrary environment.

Bibliography

[1] M. Abercrombie and G. A. Dunn. Adhesions of fibroblasts to substratum during contact inhibition observed by interference reflection microscopy. *Exp. Cell Res.*, 92:57–62, 1975.

[2] B. Alberts, A. Johnson, J. Lewis, M. Raff, K. Roberts, and P. Walter. *Molecular biology of the cell.* Garland Science, New York, 4th ed. edition, 2002.

[3] R. Alon, S. Chen, R. Fuhlbrigge, K. D. Puri, and T. A. Springer. The kinetics and shear threshold of transient and rolling interactions of L-selectin with its ligand on leukocytes. *Proc. Natl. Acad. Sci. USA*, 95:11631–11636, 1998.

[4] R. Alon, S. Chen, K. D. Puri, E. B. Finger, and T. A. Springer. The kinetics of L-selectin tethers and the mechanics of selectin-mediated rolling. *J. Cell Biol.*, 138:1169–1180, 1997.

[5] R. Alon, D. A. Hammer, and T. A. Springer. Lifetime of the P-selection-carbohydrate bond and its response to tensile force in hydrodynamic flow. *Nature*, 374:539–542, 1995.

[6] N. Q. Balaban, U. S. Schwarz, D. Riveline, P. Goichberg, G. Tzur, I. Sabanay, D. Mahalu, S. Safran, A. Bershadsky, L. Addadi, and B. Geiger. Force and focal adhesion assembly: a close relationship studied using elastic micro-patterned substrates. *Nat. Cell Biol.*, 3:466–472, 2001.

[7] V. H. Barocas and R. T. Tranquillo. An anisotropic biphasic theory of tissue-equivalent mechanics: the interplay among cell traction, fibrillar network deformation, fibril alignment, and cell contact guidance. *J. Biomech. Eng.*, 119:137–145, 1997.

[8] W. Baumgartner, P. Hinterdorfer, W. Ness, A. Raab, D. Vestweber, H. Schindler, and D. Drenckhahn. Cadherin interaction probed by atomic force microscopy. *Proc. Nat. Acad. Sci. USA*, 97:4005–4010, 2000.

[9] E. Bell, B. Ivarsson, and C. Merrill. Production of a tissue-like structure by contraction of collagen lattices by human fibroblasts of different proliferative potential *in vitro*. *Proc. Natl. Acad. Sci. USA*, 76:1274–1278, 1979.

[10] G. I. Bell. Models for the specific adhesion of cells to cells. *Science*, 200:618–627, 1978.

[11] G. I. Bell, M. Dembo, and P. Bongrand. Competition between nonspecific repulsion and specific bonding. *Biophys. J.*, 45:1051–1064, 1984.

[12] K. A. Beningo, M. Dembo, I. Kaverina, J. V. Small, and Y.-L. Wang. Nascent focal adhesions are responsible for the generation of strong propulsive forces in migrating fibroblasts. *J. Cell Biol.*, 153:881–887, 2001.

[13] K. A. Beningo and Y.-L. Wang. Flexible substrata for the detection of cellular traction forces. *Trends Cell Biol.*, 12:79–84, 2002.

[14] M. Benoit, D. Gabriel, G. Gerisch, and H. E. Gaub. Discrete interactions in cell adhesion measured by single-molecule force spectroscopy. *Nat. Cell Biol.*, 2:313–317, 2000.

[15] K. Berndl, J. Käs, R. Lipowsky, E. Sackmann, and U. Seifert. Shape transformations of giant vesicles: extreme sensitivity to bilayer asymmetry. *Europhys. Lett.*, 13:659–664, 1990.

[16] A. Bershadsky, N. Q. Balaban, and B. Geiger. Adhesion-dependent cell mechanosensitivity. *Annu. Rev. Cell. Dev. Biol.*, 19:677–95, 2003.

[17] I. B. Bischofs, S. A. Safran, and U. S. Schwarz. Elastic interactions of active cells with soft materials. *Phys. Rev. E*, 69:021911, 2004.

[18] I. B. Bischofs and U. S. Schwarz. Cell organization in soft media due to active mechanosensing. *Proc. Natl. Acad. Sci. USA*, 100:9274–9279, 2003.

[19] A. Brock, E. Chang, C.-C. Ho, P. LeDuc, X. Jiang, G. W. Whitesides, and D. E. Ingber. Geometric determinants of directional cell motility revealed using microcontact printing. *Langmuir*, 19:1611–1617, 2003.

[20] R. Bruinsma. Physical aspects of adhesion of leukocytes. In T. Riste and D. Sherrington, editors, *Physics of biomaterials: fluctuations, self-assembly and evolution*, pages 61–101, Amsterdam, 1996. Kluwer.

[21] R. Bruinsma, A. Behrisch, and E. Sackmann. Adhesive switching of membranes: experiment and theory. *Phys. Rev. E*, 61:4253–4266, 2000.

[22] R. Bruinsma, M. Goulian, and P. Pincus. Self-assembly of membrane junctions. *Biophys. J.*, 67:746–750, 1994.

[23] K. Burton, J. H. Park, and D. L. Taylor. Keratocytes generate traction forces in two phases. *Mol. Biol. Cell*, 10:3745–3769, 1999.

[24] K. Burton and D. L. Taylor. Traction forces of cytokinesis measured with optically modified elastic substrata. *Nature*, 385:450–454, 1997.

[25] J. P. Butler, I. M. Tolic-Norrelykke, B. Fabry, and J. J. Fredberg. Traction fields, moments, and strain energy that cells exert on their surroundings. *Am. J. Physiol. Cell Physiol.*, 282:C595–C605, 2002.

[26] I. Cantat and C. Misbah. Lift force and dynamical unbinding of adhering vesicles under shear flow. *Phys. Rev. Lett.*, 83:880–883, 1999.

[27] K.-C. Chang and D. A. Hammer. The forward rate of binding of surface-tethered reactants: effect of relative motion between two surfaces. *Biophys. J.*, 76:1280–1292, 1999.

[28] K.-C. Chang, D. F. J. Tees, and D. A. Hammer. The state diagram for cell adhesion under flow: leukocyte rolling and firm adhesion. *Proc. Natl. Acad. Sci. USA*, 97:11262–11267, 2000.

[29] C. S. Chen, M. Mrksich, S. Huang, G. W. Whitesides, and D. E. Ingber. Geometric control of cell life and death. *Science*, 276:1425–1428, 1997.

[30] S. Chen and T. A. Springer. An automatic braking system that stabilizes leukocyte rolling by an increase in selectin bond number with shear. *J. Cell Biol.*, 144:185–200, 1999.

[31] S. Chen and T. A. Springer. Selectin receptor-ligand bonds: formation limited by shear rate and dissociation governed by the Bell model. *Proc. Natl. Acad. Sci. USA*, 98:950–955, 2001.

[32] W. Chen and S. J. Singer. Immunoelectron microscopic studies of the sites of cell-substratum and cell-cell contacts in cultured fibroblasts. *J. Cell Biol.*, 95:205–222, 1982.

[33] S. E. Chesla, P. Selvaraj, and C. Zhu. Measuring two-dimensional receptor-ligand binding kinetics by micropipette. *Biophys. J*, 75:1553–1572, 1998.

[34] M. E. Chicurel, C. S. Chen, and D. E. Ingber. Cellular control lies in the balance of forces. *Curr. Opin. Cell. Biol.*, 10:232–239, 1998.

[35] D. Choquet, D. F. Felsenfeld, and M. P. Sheetz. Extracellular matrix rigidity causes strengthening of integrin-cytoskeleton linkages. *Cell*, 88:39–48, 1997.

[36] E. Cukierman, R. Pankov, D.R. Stevens, and K.M. Yamada. Taking cell-matrix adhesions to the third dimension. *Science*, 294:1708–1712, 2002.

[37] A. Curtis and M. Riehle. Tissue engineering: the biophysical background. *Phys. Med. Biol.*, 46:R47–R65, 2001.

[38] P. C. Dartsch, H. Hämmerle, and E. Betz. Orientation of cultured arterial smooth muscle cells growing on cyclically stretched substrates. *Acta anat.*, 125:108–113, 1986.

[39] M. J. Davis and M. A. Hill. Signaling mechanisms underlying the vascular myogenic response. *Physiol. Rev.*, 79:387–423, 1999.

[40] M. Dembo, T. Oliver, A. Ishihara, and K. Jacobson. Imaging the traction stresses exerted by locomoting cells with the elastic substratum method. *Biophys. J.*, 70:2008–2022, 1996.

[41] M. Dembo, D. C. Torney, K. Saxman, and D. Hammer. The reaction-limited kinetics of membrane-to-surface adhesion and detachment. *Proc. R. Soc. Lond. B*, 234:55–83, 1988.

[42] M. Dembo and Y.-L. Wang. Stresses at the cell-to-substrate interface during locomotion of fibroblasts. *Biophys. J.*, 76:2307–2316, 1999.

[43] H. J. Donahue. Gap junctions and biophysical regulation of bone cell differentiation. *Bone*, 26:417–422, 2000.

[44] O. Dwir, A. Solomon, S. Mangan, G. S. Kansas, U. S. Schwarz, and R. Alon. Avidity enhancement of L-selectin bonds by flow: shear-promoted rotation of leukocytes turn labile bonds into functional tethers. *J. Cell Biol.*, 163:649–659, 2003.

[45] M. Eastwood, V. C. Mudera, D. A. McGrouther, and R. A. Brown. Effect of precise mechanical loading on fibroblast populated collagen lattices. *Cell Motil. Cytoskel.*, 40:13–21, 1998.

[46] A. Engler, L. Bacakova, C. Newman, A. Hategan, M. Griffin, and D. Discher. Substrate compliance versus ligand density in cell on gel response. *Biophys. J.*, 86:617–628, 2004.

[47] T. Erdmann and U. S. Schwarz. Adhesion clusters under shared linear loading: a stochastic analysis. *Europhys. Lett.*, 66:603–609, 2004.

[48] T. Erdmann and U. S. Schwarz. Stability of adhesion clusters under constant force. *Phys. Rev. Lett.*, 92:108102, 2004.

[49] E. Evans. Probing the relation between force, lifetime and chemistry in single molecular bonds. *Annu. Rev. Biophys. Biomol. Struct.*, 30:105–28, 2001.

[50] E. Evans, A. Leung, D. Hammer, and S. Simon. Chemically distinct transition states govern rapid dissociation of single L-selectin bonds under force. *Proc. Natl. Acad. Sci. USA*, 98:3784–3789, 2001.

[51] E. Evans and K. Ritchie. Dynamic strength of molecular adhesion bonds. *Biophys. J.*, 72:1541–1555, 1997.

[52] E. Evans and K. Ritchie. Strength of a weak bond connecting flexible polymer chains. *Biophys. J.*, 76:2439–2447, 1999.

[53] E. B. Finger, K. D. Puri, R. Alon, M. B. Lawrence, U. H. von Andrian, and T. A. Springer. Adhesion through L-selectin requires a threshold hydrodynamic shear. *Nature*, 379:266–269, 1996.

[54] E.-L. Florin, V. T. Moy, and H. E. Gaub. Adhesion forces between individual ligand-receptor pairs. *Science*, 264:415–417, 1994.

[55] J. Fritz, A. G. Katopodis, F. Kolbinger, and D. Anselmetti. Force-mediated kinetics of single P-selectin/ligand complexes observed by atomic force microscopy. *Proc. Nat. Acad. Sci. USA*, 95:12283–12288, 1998.

[56] C. G. Galbraith and M. Sheetz. Forces on adhesive contacts affect cell function. *Curr. Opin. Cell Biol.*, 10:566–571, 1998.

[57] M. Gao, D. Craig, O. Lequin, I. D. Campbell, V. Vogel, and K. Schulten. Structure and functional significance of mechanically unfolded fibronectin type III_1 intermediates. *Proc. Nat. Acad. Sci. USA*, 100:14784–14789, 2003.

[58] B. Geiger and A. Bershadsky. Assembly and mechanosensory function of focal contacts. *Curr. Opin. Cell Biol.*, 13:584–592, 2001.

[59] B. Geiger and A. Bershadsky. Exploring the neighborhood: adhesion-coupled cell mechanosensors. *Cell*, 110:139–142, 2002.

[60] B. Geiger, A. Bershadsky, R. Pankov, and K.M. Yamada. Transmembrane crosstalk between the extracellular matrix and the cytoskeleton. *Nat. Rev. Mol. Cell Biol.*, 2:793–805, 2001.

[61] D. T. Gillespie. Exact stochastic simulation of coupled chemical reactions. *J. Phys. Chem.*, 81:2340–2361, 1977.

[62] P. G. Gillespie and R. G. Walker. Molecular basis of mechanosensory transduction. *Nature*, 413:194–202, 2001.

[63] T. S. Girton, V. H. Barocas, and R. T. Tranquillo. Confined compression of a tissue-equivalent: collagen fibril and cell alignment in response to anisotropic strain. *J. Biomech. Eng.*, 124:568–575, 2002.

[64] N. S. Goel and N. Richter-Dyn. *Stochastic models in biology.* Academic Press, New York, 1974.

[65] A. J. Goldmann, R. G. Cox, and H. Brenner. Slow viscous motion of a sphere parallel to a plane wall - II couette flow. *Chem. Eng. Sci.*, 22:653–660, 1967.

[66] B. Goldstein and C. Wofsy. Why is it so hard to dissociate multivalent antigens from cell-surface antibodies ? *Immunology Today*, 17:77–80, 1996.

[67] A. W. Greenberg, D. K. Brunk, and D. A. Hammer. Cell-free rolling mediated by L-selectin and sialyl Lewis^x reveals the shear threshold effect. *Biophys. J.*, 79:2391–2402, 2000.

[68] F. Grinnell. Fibroblast-collagen-matrix contraction: growth-factor signalling and mechanical loading. *Trends in Cell Biol.*, 10:362–365, 2000.

[69] H. Grubmüller, B. Heymann, and P. Tavan. Ligand binding: molecular mechanics calculation of the streptavidin-biotin rupture force. *Science*, 271:997–999, 1996.

[70] J. Guck, R. Ananthakrishnan, H. Mahmood, T. J. Moon, C. C. Cunningham, and J. Käs. The optical stretcher: a novel laser tool to micromanipulate cells. *Biophys. J.*, 81:767–84, 2001.

[71] Z. Guttenberg, A. R. Bausch, B. Hu, R. Bruinsma, L. Moroder, and E. Sackmann. Measuring ligand-receptor unbinding forces with magnetic beads: Molecular leverage. *Langmuir*, 16:8984–8993, 2000.

[72] D. A. Hammer and S. M. Apte. Simulation of cell rolling and adhesion on surfaces in shear flow: general results and analysis of selectin-mediated neutrophil adhesion. *Biophys. J.*, 63:35–57, 1992.

[73] P. Hänggi, P. Talkner, and M. Borkovec. Reaction-rate theory: fifty years after Kramers. *Rev. Mod. Phys.*, 62:251–341, 1990.

[74] P. C. Hansen. *Rank-deficient and discrete ill-posed problems.* SIAM monographs on mathematical modeling and computation. SIAM, Philadelphia, PA, 1998.

[75] A. K. Harris, D. Stopak, and P. Wild. Fibroblast traction as a mechanism for collagen morphogenesis. *Nature*, 290:249–251, 1981.

[76] A. K. Harris, P. Wild, and D. Stopak. Silicone rubber substrata: a new wrinkle in the study of cell locomotion. *Science*, 208:177–179, 1980.

[77] W. S. Haston, J. M. Shields, and P. C. Wilkinson. The orientation of fibroblasts and neutrophils on elastic substrates. *Exp. Cell Res.*, 146:117–126, 1983.

[78] E. Helfer, S. Harlepp, L. Bourdieu, J. Robert, F. C. MacKintosh, and D. Chatenay. Microrheology of biopolymer-membrane complexes. *Phys. Rev. Lett.*, 85:457–60, 2000.

[79] B. Heymann and H. Grubmüller. Dynamic force spectroscopy of molecular adhesion bonds. *Phys. Rev. Lett.*, 84:6126–6129, 2000.

[80] R.-P. Hirsekorn and R. Siems. Long-range interaction of point defects with arbitrary dipole tensors. *Z. Phys. B - Cond. Mat.*, 40:311–319, 1981.

[81] J. Honerkamp. *Stochastische dynamische Systeme.* VCH, Weinheim, 1990.

[82] J. Honerkamp and J. Weese. Tikhonovs regularization method for ill-posed problems. *Continuum Mech. Thermodyn.*, 2:17–30, 1990.

[83] J. Howard. *Mechanics of motor proteins and the cytoskeleton.* Sinauer Associates, Sunderland, Massachusetts, 2001.

[84] S. Huang and D. E. Ingber. The structural and mechanical complexity of cell-growth control. *Nat. Cell Biol.*, 1:E131–E138, 1999.

[85] D. Humphrey, C. Duggan, D. Saha, D. Smith, and J. Käs. Active fluidization of polymer networks through molecular motors. *Nature*, 416:413–6, 2002.

[86] J. N. Israelachvili. *Intermolecular and surface forces.* Academic Press, London, 1992.

[87] B. Isralewitz, M. Gao, and K. Schulten. Steered molecular dynamics and mechanical functions of proteins. *Curr. Opin. Struct. Biol.*, 11:224–230, 2001.

[88] S. Izrailev, S. Stepaniants, M. Balsera, Y. Oono, and K. Schulten. Molecular dynamics study of unbinding of the avidin-biotin complex. *Biophys. J.*, 72:1568–1581, 1997.

[89] P. A. Janmey, T. Yeung, and L. A. Flanagan. Effect of substrate stiffness on cell morphology. *Abstracts ASME Summer Bioengineering Conference*, 50:709–710, 2001.

[90] K. L. Johnson. *Contact mechanics.* Cambridge University Press, Cambridge, 1985.

[91] F. Jülicher, A. Ajdari, and J. Prost. Modeling molecular motors. *Rev. Mod. Phys.*, 69:1269–1281, 1997.

[92] F. Jülicher and R. Lipowsky. Domain induced budding of vesicles. *Phys. Rev. Lett.*, 70:2964–2967, 1993.

[93] M. S. Z. Kellermayer, S. B. Smith, H. L. Granzier, and C. Bustamante. Folding-unfolding transitions in single titin molecules characterized with laser tweezers. *Science*, 276:1112–1116, 1997.

[94] I. Koltover, J. O. Rädler, and C. R. Safinya. Membrane mediated attraction and ordered aggregation of colloidal particles bound to giant phospholipid vesicles. *Phys. Rev. Lett.*, 82:1991–1994, 1999.

[95] H. A. Kramers. Brownian motion in a field of force and the diffusion model of chemical reactions. *Physica*, 7:284–304, 1940.

[96] A. Krammer, H. Lu, B. Isralewitz, K. Schulten, and V. Vogel. Forced unfolding of the fibronectin type iii module reveals a tensile molecular recognition switch. *Proc. Natl. Acad. Sci. USA*, 96:1351–1356, 1999.

[97] M. Kraus, W. Wintz, U. Seifert, and R. Lipowsky. Fluid vesicles in shear flow. *Phys. Rev. Lett.*, 77:3685–3688, 1996.

[98] S. C. Kuo, D. A. Hammer, and D. A. Lauffenburger. Simulation of detachment of specifically bound particles from surfaces by shear flow. *Biophys. J.*, 73:517–531, 1997.

[99] L. D. Landau and E. M. Lifshitz. *Theory of elasticity*, volume 7 of *Course of Theoretical Physics.* Pergamon Press, Oxford, 2nd edition, 1970.

[100] K. H. Lau and W. Kohn. Elastic interaction of two atoms adsorbed on a solid surface. *Surf. Sci.*, 65:607–618, 1977.

[101] D. A. Lauffenburger and J. J. Linderman. *Receptors: models for binding, trafficking, and signalling.* Oxford University Press, Oxford, 1993.

[102] D. Leckband and J. Israelachvili. Intermolecular forces in biology. *Quart. Rev. Biophys.*, 34:105–267, 2001.

[103] J. Lee, M. Leonard, T. Oliver, A. Ishihara, and K. Jacobson. Traction forces generated by locomoting keratocytes. *J. Cell Biol.*, 127:1957–1964, 1994.

[104] D. Lehnert, B. Wehrle-Haller, C. David, U. Weiland, C. Ballestrem, B. A. Imhof, and M. Bastmeyer. Cell behaviour on micropatterned substrata: limits of extracellular matrix geometry for spreading and adhesion. *J. Cell Sci.*, 117:41–52, 2003.

[105] P. Lenz, J.-F. Joanny, F. Jülicher, and J. Prost. Membranes with rotating motors. *Phys. Rev. Lett.*, 91:108104, 2003.

[106] F. Li, S. D. Redick, H. P. Erickson, and V. T. Moy. Force measurements of the $\alpha_5\beta_1$ integrin-fibronectin interaction. *Biophys. J.*, 84:1252–1262, 2003.

[107] H. W. G. Lim, M. Wortis, and R. Mukhopadhyay. Stomatocyte-discocyte-echinocyte sequence of the human red blood cell: evidence for the bilayer-couple hypothesis from membrane mechanics. *Proc. Natl. Acad. Sci. USA*, 99:16766–9, 2002.

[108] L. Limozin and E. Sackmann. Polymorphism of cross-linked actin networks in giant vesicles. *Phys. Rev. Lett.*, 89:168103, 2002.

[109] R. Lipowsky. The conformation of membranes. *Nature*, 349:475–481, 1991.

[110] R. Lipowsky. Budding of membranes induced by intramembrane domains. *J. Phys. II France*, 2:1825–1840, 1992.

[111] R. Lipowsky. Adhesion of membranes via anchored stickers. *Phys. Rev. Lett.*, 77:1652–1655, 1996.

[112] R. Lipowsky. Molecular motors and stochastic models. In J. A. Freund and T. Pschel, editors, *Stochastic Processes in Physics, Chemistry, and*

Biology, volume 557 of *Lecture Notes in Physics*, pages 21–31. Springer, Berlin, 2000.

[113] R. Lipowsky. Biomimetic materials and transport systems. In *European White Book on Fundamental Research in Materials Science*, pages 78–82. Max-Planck-Institut für Metallforschung, 2001.

[114] R. Lipowsky and H. G. Döbereiner. Vesicles in contact with nanoparticles and colloids. *Europhys. Lett.*, 43:219–225, 1998.

[115] R. Lipowsky and E. Sackmann. *Structure and dynamics of membranes*, volume 1A and 1B of *Handbook of biological physics*. Elsevier, Amsterdam, 1995.

[116] C.-M. Lo, H.-B. Wang, M. Dembo, and Y.-L. Wang. Cell movement is guided by the rigidity of the substrate. *Biophys. J.*, 79:144–152, 2000.

[117] B. Lorz, R. Simson, J. Nardi, and E. Sackmann. Weakly adhering vesicles in shear flow: tanktreading and anomalous lift force. *Europhys. Lett.*, 51:468–474, 2000.

[118] A. E. H. Love. *A treatise on the mathematical theory of elasticity*. Dover Publications, New York, 1944.

[119] H. Lu, B. Isralewitz, A. Krammer, V. Vogel, and K. Schulten. Unfolding of titin immunoglobulin domains by steered molecular dynamics simulation. *Biophys. J.*, 75:662–671, 1998.

[120] J. T. H. Mandeville, M. A. Lawson, and F. R. Maxfield. Dynamic imaging of neutrophil migration in three dimensions: mechanical interactions between cells and matrix. *J. Leukoc. Biol.*, 61:188–200, 1997.

[121] B. T. Marshall, M. Long, J. W. Piper, T. Yago, R. P. McEver, and C. Zhu. Direct observation of catch bonds involving cell-adhesion molecules. *Nature*, 423:190–193, 2003.

[122] D. A. McQuarrie. Kinetics of small systems I. *J. Chem. Phys.*, 38:433–436, 1963.

[123] R. Menes and S. A. Safran. Nonlinear response of membranes to pinning sites. *Phys. Rev. E*, 56:1891–1899, 1997.

[124] R. Merkel, P. Nassoy, A. Leung, K. Ritchie, and E. Evans. Energy landscapes of receptor-ligand bonds explored with dynamic force spectroscopy. *Nature*, 397:50–53, 1999.

[125] L. Miao, U. Seifert, M. Wortis, and H. G. Döbereiner. Budding transitions of fluid-bilayer vesicles: the effect of area difference elasticity. *Phys. Rev. E.*, 49:5389–5407, 1994.

[126] R. D. Mindlin. Force at a point in the interior of a semi-infinite solid. *Physics*, 7:195–202, 1936.

[127] A. G. Moon and R. T. Tranquillo. Fibroblast-populated collagen microsphere assay of cell traction force: part 1, continuum model. *AIChE J.*, 39:163–177, 1993.

[128] S. Munevar, Y.-L. Wang, and M. Dembo. Regulation of mechanical interactions between fibroblasts and the substratum by stretch-activated Ca^{2+} entry. *J. Cell Sci.*, 117:85–92, 2004.

[129] A. Offenhäusser and W. Knoll. Cell-transistor hybrid systems and their potential applications. *Trends Biotechnol.*, 19:62–66, 2001.

[130] T. Oliver, M. Dembo, and K. Jacobson. Separation of propulsive and adhesive traction stresses in locomoting keratocytes. *J. Cell Biol.*, 145:589–604, 1999.

[131] C. E. Orsello, D. A. Lauffenburger, and D. A. Hammer. Molecular properties in cell adhesion: a physical and engineering perspective. *Trends Biotech.*, 19:310–316, 2001.

[132] G. F. Oster, J. D. Murray, and A. K. Harris. Mechanical aspects of mesenchymal morphogenesis. *J. Embryol. Exp. Morph.*, 78:83–125, 1983.

[133] S. Park, F. Khalili-Araghi, E. Tajkhorshid, and K. Schulten. Free energy calculation from steered molecular dynamics simulations using Jarzynski's equality. *J. Chem. Phys.*, 119:3559–3566, 2003.

[134] K. K. Parker, A. L. Brock, C. Brangwynne, R. J. Mannix, N. Wang, E. Ostuni, N. A. Geisse, J. C. Adams, G. W. Whitesides, and D. E. Ingber. Directional control of lamellipodia extension by constraining

cell shape and orienting cell tractional forces. *FASEB J.*, 16:1195–1204, 2002.

[135] R. J. Pelham and Y.-L. Wang. Cell locomotion and focal adhesions are regulated by substrate flexibility. *Proc. Natl. Acad. Sci. USA*, 94:13661–13665, 1997.

[136] N. Phan-Thien. On the image system for the Kelvin-state. *J. Elast.*, 13:231–235, 1983.

[137] A. Pierres, D. Touchard, A.-M. Benoliel, and P. Bongrand. Dissecting streptavidin-biotin interaction with the laminar flow chamber. *Biophys. J.*, 82:3214–3223, 2002.

[138] K. Prechtel, A. R. Bausch, V. Marchi-Artzner, M. Kantlehner, H. Kessler, and R. Merkel. Dynamic force spectroscopy to probe adhesion strength of living cells. *Phys. Rev. Lett.*, 89:028101, 2002.

[139] W. H. Press, S. A. Teukolsky, W. T. Vetterling, and B. P. Flannery. *Numerical recipes in FORTRAN. The art of scientific computing.* Cambridge University Press, Cambridge, 2nd ed. edition, 1992.

[140] M. Radmacher, M. Fritz, C. M. Kacher, J. P. Cleveland, and P. K. Hansma. Measuring the viscoelastic properties of human platelets with the Atomic Force Microscope. *Biophys. J.*, 70:556–567, 1996.

[141] S. Ramaswamy, J. Toner, and J. Prost. Nonequilibrium fluctuations, traveling waves, and instabilities in active membranes. *Phys. Rev. Lett.*, 84:3494–3497, 2000.

[142] X. D. Ren, W. B. Kiosses, and M. A. Schwartz. Regulation of the small grp-binding protein rho by cell adhesion and the cytoskeleton. *EMBO J.*, 18:578–585, 1999.

[143] M. Rief, M. Gautel, F. Oesterhelt, J. M. Fernandez, and H. E. Gaub. Reversible unfolding of individual titin immunoglobulin domains by AFM. *Science*, 276:1109–1112, 1997.

[144] D. Riveline, E. Zamir, N. Q. Balaban, U. S. Schwarz, B. Geiger, Z. Kam, and A. D. Bershadsky. Focal contact as a mechanosensor:

externally applied local mechanical force induces growth of focal contacts by a mDia1-dependent and ROCK-independent mechanism. *J. Cell Biol.*, 153:1175–1185, 2001.

[145] H. Rossiter, R. Alon, and T. S. Kupper. Selectins, T-cell rolling and inflammation. *Molec. Med. Today*, 3:214–222, 1997.

[146] P. Roy, Z. Rajfur, P. Pomorski, and K. Jacobson. Microscope-based techniques to study cell adhesion and migration. *Nat. Cell Biol.*, 4:E91–E96, 2002.

[147] S. A. Safran and D. R. Hamann. Long-range elastic interactions and staging in graphite intercalation compounds. *Phys. Rev. Lett.*, 42:1410–1413, 1979.

[148] Y. Sawada and M. P. Sheetz. Force transduction by Triton cytoskeletons. *J. Cell Biol.*, 156:609–615, 2002.

[149] U. S. Schwarz and R. Alon. L-selectin mediated leukocyte tethering in shear flow is controled by multiple contacts and cytoskeletal anchorage facilitating fast rebinding events. *Proc. Natl. Acad. Sci. USA*, 101:6940–6945, 2004.

[150] U. S. Schwarz, N. Q. Balaban, D. Riveline, L. Addadi, A. Bershadsky, S. A. Safran, and B. Geiger. Measurement of cellular forces at focal adhesions using elastic micro-patterned substrates. *Mat. Sci. Eng. C*, 23:387–394, 2003.

[151] U. S. Schwarz, N. Q. Balaban, D. Riveline, A. Bershadsky, B. Geiger, and S. A. Safran. Calculation of forces at focal adhesions from elastic substrate data: the effect of localized force and the need for regularization. *Biophys. J.*, 83:1380–1394, 2002.

[152] U. S. Schwarz, S. Komura, and S. A. Safran. Deformation and tribology of multi-walled hollow nanoparticles. *Europhys. Lett.*, 50:762–768, 2000.

[153] U. S. Schwarz and S. A. Safran. Elastic interactions of cells. *Phys. Rev. Lett.*, 88:048102, 2002.

[154] U. Seifert. Configurations of fluid membranes and vesicles. *Adv. Phys.*, 46:13–137, 1997.

[155] U. Seifert. Hydrodynamic lift on bound vesicles. *Phys. Rev. Lett.*, 83:876–879, 1999.

[156] U. Seifert. Rupture of multiple parallel molecular bonds under dynamic loading. *Phys. Rev. Lett.*, 84:2750–2753, 2000.

[157] U. Seifert. Dynamic strength of adhesion molecules: role of rebinding and self-consistent rates. *Europhys. Lett.*, 58:792–798, 2002.

[158] U. Seifert and R. Lipowsky. Adhesion of vesicles. *Phys. Rev. A*, 42:4768–4771, 1990.

[159] A. Shaub. Unravelling the extracellular matrix. *Nat. Cell. Biol.*, 1:E173–E175, 1999.

[160] J. Shillcock and U. Seifert. Escape from a metastable well under a time-ramped force. *Phys. Rev. E*, 57:7301–7304, 1998.

[161] R. Siems. Mechanical interactions of point defects. *Phys. Stat. Sol.*, 30:645–658, 1968.

[162] R. A. Simha and S. Ramaswamy. Hydrodynamic fluctuations and instabilities in ordered suspensions of self-propelled particles. *Phys. Rev. Lett.*, 89:058101, 2002.

[163] D. A. Simson, M. Strigl, M. Hohenadl, and R. Merkel. Statistical breakage of single protein A-IgG bonds reveals crossover from spontaneous to force-induced bond dissociation. *Phys. Rev. Lett.*, 83:652–655, 1999.

[164] R. Singhvi, A. Kumar, G. P. Lopez, G. N. Stephanopoulos, D. I. Wang, G. M. Whitesides, and D. E. Ingber. Engineering cell shape and function. *Science*, 264:696–8, 1994.

[165] J. V. Small, B. Geiger, I. Kaverina, and A. Bershadsky. How do microtubules guide migrating cells ? *Nat. Rev. Mol. Cell Biol.*, 3:957–964, 2002.

[166] A.-S. Smith, E. Sackmann, and U. Seifert. Effects of a pulling force on the shape of a bound vesicle. *Europhys. Lett.*, 64:281–287, 2003.

[167] S. Sukumaran and U. Seifert. Influence of shear flow on vesicles near a wall: a numerical study. *Phys. Rev. E*, 6401:1916, 2001.

[168] K. Takakuda and H. Miyairi. Tensile behaviour of fibroblasts cultured in collagen gel. *Biomaterials*, 17:1393–1397, 1996.

[169] J. L. Tan, J. Tien, D. M. Pirone, D. S. Gray, K. Bhadriraju, and C. S. Chen. Cells lying on a bed of microneedles: An approach to isolate mechanical force. *Proc. Natl. Acad. Sci. USA*, 100:1484–1489, 2003.

[170] D. F. J. Tees, J. T. Woodward, and D. A. Hammer. Reliability theory for receptor-ligand bond dissociation. *J. Chem. Phys.*, 114:7483–7496, 2001.

[171] T. Tlusty and S. A. Safran. Defect-induced phase separation in dipolar fluids. *Science*, 290:1328–1331, 2000.

[172] N. G. van Kampen. *Stochastic processes in physics and chemistry.* Elsevier, Amsterdam, 1992.

[173] H. Wagner and H. Horner. Elastic interaction and the phase transition in coherent metal-hydrogen systems. *Adv. Phys.*, 23:587, 1974.

[174] L. J. Walpole. An elastic singularity in joined half-spaces. *Int. J. Engng. Sci.*, 34:629–638, 1996.

[175] N. Wang, J. P. Butler, and D. E. Ingber. Mechanotransduction across the cell surface and through the cytoskeleton. *Science*, 260:1124–1127, 1993.

[176] N. Wang, E. Ostuni, G. W. Whitesides, and D. E. Ingber. Micropatterning tractional forces in living cells. *Cell Motil. Cytoskeleton*, 52:97–106, 2002.

[177] T. R. Weikl, R. R. Netz, and R. Lipowsky. Unbinding transitions and phase separation of multicomponent membranes. *Phys. Rev. E*, 62:R45–R48, 2000.

[178] H. R. Wirtz and L. G. Dobbs. The effects of mechanical forces on lung functions. *Resp. Physiol.*, 119:1–17, 2000.

[179] J. Y. Wong, A. Velasco, P. Rajagopalan, and Q. Pham. Directed movement of vascular smooth muscle cells on gradient-compliant hydrogels. *Langmuir*, 19:1908–1913, 2003.

[180] E. Zamir, B.-Z. Katz, S. Aota, K. M. Yamada, B. Geiger, and Z. Kam. Molecular diversity of cell-matrix adhesions. *J. Cell Sci.*, 112:1655–1669, 1999.

[181] E. Zamir, M. Katz, Y. Posen, N. Erez, K. M. Yamada, B. Z. Katz BZ, S. Lin, D. C. Lin, A. Bershadsky, Z. Kam, and B. Geiger. Dynamics and segregation of cell-matrix adhesions in cultured fibroblasts. *Nat. Cell Biol.*, 2:191–196, 2000.

[182] C. Zhu, M. Long, S. E. Chesla, and P. Bongrand. Measuring receptor/ligand interaction at the single-bond level: experimental and interpretative issues. *Ann. Biomed. Eng.*, 30:305–314, 2002.

Acknowledgements

Foremost I want to thank the academic teachers who guided my way into science. This includes Herbert Wagner, Gerhard Gompper, Reinhard Lipowsky, Udo Seifert and Sam Safran, who introduced me to soft matter and biological physics, and who provided continuous intellectual stimulation both through numerous discussions and their own work. I am especially indebted to Reinhard Lipowsky, who gave me the chance to become group leader in the theory department of the Max Planck Institute of Colloids and Interface at Golm. Without his continuous support, this work would not have been possible. I owe a debt of gratitude also to Erich Sackmann, Benjamin Geiger and Ronen Alon, for explaining to me the experimental challenges in the physics of cells.

I would like to thank Ilka Bischofs, Thorsten Erdmann and Christian Korn for the decision to start their PhD-work with me at the Max Planck Institute, for numerous discussions and for enjoyable collaboration. I also want to thank my other collaborators during recent years, including Nathalie Balaban, Daniel Riveline, Alexander Bershadsky, Lia Addadi, Benjamin Geiger, Oren Dwir and Ronen Alon. Furthermore I benefited from numerous discussions with colleagues, including Martin Bastmeyer, Adam Curtis, Dennis Discher, Hans-Günther Döbereiner, Evan Evans, Peter Fratzl, Dieter Fürst, Paul Janmey, Josef Käs, Jan Kierfeld, Stefan Klumpp, Tom Lubensky, Rudolf Merkel, Andreas Offenhäuser, Mathis Riehle, Mike Sheetz, Joachim Spatz, and Tsvi Tlustly.

Last but not least I want to thank the German Science Foundation for support through the Emmy Noether Program and Stefanie Geldbach and my parents for the fact that they always accepted my passion for science.

Publications used in this work

Elastic substrates

- N. Q. Balaban, U. S. Schwarz, D. Riveline, P. Goichberg, G. Tzur, I. Sabanay, D. Mahalu, S. Safran, A. Bershadsky, L. Addadi, and B. Geiger, Force and focal adhesion assembly: a close relationship studied using elastic micro-patterned substrates, *Nat. Cell Biol.* **3**: 466–472, 2001.
- U. S. Schwarz, N. Q. Balaban, D. Riveline, A. Bershadsky, B. Geiger, and S. A. Safran, Calculation of forces at focal adhesions from elastic substrate data: the effect of localized force and the need for regularization, *Biophys. J.* **83**: 1380–1394, 2002.
- U. S. Schwarz, N. Q. Balaban, D. Riveline, L. Addadi, A. Bershadsky, S. A. Safran, and B. Geiger, Measurement of cellular forces at focal adhesions using elastic micro-patterned substrates, *Mat. Sci. Eng. C* **23**: 387–394, 2003.

Bond dynamics

- T. Erdmann and U. S. Schwarz, Stability of adhesion clusters under constant force, *Phys. Rev. Lett.* **92**: 108102, 2004.
- T. Erdmann and U. S. Schwarz, Adhesion clusters under shared linear loading: a stochastic analysis, *Europhys. Lett.* **66**: 603–609, 2004.
- U. S. Schwarz and R. Alon, L-selectin mediated leukocyte tethering in shear flow is controled by multiple contacts and cytoskeletal anchorage facilitating fast rebinding events, *Proc. Natl. Acad. Sci. USA* **101**: 6940–6945, 2004.

Elastic interactions

- U. S. Schwarz and S. A. Safran, Elastic interactions of cells, *Phys. Rev. Lett.* **88**: 048102, 2002.

- I. B. Bischofs and U. S. Schwarz, Cell organization in soft media due to active mechanosensing, *Proc. Natl. Acad. Sci. USA* **100**: 9274–9279, 2003.

- I. B. Bischofs, S. A. Safran, and U. S. Schwarz, Elastic interactions of active cells with soft materials, *Phys. Rev. E* **69**: 021911, 2004.